Università degli Studi di Roma Tre

SCUOLA DOTTORALE IN MATEMATICA E FISICA
Corso di Dottorato di Ricerca in Fisica (XXVII Ciclo)

Tesi di Dottorato di Ricerca

A preparatory study for the extraction of the transverse spin degrees of freedom of the neutron in high intensity frontier experiments

Candidato:
Alessio Del Dotto

Coordinatore:
Prof. Roberto Raimondi

Tutor:
Dr. Mauro Iodice
Prof. Giovanni Salmè

Anno Accademico 2014

Abstract

This thesis is part of the preparatory study related to the extraction of the neutron partonic spin structure in the future high intensity polarized semi-inclusive deep inelastic scattering experiments, that will run at Thomas Jefferson National Accelerator Facility (Virginia/USA). The first part concern with a deeper phenomenological understanding of the ^{3}He polarized target, which is used as an effective neutron target. A distorted spin-dependent Spectral Function has been calculated in an extended eikonal approximation and a fully Poincaré covariant framework for the relativistic description of the ^{3}He has been developed. In the second part of this thesis the issue of particles track filtering and fitting in high intensity scenario has been addressed. Tracks fitting algorithm based on Kalman filter has been developed and adapted to the conditions of the planned high luminosity experiments. Tests of the algorithm has been performed in rather realistic experimental conditions.

Contents

Chapter 1

Introduction

Since the beginning of the twentieth century, scattering experiments have been of great importance in clarifying properties and inner structure of the atomic nucleus. Clearly, the first milestone in the long path towards the detailed understanding of the nuclear and subnuclear world was the discovery of the atomic nucleus itself, achieved in 1911 by Rutherford, Geiger and Marsden through the scattering of α particles off a gold foil [1]. The technological improvements of the particles accelerators, in particular the increasing of the momentum of projectiles and therefore the spatial resolution power, have definitely given a central role to scattering experiments in the quest of knowledge on the subatomic matter.
In order to explain the quantum numbers and the decay modes of an incredible number of baryons and mesons, discovered in '50s and '60s using multi-GeV proton accelerators, in 1964, Gell-Mann and Zweig [2, 3], inferred the existence of spin-half constituent particles, called *quarks*, as building blocks to explain the non elementary nature of hadron. By the end of the '60s, the first inclusive Deep Inelastic Scattering (DIS) experiments were performed at SLAC [4], with an electron beam, and they confirmed the composite nature of the proton and the neutron, showing that the structure functions become substantially independent of the squared momentum transfer Q^2, when it grows but the ratio $Q^2/2M_N\nu$ remains constant (ν is the energy transfer). This so-called scaling behavior was interpreted by Bjorken and Feynman [5, 6, 7] as the evidence of the existence inside the nucleon of point-like particles, the charged partons. Then, as shown by the properties of the cross sections, the partons were identified with spin-half particles, having fractional electric charges and with new degrees of freedom, called flavour, (already predicted by Gell-Mann and Zweig).
According to the Quark Parton Model the proton is made of a pair of quarks of flavor *up* and charge $\frac{2}{3}e$ and a quark of flavor *down* and charge $-\frac{1}{3}e$, each of them carrying approximately one third of the proton mass (in a naive constituent quarks picture). Moreover, in a naive picture, in a proton with the spin in a certain direction, two quarks have the spin in the same direction and the third one must be antialigned (with this spin picture, the magnetic moment is pretty well reproduced). This spin picture would be useful in what follows.
Actually, an extension of the quark model was necessary when, in '70s, new experimental results showed that quarks provide roughly half of the nucleon momentum. Then, the existence of electrically neutral partons, called *gluons*, was postulated. Within the framework of rising *Quantum*

Chromodynamics (QCD), the standard field theory of strong interactions, gluons were interpreted as gauge bosons exchanged by quarks providing their binding force. It dates back to 1979 the experimental proof of the gluon existence, by the observation of three-jet events at the PETRA collider at DESY [8], in Hamburg.
The QCD vacuum, unlike in the QED case where vacuum polarization screens charges as their separation increases, provides an anti-screening that makes increasing the strong coupling constant α_s at large distance scales, corresponding to small momentum transfer.
The DIS experiments, performed at SLAC and more recently at DESY [9, 10], allowed the extraction of the now rather well known unpolarized parton distribution functions (DF, also known as PDF), that is the probability density for finding a charged parton with given flavor, with a certain fraction of the nucleon longitudinal momentum (along the direction of the exchanged boson in hard scattering experiment). Moreover, these experimental results confirm the *scale invariance* of the unpolarized DFs, namely they become Q^2-independent if the momentum transfer is large. In reality, some small deviations have been found. Scale invariance is broken by quantum corrections: even starting with vanishing quark masses the procedure of quantization and renormalization of the theory necessarily introduces a scale of mass Λ_{QCD} and scaling violations are logarithmic corrections computable in QCD.

1.1 The spin of the nucleon

The compound nature of the nucleon suggests to address another fundamental issue: the description of the nucleon spin in terms of the dynamics of its constituents. This kind of knowledge can be gained through the extraction of the polarized DF. In particular the scattering of a polarized beam off a polarized target is one of the experimental way to access the polarized DF. However, the difficulty to produce high energy polarized beams and, in particular, polarized nuclear targets has made this type of experiments not feasible for a long time.
The first measurement of polarized electron-proton scattering was performed in 1976 at SLAC by the E80 and E130 collaborations [11, 12]. The results were affected by sizable experimental uncertainties, but they were considered in agreement with the theoretical predictions of Ellis-Jaffe sum rules [13], based on the assumption that the most part of the nucleon angular momentum was carried by the *up*, *down* and *sea* quarks, only. In '80s at CERN, the EMC collaboration [14] performed a much more accurate measurement. The result turned out to be in disagreement with the theoretical predictions. The EMC results pointed to a "spin crisis", namely a nucleon spin third component only partially ascribed to the quark spin. This was felt in contrast with the very nice description of the nucleon magnetic moments achieved in terms of constituent quark spins. Then, it was the SMC experiment that, for the first time, could discriminate the valence quark contribution from the sea contributions to the nucleon spin [17]. This was possible thanks to Semi-Inclusive lepton-nucleon Deep Inelastic Scattering (SIDIS) measurements, where not only the final lepton was detected, but also one hadron produced in the nucleon fragmentation process.
The value of the quark spin contribution to the Ellis-Jaffe sum rules is obtained from polarized deep inelastic scattering by which the first moment of the g_1 structure function is extracted. The

Table 1.1: High energy spin experiments: the kinematic ranges in x and Q^2 correspond to the average kinematic values of the highest statistics measurement of each experiment, which is typically the inclusive spin asymmetry; x denotes the Bjorken variable x_B, unless specified. (After Ref. [15])

Experiment	Year	Beam	Target	Energy (GeV)	Q^2 (GeV^2)	x
Completed experiments						
SLAC – E80, E130	1976–1983	e^-	H-butanol	$\lesssim$23	1–10	0.1–0.6
SLAC – E142/3	1992–1993	e^-	NH_3, ND_3	$\lesssim$ 30	1–10	0.03–0.8
SLAC – E154/5	1995–1999	e^-	NH_3, ^{6}LiD, ^{3}He	$\lesssim$ 50	1–35	0.01–0.8
CERN – EMC	1985	μ^+	NH_3	100, 190	1–30	0.01–0.5
CERN – SMC	1992–1996	μ^+	H/D-butanol, NH_3	100, 190	1–60	0.004–0.5
FNAL E581/E704	1988–1997	p	p	200	~ 1	$0.1 < x_F < 0.8$
Analyzing and/or Running						
DESY – HERMES	1995–2007	e^+, e^-	H, D, ^{3}He	$\sim$ 30	1–15	0.02–0.7
CERN – COMPASS	2002–2012	μ^+	NH_3, ^{6}LiD	160, 200	1–70	0.003–0.6
JLab6 – Hall A	1999–2012	e^-	^{3}He	$\lesssim$ 6	1–2.5	0.1–0.6
JLab6 – Hall B	1999–2012	e^-	NH_3, ND_3	$\lesssim$ 6	1.-5	0.05–0.6
RHIC – BRAHMS	2002–2006	p	p (beam)	2× (31–100)	$\sim$ 1–6	$-0.6 < x_F < 0.6$
RHIC – PHENIX, STAR	2002+	p	p (beam)	2× (31–250)	$\sim$ 1–400	$\sim$ 0.02–0.4
Approved future experiments (in preparation)						
CERN – COMPASS–II	2014+	μ^+, μ^-	unpolarized H_2	160	$\sim$ 1–15	$\sim$ 0.005–0.2
		π^-	NH_3	190		$-0.2 < x_F < 0.8$
JLab12 – HallA/B/C	2014+	e^-	HD, NH_3, ND_3, ^{3}He	$\lesssim$12	$\sim$ 1–10	$\sim$ 0.05–0.8

experimental results showed that the quark contribution was about 25% (see [15] for a recent review). Therefore, in order to fulfill the sum rule one has to add all the possible contributions to the nucleon's spin: i) the gluon spin ΔG and ii) the orbital angular momenta of quarks, L_z^q, and gluons L_z^G.
In conclusion, one has

$$s_z^N = \frac{1}{2} = \frac{1}{2}\Delta\Sigma + \Delta G + L_z^q + L_z^G \tag{1.1}$$

where

$$\Delta\Sigma = (\Delta u + \Delta d + \Delta q_s) \tag{1.2}$$

Experiments that probed the nucleon spin structure and the main future planned experiments are summarized in Tab. 1.1. Recently, accurate measurements,with polarized targets and beam, by HERMES and COMPASS [18] collaborations have shown that the $\Delta\Sigma$ contribution is of the order of 30%. The experimental values of each contributions to $\Delta\Sigma$ (cf Eq. (2.58) are summarized in Tab. 1.2

The same collaborations measured also the ΔG term [18], that seems to be compatible with a vanishing value, within the still large experimental uncertainties. In Tab. 1.3 polarized gluon measurements from deep inelastic experiments are summarized. However, the chance to measure ΔG component in the proton has been one of the main drive at RICH, with the PHENIX and STAR detectors, using polarized proton - proton collision. Results from PHENIX, STAR and global fits to polarized world data from DIS, semi-inclusive DIS, and proton-proton collisions by de Florian-Sassot-Stratmann-Vogelsang (DSSV) provided the first evidence of a nonzero gluon polarization

Table 1.2: First moments for valence quark and light-sea polarization from SMC, HERMES, and COMPASS. For each experiment the integrated sea is evaluated from data up to $x = 0.3$ and, for SMC, assuming an isospin symmetric polarized sea. (After Ref. [15])

Experiment	x-range	Q^2 (GeV^2)	Δu_v	Δd_v	$\Delta \bar{u}$	$\Delta \bar{d}$	$\Delta\Sigma$
SMC	0.003–0.7	10	$0.73 \pm 0.10 \pm 0.07$	$-0.47 \pm 0.14 \pm 0.08$	$0.01 \pm 0.04 \pm 0.03$	$0.01 \pm 0.04 \pm 0.03$	$0.28 \pm 0.18 \pm 0.11$
HERMES	0.023–0.6	2.5	$0.60 \pm 0.07 \pm 0.04$	$-0.17 \pm 0.07 \pm 0.05$	$0.00 \pm 0.04 \pm 0.02$	$-0.05 \pm 0.03 \pm 0.01$	$0.38 \pm 0.11 \pm 0.07$
COMPASS	0.006–0.7	10	$0.67 \pm 0.03 \pm 0.03$	$-0.28 \pm 0.06 \pm 0.03$	$0.02 \pm 0.02 \pm 0.01$	$-0.05 \pm 0.03 \pm 0.02$	$0.36 \pm 0.08 \pm 0.05$

in the proton [16].
The last two terms of proton spin sum rule can be basically related to observables measured in semi-inclusive deep inelastic scattering (SIDIS) and Deeply Virtual Compton Scattering (see [15]), some results have been obtained with different targets and will be summarized at the end of the next Chapter. The main goal of the future experiments is the precision measurements of the last two terms in Eq. (1.1), and in particular, in the near future, it will be possible to measure the L_z^q term, for both proton and neutron. It is important to emphasize that precise measures on neutron are crucial in order to achieve a flavor decomposition of the terms contributing to the spin sum rules; this can be done trough semi-inclusive deep inelastic experiments which permit to gain informations on the so called transverse momentum dependent parton distributions of the neutron (see Chapter 2).
This is the physical motivation of the present thesis, that focuses on the SIDIS processes, where a polarized electron beam is scattered by a polarized ^{3}He target, with the aim of extracting the relevant information on the neutron, so that the flavor decomposition of the orbital contribution could be completed (even if in a model dependent manner). In particular, the work has been conducted in two parallel but complementary activities: i) the first deal with the evaluation of the systematic effects that the actual knowledge of the ^{3}He physical system induces on the relevant quantities one aim to extract from the experiments in order to know the inner quark dynamics of the neutron, which is extremely important in the context of a high luminosity experiment; ii) the second is related again to the extremely high luminosity (order 10^{39} cm^{-2}s^{-1}) that will be achieved in such a SIDIS experiments, indeed this means a really high statistical precision, and therefore the development of dedicated tracks filtering and fitting algorithms has been carried out in order to fully exploit the luminosity at disposal.

1.2 The parton distribution functions

The quark spin distribution, inside the nucleon, is described through several DFs [23], which in general depend on the 3-momentum of the parton. Averaging over the quark transverse momentum p_T in leading order (twist-two) approximation (see Chapter 2 for details), only three parton DFs are needed for a complete description of the nucleon spin structure. It should be pointed out that, after averaging on p_T, the DFs depend upon only the variable $x_B = Q^2/2M\nu$, the celebrated Bjorken variable.
Two of them, the momentum (or spin-independent) DF, $q(x)$, and the helicity DF, $\Delta q(x)$, are

Table 1.3: Polarized gluon measurements from deep inelastic experiments (After Ref.[15]). $\langle \mu^2 \rangle$ is the scale at which measurements are performed.

Experiment	process	$\langle x_g \rangle$	$\langle \mu^2 \rangle$ (GeV^2)	$\Delta G/G$
HERMES	hadron pairs	0.17	~ 2	$0.41 \pm 0.18 \pm 0.03$
HERMES	inclusive hadrons	0.22	1.35	$0.049 \pm 0.034 \pm 0.010^{+0.125}_{-0.099}$
SMC	hadron pairs	0.07		$-0.20 \pm 0.28 \pm 0.10$
COMPASS	hadron pairs, $Q^2 < 1$	0.085	3	$0.016 \pm 0.058 \pm 0.054$
COMPASS	hadron pairs, $Q^2 > 1$	0.09	3	$0.125 \pm 0.060 \pm 0.063$
COMPASS	open charm (LO)	0.11	13	$-0.06 \pm 0.21 \pm 0.08$
COMPASS	open charm (NLO)	0.20	13	$-0.13 \pm 0.15 \pm 0.15$

very well known and measured in a large number of experiments. The first DF is the probability density to find a quark inside the nucleon, carrying a fraction x of the nucleon momentum; the second one, if considered in the helicity basis, is the difference between the distribution probability to find a quark with helicity aligned and antialigned to the nucleon longitudinal polarization. The third DF, the transversity distribution $\delta q(x)$, have a correct probabilistic definition in a basis of transverse spin eigenstates and, in this basis, is the difference of the probability density to find, in a transversely polarized nucleon, a quark with its spin aligned and anti-aligned with respect to the transverse spin of the nucleon.
In a non relativistic framework, the transvesity distribution function is equal to the helicity one, i.e. $\delta q(x) \sim \Delta q(x)$. But, if one takes into account relativistic effects, it is expected to be different. Due to its *chiral-odd* nature, the transversity DF must be measured in an experimental process where another chiral-odd quantity is involved (recall that QCD at large extent is chirally invariant). This is the case of the SIDIS, where the transversity DF is convoluted with the chiral-odd Collins fragmentation function (see Chapter 2 for details), that describes the hadron emitted by a struck quark.
If we do not integrate over the transverse momentum p_T, other leading order DFs appear together with the three previously defined; all these p_T dependent functions are called Transverse Momentum Distributions (TMD's) [23]. Among them, the Sivers function, that describes the correlation between the transverse polarization of the target nucleon and the transverse momentum of quarks (see [19]), is of particular interest. Indeed, if we consider the cross section of SIDIS in which the lepton beam is unpolarized and the nucleon target is transversely polarized, a term where the Sivers function is involved appears in combination with the transversity term and therefore it has to be taken into account for investigating $\delta q(x)$. In addition, a non-zero Sivers function implies a non-zero orbital angular momentum of the quarks inside the nucleon and it has been related to the spatial distribution of the quarks inside the nucleon [21, 22].

The thesis is organized as follows: the theoretical framework of the semi-inclusive deep inelastic scattering is presented in Chapter 2. In Chapter 3 the main feature of the future planned high luminosity SIDIS experiments are summarized, with particular attention to the tracking systems. In Chapters 4 and 5 an improved phenomenological framework describing the nuclear structure of the ^{3}He is illustrated and applied to the experimental observables related with the neutron partonic structure. Finally, in Chapter 6 a new tracks filtering algorithm with a concrete application to the above described systems will be exposed.

Chapter 2

Transverse degrees of freedom of the nucleon

2.1 Polarized DIS in the parton model

The formalism of the deep inelastic scattering (DIS) by a polarized nucleon is illustrated in detail in several recent review (see e.g. [23]). Let us briefly summarize the basic ingredients of the theoretical description. We consider the process

$$l(\ell) + N(P) \to l(\ell') + X(P_X) \tag{2.1}$$

where a lepton l scatter off a polarized nucleon and in the final state only the outgoing lepton is detected. The cross section of this process is given in Born approximation by

$$\frac{d^6\sigma}{dx dy d\phi_S} = \frac{\alpha^2}{2sxQ^2} 2MW^{\mu\nu} L_{\mu\nu}, \tag{2.2}$$

where $q = \ell - \ell'$, $Q^2 = -q^2$, $x = Q^2/2P \cdot q$, $y = q \cdot P/\ell \cdot P$, $s = (\ell + P)^2$, ϕ_S the angle defined in Fig. 2.7, $L_{\mu\nu}$ the leptonic tensor and $W^{\mu\nu}$ the hadronic one. The leptonic tensor $L_{\mu\nu}$ contains all the information on the lepton electromagnetic interaction, which is described by the QED. In particular the above expression holds in Born approximation, namely the electromagnetic interaction is mediated by only one virtual photon and in this case $L_{\mu\nu}$ is defined as follows

$$\begin{aligned} L_{\mu\nu} &= \sum_{s_{l'}} \left[\bar{u}_{l'}(\ell', s_{l'}) \gamma_\mu u_l(\ell, s_l) \right]^* \left[\bar{u}_{l'}(\ell', s_{l'}) \gamma_\nu u_l(\ell, s_l) \right] \\ &= Tr \left[(\not{\ell} + m_l) \frac{1}{2} (1 + \gamma_5 \not{s}_l) \gamma_\mu (\not{\ell}' + m_l) \gamma_\nu \right]. \end{aligned} \tag{2.3}$$

where s_l is the lepton spin vector and m_l the lepton mass. All the information concerning the nucleon is contained in the hadronic tensor, which can be written by using a quantum field formalism in the framework of the QCD improved parton model, where the interaction of a high-Q^2 photon

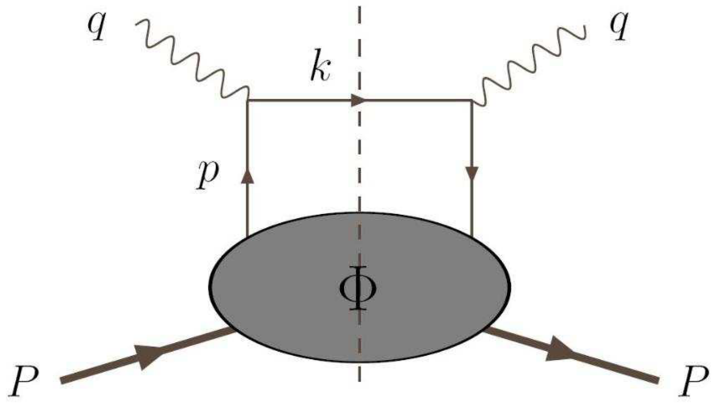

Figure 2.1: Handbag diagram for inclusive DIS.

with quasi-free particles, inside the nucleon, is taken into account. Then, the hadronic tensor $W_{\mu\nu}$ reads,

$$W_{\mu\nu}(P,S) = \sum_{q\bar{q}} e_q^2 \int \frac{d^4p}{(2\pi)^4}\delta((p+q)^2)\mathrm{Tr}[\Phi(p,P,S)\gamma_\mu(\not{p}+\not{q})\gamma_\nu], \tag{2.4}$$

where p the quark 4-momentum before hitting, $k = p + q$ the 4-momentum of the struck quark and S the nucleon polarization; the quark masses are neglected. In Eq. (2.4), $\Phi(p,P,S)$ is the *quark-quark correlation matrix*, that describes the quark dynamics inside the nucleon, namely it contains all the non perturbative QCD effects. It is given by

$$\Phi_{ij}(p,P,S) = \int d^4\xi e^{ip\cdot\xi} \left\langle P,S|\bar{\psi}_j(0)\psi_i(\xi)|P,S\right\rangle \tag{2.5}$$

where ψ is a quark spinor field, *i,j* are Dirac indexes and the sum over colors indexes is understood. In Fig. 2.1, it is shown the main contribution to DIS, that is pictorially represented by the so-called handbag diagram. An important step is represented by the expansion of Φ in terms of a Dirac basis given by

$$\Gamma = \{\mathbf{1}, \gamma^\mu, \gamma^\mu\gamma_5, i\gamma_5, i\sigma^{\mu\nu}\gamma_5\}, \tag{2.6}$$

where $\sigma^{\mu\nu} = i\left[\gamma^\mu, \gamma^\nu\right]/2$. In Eq. (2.6), $i\gamma_5$ and $i\sigma^{\mu\nu}\gamma_5 = -\epsilon^{\mu\nu\alpha\beta}\sigma_{\alpha\beta}/2$ are chosen for the sake of convenience, as discussed in [23]. Then one can write the following decomposition

$$\Phi\left(p,P,S\right) = \frac{1}{2}\left\{\mathcal{S}\mathbf{1} + \mathcal{V}_\mu\gamma^\mu + \mathcal{A}_\mu\gamma_5\gamma^\mu + i\mathcal{P}_5\gamma_5 + i\mathcal{T}_{\mu\nu}\sigma^{\mu\nu}\gamma_5\right\} \tag{2.7}$$

where the factors $\mathcal{S}$, $\mathcal{V}_\mu$, $\mathcal{A}_\mu$, $\mathcal{P}_5$ and $\mathcal{T}_{\mu\nu}$ are scalar, vector, axial-vector, pseudo-scalar and tensor functions, respectively. They properly depend upon the momenta p, P and the nucleon polarization S. The general form of the previous functions is imposed by the properties to be fulfilled by Φ, namely Lorentz invariance, parity, time reversal and hermiticity [23]. In the Infinite Momentum Frame (IMF), namely the reference frame where the masses of the partonic constituents and their transverse momenta can be neglected, the functions are ordered according to powers of $1/P^+$, where the leading order term is $(1/P^+)^{-1} = P^+$ and the next to leading order term is $(1/P^+)^0 = 1$, (see Appendix A for the details on light-cone formalism). The different powers correspond to the twist expansion, see e.g. [24], where the leading term is a twist-two contribution. By neglecting the transverse momentum of the quarks inside the nucleon, in leading order approximation, only $\mathcal{V}^\mu$, $\mathcal{A}^\mu$ and $\mathcal{T}^{\mu\nu}$ are nonzero quantities, and Φ reads

$$\Phi\,(p,P,S) = \frac{1}{2}\left\{A_1 \not{P} + A_2 \lambda_N \gamma_5 \not{P} + A_3 \not{P} \gamma_5 \not{S}_\perp\right\}, \tag{2.8}$$

where the high-energy approximation of the nucleon spin is assumed, i.e. $S^\mu \approx \lambda_N \frac{P^\mu}{M} + S^\mu_\perp$, with λ_N the nucleon helicity and $S^\mu_\perp$ the transverse polarization. The three amplitudes $A_i(p^2, p\cdot P)$ are real and they do not depend upon $(p\cdot S)^2$ for $J = 1/2$, since they are determined by the internal dynamics. Integrating the three amplitudes over p with the constraint $x = p^+/P^+$ (in the IMF $x = x_B$ the well known Bjorken variable), one gets three leading-twist DF's, viz

$$q(x) = \int \frac{d^4p}{(2\pi)^4} A_1(p^2, p\cdot P)\delta\left(x - \frac{p^+}{P^+}\right), \tag{2.9}$$

$$\Delta q(x) = \int \frac{d^4p}{(2\pi)^4} A_2(p^2, p\cdot P)\delta\left(x - \frac{p^+}{P^+}\right), \tag{2.10}$$

$$\delta q(x) = \int \frac{d^4p}{(2\pi)^4} A_3(p^2, p\cdot P)\delta\left(x - \frac{p^+}{P^+}\right). \tag{2.11}$$

where $q(x)$ is the *momentum* (spin-independent) distribution, $\Delta q(x)$ the *helicity* distribution and the third distribution, $\delta q(x)$, is called *transversity*. The first two functions have been measured with high accuracy by numerous experiments in the past decades [18]. The third one is remained unmeasured for a long time, due to its chiral-odd nature (see the following subsection for details). Analogous distributions, $\bar{q}(x)$,$\Delta\bar{q}(x)$,$\delta\bar{q}(x)$, can be introduced for the antiquarks. Integrating the distribution functions over x, one obtains the three leading-twist first moments:

$$q = \int_0^1 \left[q(x) - \bar{q}(x)\right] dx = g_V, \tag{2.12}$$

$$\Delta q = \int_0^1 \left[\Delta q(x) - \Delta\bar{q}(x)\right] dx = g_A, \tag{2.13}$$

$$\delta q = \int_0^1 \left[\delta q(x) - \delta\bar{q}(x)\right] dx = g_T, \tag{2.14}$$

where g_V, g_A and g_T are vector, axial and tensor charges of the nucleon, respectively. Summarizing, at leading-twist order the integrated quark-quark correlation matrix reads

$$\Phi(P,S) = \frac{1}{2}\left\{q(x)\not{P} + \lambda_N \Delta q(x)\gamma_5 \not{P} + \delta q(x)\not{P}\gamma_5 \not{S}_T\right\}. \tag{2.15}$$

2.1.1 Physical interpretation of the twist-two DFs

Momentum and helicity DFs yield the probability densities to find a quark with a given momentum fraction and a given polarization inside the nucleon. In order to understand the physical meaning, let us first of all decompose the quark fields as follows

$$\psi = \psi_{(+)} + \psi_{(-)} \tag{2.16}$$

where

$$\psi_{(\pm)} = \frac{1}{2}\gamma^{\mp}\gamma^{\pm}\psi \tag{2.17}$$

that is known as the *good*, $+$, (*bad*, $-$) part of the quark fields. Using

$$\begin{aligned}
\bar{\psi}\,\gamma^+\,\psi &= \sqrt{2}\,\psi^\dagger_{(+)}\,\psi_{(+)}\,, && (2.18a)\\
\bar{\psi}\,\gamma^+\gamma_5\,\psi &= \sqrt{2}\,\psi^\dagger_{(+)}\,\gamma_5\,\psi_{(+)}\,, && (2.18b)\\
\bar{\psi}\,i\sigma^{i+}\gamma_5\,\psi &= \sqrt{2}\,\psi^\dagger_{(+)}\,\gamma^i\gamma_5\,\psi_{(+)}\,. && (2.18c)
\end{aligned}$$

the leading-twist distributions (2.9–2.11) can be re-expressed as [20]

$$\begin{aligned}
q(x) &= \int \frac{d\xi^-}{2\sqrt{2}\,\pi} e^{ixP^+\xi^-}\langle PS|\psi^\dagger_{(+)}(0)\psi_{(+)}(0,\xi^-,\mathbf{0}_\perp)|PS\rangle\,, && (2.19a)\\
\Delta q(x) &= \int \frac{d\xi^-}{2\sqrt{2}\,\pi} e^{ixP^+\xi^-}\langle PS|\psi^\dagger_{(+)}(0)\gamma_5\psi_{(+)}(0,\xi^-,\mathbf{0}_\perp)|PS\rangle\,, && (2.19b)\\
\delta q(x) &= \int \frac{d\xi^-}{2\sqrt{2}\,\pi} e^{ixP^+\xi^-}\langle PS|\psi^\dagger_{(+)}(0)\gamma^1\gamma_5\psi_{(+)}(0,\xi^-,\mathbf{0}_\perp)|PS\rangle\,, && (2.19c)
\end{aligned}$$

and only the *good* component appears. The above expressions allows us to adress a fundamental issue: in Eqs. (2.9), (2.10) and (2.11) the variable x is not constrained to be less than 1 (as expected in view of the identification with the Bjorken variable).By inserting a complete set of intermediate states, e.g., in Eq. (2.19a), one can obtain the desired upper bound. As a matter of fact, one gets

$$q(x) = \frac{1}{\sqrt{2}} \sum_n \delta\big((1-x)P^+ - P_n^+\big)\,|\langle PS|\psi_{(+)}(0)|n\rangle|^2\,. \tag{2.20}$$

and therefore

$$1 - x = \frac{P_n^+}{P^+} \geq 0 \tag{2.21}$$

Notice that the positivity of the plus components of a physical particle has been exploited . Moreover, Eq. 2.19a clearly shows the physical meaning of $f(x)$, that gives the probability of finding inside the nucleon a quark (irrespective of its polarization) with longitudinal-momentum fraction p^+/P^+. Let us now consider the distribution (2.19b). By using the projector $\mathcal{P}_\pm = \frac{1}{2}\,(1 \pm \gamma_5)$ we obtain

$$\begin{aligned}
\Delta q(x) &= \frac{1}{\sqrt{2}} \sum_n \delta\big((1-x)P^+ - P_n^+\big)\\
&\quad \times \Big\{ \big|\langle PS|\mathcal{P}_+\psi_{(+)}(0)|n\rangle\big|^2 - \big|\langle PS|\mathcal{P}_-\psi_{(+)}(0)|n\rangle\big|^2 \Big\}\,, && (2.22)
\end{aligned}$$

Adopting the helicity basis for a fermion, Eq. (2.22) yields difference between the number density of quarks with positive helicity and the one with negative helicity. To summarize, the Dirac structures $\gamma_0\gamma^+$ and $\gamma_0\gamma^+\gamma_5$ are diagonal in the helicity basis, (i.e. they commute with the helicity operator, for massless particles reduces to $\gamma_5/2$), therefore the momentum distribution $q(x)$ and $\Delta q(x)$ assume a clear probabilistic meaning. By using the helicity basis, one can write the unpolarized DF as follows

$$q(x) = q^{\rightrightarrows}(x) + q^{\leftrightarrows}(x) \tag{2.23}$$

where $q^{\rightrightarrows}(x)$ ($q^{\leftrightarrows}(x)$) is the probability distribution to find a quark with helicity aligned (antialigned) to the nucleon polarization. As to the helicity DF one gets

$$\Delta q(x) = q^{\rightrightarrows}(x) - q^{\leftrightarrows}(x). \tag{2.24}$$

It gives the difference between the probability distribution of finding, in a longitudinally polarized nucleon, quarks with spin aligned or anti-aligned respect to the nucleon spin.

Differently the Dirac structure in $\gamma_0\gamma^+\gamma^i\gamma_5$ is not diagonal in the helicity basis. Therefore we do not have an immediate probabilistic interpretation for the transverisity DF. However, one can recover a probabilistic interpretation by adopting the basis of transverse spin eigenstates $|\downarrow\rangle$ and $|\uparrow\rangle$, which are defined as linear combination of helicity eigenstates, $|+\rangle$ and $|-\rangle$, namely

$$|\uparrow\rangle = \frac{1}{\sqrt{2}}(|+\rangle + i\,|-\rangle)\,, \qquad |\downarrow\rangle = \frac{1}{\sqrt{2}}(|+\rangle - i\,|-\rangle)\,, \tag{2.25}$$

Indeed, using the projector $\mathcal{P}_{\uparrow\downarrow} = \frac{1}{2}(1 \pm \gamma^1\gamma_5)$ we find

$$\begin{aligned} \delta q(x) &= \frac{1}{\sqrt{2}} \sum_n \delta\left((1-x)P^+ - P_n^+\right) \\ &\quad \times \left\{ \left|\langle PS|\mathcal{P}_\uparrow \psi_{(+)}(0)|n\rangle\right|^2 - \left|\langle PS|\mathcal{P}_\downarrow \psi_{(+)}(0)|n\rangle\right|^2 \right\}. \end{aligned} \tag{2.26}$$

Then, the transversity $\delta q(x)$ can be interpreted as the probability distribution to find a quark with its spin aligned along the transverse spin of the nucleon minus the probability distribution of an opposite alignment; viz.

$$\delta q(x) = q^{\Uparrow\uparrow}(x) - q^{\Uparrow\downarrow}(x). \tag{2.27}$$

Furthermore, in the IMF helicity and chirality coincide and therefore transversity (not diagonal in the helicity basis) is a chiral-odd function. For this reason, since electromagnetic and strong interactions conserve chirality, transversity is not measurable through DIS experiments. In these inclusive processes, the strong interaction affects Φ only, since possible hadronic interactions in the final state can be safely disregarded. Differently, in SIDIS the meson production vertex can flip quark helicity and this allows one to experimentally access the transverse quark distribution. The probabilistic interpretation of the three distributions immediately leads to the following inequalities

$$|\Delta q(x)| \leq q(x), \qquad |\delta q(x)| \leq q(x). \tag{2.28}$$

Indeed, there is a third subtle inequality involving simultaneously all the leading twist distributions, the so called Soffer inequality [23]:

$$2\,|\delta q(x)| \leq q(x) + \Delta q(x). \tag{2.29}$$

In conclusion, it is worth noting that the three inequalities are preserved by QCD evolution.

2.1.2 Transverse momentum dependent distribution functions

In the leading-twist description of DIS, the transverse component of the quark momentum, $\vec{p}_\perp$, is not important, since in the IMF, it is suppressed by one power of P^+ and is small compared with the longitudinal component of the momentum. Therefore, in the description of DIS within the parton model, the parton DF depends only upon x, i.e. the longitudinal fraction of the target momentum carried by a parton. It should pointed out that given the basically non-perturbative effects in the bound state, parton DF's cannot be obtained by perturbative QCD and due to the limitations in the present lattice QCD calculations, the parton DF's are phenomenologically extracted from DIS experimental data, obtained in a extremely large intervals of Q^2 [9, 10].
The transverse component plays an important role in the description of high order perturbative QCD and in soft non perturbative hadronic processes. For instance it is important in the description of many single spin effects recently observed in SIDIS processes, where a hadron is detected in the final state in coincidence with the scattered lepton.

The quark momentum can be decomposed as follows

$$k^\mu \simeq xP^\mu + p_T^\mu\,, \tag{2.30}$$

where p_T^μ is the transverse momentum of the parton in the nucleon. Then, additional leading-twist amplitudes appear in the tensor $\mathcal{T}^{\mu\nu}$ and axial $\mathcal{A}^\mu$ components of the correlation matrix (cf Eq. (2.7) and Ref. [23]), once the p_T dependence is taken into account. The quark–quark correlation matrix then reads

$$\begin{aligned}\Phi(p,P,S) \;=\; & \frac{1}{2}\{A_1\,\not{P} + A_2\lambda_N\gamma_5\,\not{P} + A_3\,\not{P}\gamma_5\,\not{S}_\perp \\ & + \frac{1}{M}\widetilde{A}_1\boldsymbol{p}_T\cdot\boldsymbol{S}_\perp\gamma_5\,\not{P} + \widetilde{A}_2\frac{\lambda_N}{M}\,\not{P}\gamma_5\,\not{p}_T \\ & + \frac{1}{M^2}\widetilde{A}_3\boldsymbol{p}_T\cdot\boldsymbol{S}_\perp\,\not{P}\gamma_5\,\not{p}_T\Big\}\,.\end{aligned} \tag{2.31}$$

If p_T is not integrated out one obtains six transverse momentum distribution functions (TMDs): $q(x,p_T^2)$, $\Delta q(x,p_T^2)$, $h_{1T}(x,p_T^2)$, $h_{1T}^\perp(x,p_T^2)$, $g_{1T}(x,p_T^2)$ and $h_{1L}^\perp(x,p_T^2)$ [1]. In particular the letters g and h indicate the longitudinal and transverse polarization of the quark, respectively, the subscripts L= longitudinal and T= transverse indicate the polarization of the nucleon, finally the subscript 1 indicates the leading-twist order of the expantion and the superscript $\perp$ indicates that,

[1]This notation historically used in DIS, has been usually changed in the context concerning TMDs. One usually finds in literature $q \equiv f_1$, $\Delta q \equiv g_{1L}$ and $\delta q \equiv h_{1T}$.

if integrated over p_T, the corresponding DF vanishes. The first four TMDs, after integrating out over p_T with proper weights, lead to

$$q(x) = \int d^2\vec{p}_T q(x, p_T^2), \tag{2.32}$$

$$\Delta q(x) = \int d^2\vec{p}_T \Delta q(x, p_T^2), \tag{2.33}$$

$$\delta q(x) = \int d^2\vec{p}_T \left\{ h_{1T}^q(x, p_T^2) + \frac{p_T^2}{2M^2} h_{1T}^{\perp q}(x, p_T^2) \right\} = \int d^2 p_T^2 \delta q(x, p_T^2). \tag{2.34}$$

The two remaining transverse distributions g_{1T} and $h_{1L}^{\perp}$ are completely new.
It is also useful to define the moments of a generic distribution function $d(x, p_T^2)$:

$$d^{(1/2)}(x) \equiv \int d^2\vec{p}_T d^{(1/2)}(x, p_T^2) \equiv \int d^2\vec{p}_T \frac{|\vec{p}_T|}{2M} d(x, p_T^2), \tag{2.35}$$

$$d^{(n)}(x) \equiv \int d^2\vec{p}_T d^{(n)}(x, p_T^2) \equiv \int d^2\vec{p}_T \left(\frac{|\vec{p}_T|^2}{2M} \right)^n d(x, p_T^2), \tag{2.36}$$

where n is a integer number.

2.1.3 Sivers and Boer-Mulders distribution functions

Two more twist-two DFs must be considered if one takes into account the Wilson line operator in the correlation function. In order to fulfill the gauge invariance of the correlation function, a gauge link operator $\mathcal{L}$ must be inserted between the quark fields [19]:

$$\Phi_{ij}(p.P, S) = \frac{1}{(2\pi)^4} \int d^4\xi e^{ip\cdot\xi} \left\langle P, S | \bar{\psi}_j(0) \mathcal{L}(0, \xi) \psi_i(\xi) | P, S \right\rangle, \tag{2.37}$$

where

$$\mathcal{L}(0, \xi) = \mathcal{P}exp\left(-i\sqrt{4\pi\alpha_S} \int_0^\xi ds^\mu \mathcal{A}_\mu(s) \right), \tag{2.38}$$

is a bilocal operator connecting the quark fields in two different points of the space-time. $\mathcal{P}$ indicates the path-ordering of the integral over the gauge field $\mathcal{A}_\mu$. This operator, called also Wilson line, takes into account the sum of all the diagrams with soft gluon exchanges. The invariance under time-reversal, in absence of gauge link (recall that for the light cone gauge $\mathcal{A}^+ = 0$ and chosing a suitable pattern one has $\mathcal{L} = 1$), generates the following constraint for the correlation function [23]:

$$\Phi^*_{\mathcal{L}=1}(p, P, S) = \gamma_5 C \Phi_{\mathcal{L}=1}(\tilde{p}, \tilde{P}, \tilde{S}) C^\dagger \gamma_5, \tag{2.39}$$

where $C = i\gamma^2\gamma^0$ and the tilde four-vectors are defined as $\tilde{p}^\mu = (p^0, -\vec{p})$. Obviously, T-odd terms in Φ will change sign on the right-hand side and therefore they are forbidden. Differenetly, with the insertion of $\mathcal{L}$ in Φ and taking a perturbative expansion, time–reversal invariance does not constrain the T–odd DFs (in leading twist) to be zero [25]. The colliding particles interact strongly with non-trivial relative phases and the transformation of interacting final states into initial

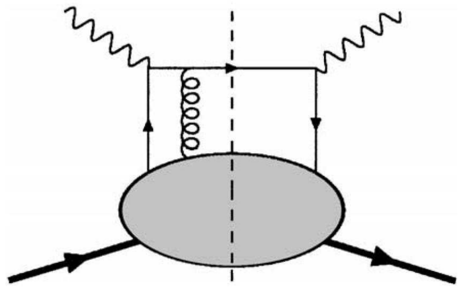

Figure 2.2: Higher-twist contribution to DIS involving quark-quark-gluon correlation.

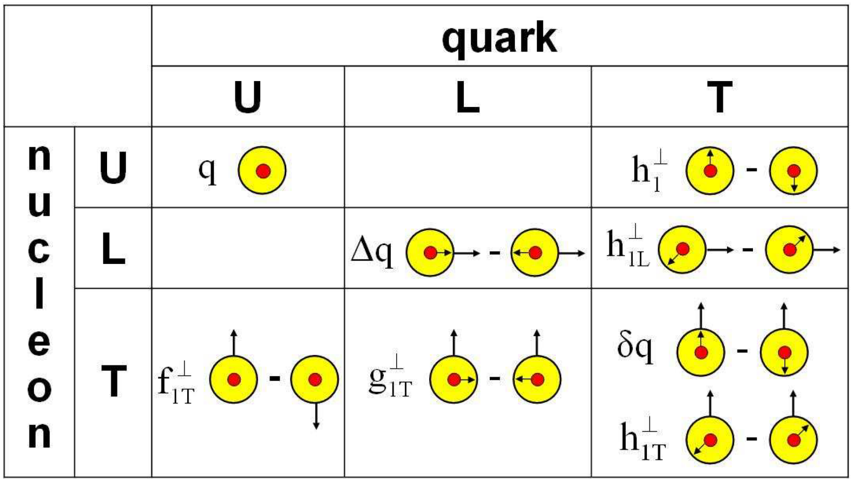

Figure 2.3: Leading-twist transverse momentum dependent quark distribution functions. The external arrows indicate the target polarization, while the internal ones the quark polarization. (Let us remind again that usually in literature one has a different notation $q \equiv f_1$, $\Delta q \equiv g_{1L}$ and $\delta q \equiv h_{1T}$).

states is not as simple as for non-interacting final state. Therefore, in the actual case, time-reversal invariance cannot be implemented by naïvely imposing the condition (2.39), that holds only if the strong interaction in the final state is disregarded. Summarizing, "T-odd" terms that are not present in the correlation function, (2.31), when the condition $\mathcal{L} = 1$ is fulfilled, rather than violating time-reversal invariance,are fundamentantal for restoring the invariance itself in the case when the condition $\mathcal{L} \neq 1$ has to be considered. The first naïve T-odd distribution function was proposed by Sivers [19] for explaining single-spin asymmetries observed in pion production by proton-proton scattering. It is related to the probability density of unpolarized quarks in a transversely polarized nucleon and is denoted by $f_{1T}^\perp(x, p_T^2)$. The special interest for the *Sivers function* is due to the fact that a non zero Sivers function implies a nonzero orbital angular momentum of the quarks within the nucleon [21, 22]. The presence of an orbital contribution to the spin sum-rule should be useful for explaining the present discrepancy in the nucleon spin sum rule (cf. Eq. (1.1)).
There is also a second T-odd distribution function, the *Boer-Mulders function*, $h_1^\perp(x, p_T^2)$, that

measure the probability density of transversely polarized quarks in an unpolarized nucleon. Also for T-odd distribution functions exist bounds that ensure the positivity, see e.g. [26]:

$$|f_{1T}^{\perp(1)q}(x, p_T^2)| \leq q^{(1/2)}(x, p_T^2), \tag{2.40}$$

$$|h_1^{\perp(1)q}(x, p_T^2)| \leq q^{(1/2)}(x, p_T^2). \tag{2.41}$$

Fig. 2.3 summarizes all the 8 leading-order TMDs. It is interesting to emphasize that one could naively assume that the TMDs are universal observables describing the quark and gluon content of the nucleon. In contrast to such an expectation, due to the gauge nature of QCD, the Sivers function mesured in the SIDIS has to be of the same magnitude but opposite in sign with respect to the Sivers function measured in DY [29]. In the next future, when measurement of sufficient precision will be available, the experimental test of this theorem will give a prove of the gauge nature of QCD.

2.1.4 Sub-leading–Twist Distribution Functions

By taking into account twist-three amplitudes, e.g. terms of order$(1/P^+)^0$, in the correlation function, six new DFs appear. After integrating over p_T one recovers three T-even functions

$$e^q(x), \qquad h_L^q(x), \qquad g_T^q(x) \tag{2.42}$$

and three T-odd ones

$$h^q(x), \qquad e_L^q(x), \qquad f_T^q(x) \tag{2.43}$$

where L and T indicate a longitudinal and transversely polarized nucleon respectively. They do not have a trivial interpretation in terms of partonic distributions, since various kinematical and dynamical effects contribute to higher twists, e.g. quarks masses, intrinsic transverse momenta and gluon interactions. As a consequence, it is possible to decompose [27] twist-three distribution functions in three parts: a quark mass term, a term related to the leading-twist distributions and an interaction dependent term. The last term arises from non-handbag diagrams, like the one shown in Fig.(2.2), where the gluon is a hard gluon and the introduction of a quark-quark-gluon correlation function is required. Among the six twist-three functions, $g_T^q(x)$ is of particular interest, since it is related to the nucleon polarized structure function $g_2(x)$ by:

$$g_1(x) + g_2(x) = \frac{1}{2}\sum_{q,\bar{q}} e_q^2 g_T^q(x), \tag{2.44}$$

where $g_1(x) = \frac{1}{2}\sum_{q,\bar{q}} e_q^2 \Delta q(x)$. A simple partonic picture of $g_2(x)$ does not exist. According to [27], one can decompose $g_T^q(x)$ as follows

$$g_T^q(x) = \frac{m_q}{M}\delta q(x) + \frac{1}{x} g_{1T}^{(1)q}(x) + \tilde{g}_T^q(x), \tag{2.45}$$

where transversity is weighted by a tiny factor m_q/M and $\tilde{g}_T$ contains the interaction effect.

2.1.5 How to measure transversity

As mentioned before, helicity conservation prevents the possibility to measure transversity in DIS, since in order to experimentally observe a chiral-odd object it is necessary that it appears in combination with another chiral-odd quantity, given the global chiral invariance. There are basically two processes that can be used to measure transversity: the transversely polarized Drell-Yan processes in proton-proton scattering, with a transversely polarized proton and an unpolarized one, and the SIDIS measurements, in which at least one final state hadron is detected in coincidence with the scattered lepton. In the case of the proton-proton scattering, due to the one-gluon exchange, the transversity distribution of a quark can be measured in combination with a distribution of an anti-quark, belonging to the sea of the other proton. A valence-quark tranversity distribution is expected to be larger than a sea quark one. If this is true, then the asymmetry[2] measured in a polarized DY $p\bar{p}$ process should be larger than the one for a pp process. This can be understood by considering that in the first case there is a product of two valence quark DF, while in the second case the product is between a valence distribution and a sea distribution. Unfortunately, proton-antiproton polarized experiments are very difficult to be performed and up to now there is only a proposal [28] that aims at performing this kind of measurement. In SIDIS, Fig.(2.4), tranversity enters the cross section in combination with a chiral-odd fragmentation function. Identifying the produced hadrons, it is possible to extract information about the parent quarks. In the recent past, HERMES and COMPASS experiments have made this kind of measurements, with high precision, but only for proton and deuterium [18]. A specific scientific program will start in the next years at Thomas Jefferson Lab National Accelerator Facility (JLAB), with the aim of systematically extending these measurements to the neutron (some measurements on neutron has been done using polarized ^{3}He as an effective neutron target as will be outlined in the last Subsection).

2.2 Semi-Inclusive Deep inelastic Scattering

Let us consider the case in which one hadron, with four-momentum P_h, is detected in coincidence with the scattered lepton, then we have (cf. Fig.(2.4)):

$$l(\ell) + N(P) \to l(\ell') + h(P_h) + X(P_X) \tag{2.47}$$

where l and N are the incident lepton and the nucleon target; while h and X are the produced hadron and the undetected hadronic remnant, respectively. In brakets there are the corresponding four-momenta. With respect to DIS, the investigation of SIDIS requires a new ingredient, that describes the transition from partonic degrees of freedom to final hadronic ones: namely the

[2]When both hadrons are transversely polarised, the typical observables are double-spin transverse asymmetries of the form

$$A_{TT}^{DY} = \frac{d\sigma(\vec{S_T},\vec{S_T}) - d\sigma(\vec{S_T},-\vec{S_T})}{d\sigma(\vec{S_T},\vec{S_T}) + d\sigma(\vec{S_T},-\vec{S_T})} \tag{2.46}$$

, and the good candidate process for measuring transversity in doubly polarized pp ($p\bar{p}$) collisions is Drell–Yan lepton pair production, where the lowest order Drell-Yan asymmetry contains the product of two transversity functions belonging to the two hadrons [23].

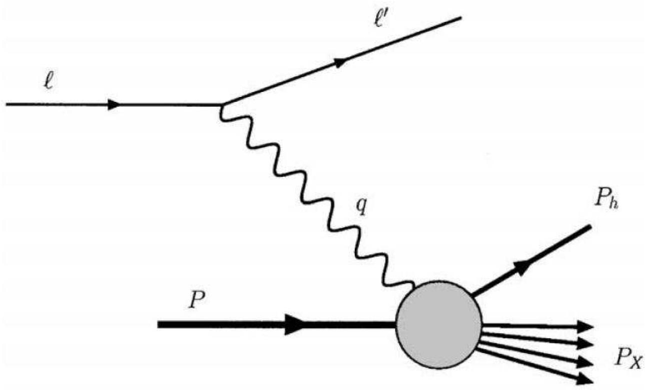

Figure 2.4: Feynman diagram for Semi-Inclusive Deep Inelastic Scattering.

so-called *fragmentation* or *hadronizzation* process. It is worth noting that the hadronization is a completely non perturbative QCD process. Moreover, the analysis of SIDIS involves the *factorization theorem*, which states that in hard scattering processes one assume are universal parton DFs and fragmentation functions (FFs) (that represent the probability for a parton to fragment into a particular hadron, carrying a certain fraction of the parton momentum). This means that parton DFs and FFs needed for describing DIS, DY, e^+e^- or *pp* hard processes, must be always the same, while the hard scattering cross section is different. In the case of the lepto-production of a hadron *h*, the cross section can be factorized as follows:

$$\frac{d^3\sigma^h}{dxdQ^2dz} = \sum_{a,b=q,\bar{q},g} d_a(x,Q^2) \otimes \sigma_{ab}(x,Q^2) \otimes F_b^h(z,Q^2), \tag{2.48}$$

where $z = P \cdot p / P \cdot q \overset{lab}{=} E_h/\nu$ is the energy fraction of the final hadron, $d_a(x,Q^2)$ describes the distribution of the parton *a* in the nucleon, σ_{ab} is the hard-scattering cross section for the process $la \to l'b$ (calculable in perturbative QCD) and $F_b^h(z,Q^2)$ describes the fragmentation of the final parton *b* into hadron *h* carrying a fraction of energy *z*. The FFs, related to the three lightest quark flavours (u,d,s) can be assigned, by applying charge conjugation and isospin simmetry, in three categories: favorite (*fav*), unfavorite (*unfav*) and strange (*s*), depending on the flavor of the fragmenting quark and on the quark content of the produced hadron. For example, for fragmentation into pions one has:

$$F_{fav}(z,Q^2) = F_u^{\pi^+}(z,Q^2) = F_{\bar{u}}^{\pi^-}(z,Q^2) = F_{\bar{d}}^{\pi^+}(z,Q^2) = F_d^{\pi^-}(z,Q^2), \tag{2.49}$$

$$F_{unfav}(z,Q^2) = F_u^{\pi^-}(z,Q^2) = F_{\bar{u}}^{\pi^+}(z,Q^2) = F_{\bar{d}}^{\pi^-}(z,Q^2) = F_d^{\pi^+}(z,Q^2), \tag{2.50}$$

$$F_s(z,Q^2) = F_s^{\pi^+}(z,Q^2) = F_{\bar{s}}^{\pi^-}(z,Q^2) = F_{\bar{s}}^{\pi^+}(z,Q^2) = F_s^{\pi^-}(z,Q^2). \tag{2.51}$$

Similar expressions hold for kaons. From Eqs. (2.49) and (2.50), the FFs for neutral pions are defined by:

$$F^{q\to\pi^0}(z) = \frac{1}{2}\left\{F_q^{\pi^+}(z) + F_q^{\pi^-}(z)\right\} = \frac{1}{2}\left\{F_{fav}(z) + F_{unfav}(z)\right\} \tag{2.52}$$

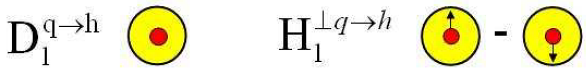

Figure 2.5: The leading-twist transverse momentum dependent fragmentation functions. The struck quark (produced hadron) is represented as a small red (big yellow) circle.

All these FFs are not calculable from first principles and they are extracted from experimental data through global fits.

2.2.1 The Hadronic tensor in SIDIS

The hadronic tensor for semi-inclusive DIS must take into account the fragmentation of the struck quark. This can be accomplished by introducing a new quark- quark correlation function, that describes the fragmentation process of the quark after absorbing the virtual photon. Then $W^{\mu\nu}$ reads

$$W^{\mu\nu}(P,S,P_h,S_h) = \sum_{q,\bar{q}} e_q^2 \int d^4p\, d^4k\, \delta^4(p+q-k)\mathrm{Tr}\left[\Phi(p,P,S)\gamma^\mu\Delta(k,P_h,S_h)\gamma^\nu\right]. \quad (2.53)$$

The new correlator Δ is given by

$$\Delta_{ij} = \frac{1}{(2\pi)^4}\int d^4\xi e^{ik\cdot\xi} \langle 0|\psi_i(\xi)|P_h,S_h\rangle \langle P_h,S_h|\bar{\psi}_j(0)|0\rangle\,, \quad (2.54)$$

The correlation function Δ can be decomposed in the same Dirac basis (2.6), as in the case of Φ. Including the intrinsic transverse component of the final hadron momentum, K_T, eight leading-twist fragmentation functions are obtained. However at leading-twist, assuming the unpolarized and transversely polarized case only (namely, the most interesting cases to dealing with the quark orbital angular momentum) and after summing over the spin of the produced hadron S_h , only the spin-independent fragmentation function $D_1^q(z,K_T^2)$ and the so-called *Collins function*, $H_1^{\perp q}(z,K_T^2)$ chiral-odd and T-odd), [30] remain.

2.2.2 Probabilistic interpretation of leading-twist FFs

The two leading-twist fragmentation functions, as the leading-twist distribution functions, have a direct probabilistic interpretation. $D_1^q(z,K_T^2)$ represents the probability density that a struck quark of flavor q fragments into a hadron h, carrying longitudinal momentum fraction z of the fragmenting quark, and transverse momentum K_T, in the intrinsic frame of the fragmenting quark[3]. Instead, $H_1^{\perp q}(z,K_T^2)$ is the difference of the probability densities of quarks with opposite transverse spin to fragment into a final hadron with transverse momentum K_T (see Figure 2.5). The Collins function like the Sivers function vanishes if it is integrated over the intrinsic transverse momentum. D_1^q does not change sign under chirality and time reversal transformation. Differently, $H_1^{\perp q}$

[3] $\vec{K}_T$ is the transverse momentum of the hadron h with respect to the fragmenting quark. If the transverse motion of quarks inside the target is ignored, $\vec{K}_T$ coincides with $\vec{P}_{h\perp}$ defined in Fig.2.7 (see [23]).

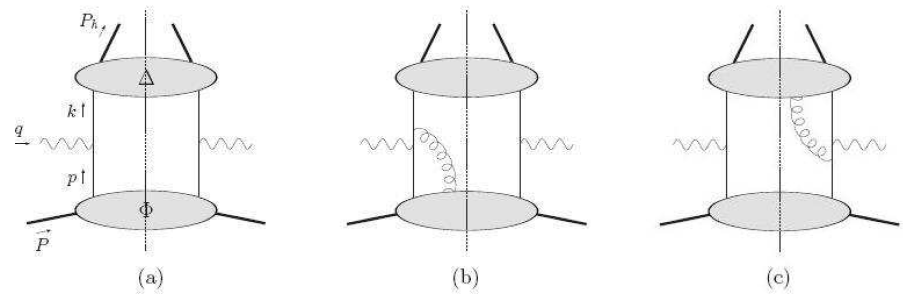

Figure 2.6: Extended handbag diagrams for semi-inclusive DIS.

is chiral-odd and T-odd. For the Collins FF, there are no problems similar to the case of Sivers TMD, namely there are no constraints deriving from time-reversal invariance, due to the presence in the final state of the undetected hadron X together with the detected hadron h. It has been shown [31, 32] that the final state interaction, present in the upper blobs in Fig.(2.6), by itself justifies the existence of T-odd fragmentation functions. As in the case of distribution functions, it is convenient to introduce the moments, namely:

$$F^{1/2}(z) \equiv z^2 \int d^2\vec{k}_T F^{(1/2)}(z, z^2 k_T^2) \equiv z^2 \int d^2\vec{k}_T \frac{|\vec{k}_T|}{2M_h} F(z, z^2 k_T^2), \tag{2.55}$$

$$F^n(z) \equiv z^2 \int d^2\vec{k}_T F^n(z, z^2 k_T^2) \equiv z^2 \int d^2\vec{k}_T \left(\frac{|\vec{k}_T|}{2M_h}\right)^n F(z, z^2 k_T^2), \tag{2.56}$$

with $\vec{K}_T = -z\vec{k}_T$, where $\vec{k}_T$ is the transverse momentum of the fragmenting quark, n is an integer and F is a generic transverse momentum dependent fragmentation function. From the positivity constraint, the following inequality, see [33], can be obtained

$$\left| H_1^{\perp(1)}(z, z^2 k_T^2) \right| \leq D_1^{(1/2)}(z, z^2 k_T^2). \tag{2.57}$$

2.2.3 The Cross section

The differential cross section for the reaction in (2.47) is given by:

$$\frac{d^6\sigma}{dx dy dz d\phi_S dP_{h\perp}^2} = \frac{\alpha^2 y}{8zQ^4} 2MW^{\mu\nu} L_{\mu\nu}, \tag{2.58}$$

where x and z are the quantities defined in the previous section, $y = P \cdot q / P \cdot \ell \overset{lab}{=} \nu/E$ is the energy fraction of the virtual photon with respect to the incoming lepton and $L_{\mu\nu}$ is the leptonic tensor. Moreover, ϕ_S is the azimuthal angle (around the virtual photon direction, i.e. with respect to the the z-axis $\equiv \hat{q}$) between the transverse component of the target spin vector, $\vec{S}_T$, and the scattering plane, while ϕ is the azimuthal angle between the scattering plane and the plane where the hadron is produced (see Fig. (2.7)). The differential cross section of the semi-inclusive process

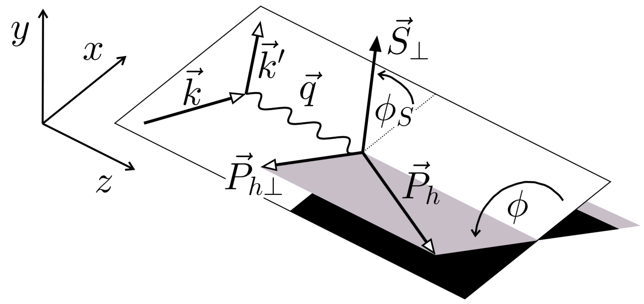

Figure 2.7: Definition of the azimuthal angles ϕ and ϕ_S between scattering plane (in white), the hadron-production plane (grey) and the transverse component of the nucleon spin vector $\vec{S_\perp}$ (or $\vec{S_T}$). The lepton momenta $\vec{k}$ and $\vec{k}'$ in figure are named $\vec{\ell}$ and $\vec{\ell}'$ in the text.

can be written in a model independent way according to [34], as follows

$$\begin{aligned}
\frac{d^6\sigma}{dxdydzd\phi_S dP_{h\perp}^2} &= \frac{\alpha^2}{xyQ^2}\frac{y^2}{2(1-\epsilon)}\left(1+\frac{\gamma^2}{2x}\right)\{F_{UU,T}+\epsilon F_{UU,L} \\
&+ \sqrt{2\epsilon(1+\epsilon)}\, cos\phi F_{UU}^{cos\phi} + \epsilon\, cos(2\phi) F_{UU}^{cos(2\phi)} + \lambda_e\sqrt{2\epsilon(1-\epsilon)}\, sin\phi F_{UL}^{sin\phi} \\
&+ S_L\left[\sqrt{2\epsilon(1+\epsilon)}\, sin\phi F_{UL}^{sin\phi} + \epsilon\, sin(2\phi) F_{UL}^{sin(2\phi)}\right] \\
&+ |S_T|\left[sin(\phi-\phi_S)\left(F_{UT,T}^{sin(\phi-\phi_S)} + \epsilon F_{UT,L}^{sin(\phi-\phi_S)}\right)\right. \\
&+ \epsilon\, sin(\phi+\phi_S) F_{UT}^{sin(\phi+\phi_S)} + \epsilon sin(3\phi-\phi_S) F_{UT}^{sin(3\phi-\phi_S)} \\
&+ \left.\sqrt{2\epsilon(1+\epsilon)} sin\phi_S\, F_{UT}^{sin\phi_S} + \sqrt{2\epsilon(1+\epsilon)} sin(2\phi-\phi_S)\, F_{UT}^{sin(2\phi-\phi_S)}\ \right] \\
&+ |S_T|\lambda_e\left[\sqrt{1-\epsilon^2}\, cos(2\phi-\phi_S) F_{LT}^{cos(\phi-\phi_S)} + \sqrt{2\epsilon(1-\epsilon)}\, cos\phi_S F_{LT}^{cos\phi_S}\right. \\
&+ \left.\sqrt{2\epsilon(1-\epsilon)}\, cos(2\phi-\phi_S) F_{LT}^{cos(2\phi-\phi_S)}\ \right]\}
\end{aligned} \tag{2.59}$$

The first two subscripts in the structure function F indicate the polarization of beam and the target (U = unpolarized, L=longitudinally polarized, T=transversely polarized), respectively. The third subscript indicates the polarization of the virtual photon and the superscript the angular multiplication factor. Moreover, λ_e indicates the helicity of the lepton beam, the target polarization S_L and S_T (with respect to $\hat{z} = \hat{q}$) are given by

$$S_T = \frac{cos\theta}{\sqrt{1-sin^2\theta sin^2\phi_S}} P_T, \qquad S_L = \frac{sin\theta cos\phi_S}{\sqrt{1-sin^2\theta sin^2\phi_S}} P_T \tag{2.60}$$

where P_T is the transverse polarization of the target respect to the beam direction, $cos\theta = \hat{\ell}\cdot\hat{q}$, $sin\theta = \gamma\sqrt{(1-y-\frac{1}{4}y^2\gamma^2)/(1+\gamma^2)}$ with $\gamma = 2xM_n/Q$, where M_n is the nucleon mass. Finally,

$$\epsilon = \frac{1-y-\frac{\gamma^2y^2}{4}}{1-y+\frac{y^2}{2}+\frac{\gamma^2y^2}{4}} \tag{2.61}$$

is the ratio between the longitudinal and transverse photon fluxes, see [34, 35] for details. In order to emphasize the beam and target polarization in the differential cross section, Eq. (2.59) can be recast in the following way (notice that for simplifying the notation, we drop out the denominator present in the left hand side of (2.59)).

$$d^6\sigma = d^6\sigma_{UU} + d^6\sigma_{LU} + d^6\sigma_{UL} + d^6\sigma_{LL} + d^6\sigma_{UT} + d^6\sigma_{LT}, \tag{2.62}$$

where each therms has the general form:

$$d^6\sigma_{\text{Beam Target}} = \frac{2\alpha^2}{sxy^2} \cdot K(y) \cdot \mathcal{A}(\phi, \phi_S) \cdot \sum_{q\bar{q}} e_q^2 \mathcal{I}[\mathcal{W} \cdot d \cdot F]. \tag{2.63}$$

where $K(y)$ is a kinematical factor that corresponds to one of the following quantities [34]

$$A(y) = \left(1 - y + \frac{y^2}{2} - \frac{y^2\gamma^2}{4}\right)\frac{1}{1+\gamma^2}, \tag{2.64a}$$

$$B(y) = \left(1 - y - \frac{y^2\gamma^2}{4}\right)\frac{1}{1+\gamma^2}, \tag{2.64b}$$

$$C(y) = \frac{1}{\sqrt{1+\gamma^2}} y \left(1 - \frac{y}{2}\right), \tag{2.64c}$$

$$D(y) = \frac{2(2-y)}{1+\gamma^2}\sqrt{1 - y - \frac{y^2\gamma^2}{4}}, \tag{2.64d}$$

and $\mathcal{A}(\phi, \phi_S)$ is a sinusoidal oscillating term dependent upon a combination of the angles ϕ and ϕ_S defined in Figure 2.7. In Eq. (2.63), $I[\mathcal{W} \cdot d \cdot F]$ is a proper integral given by

$$\mathcal{I}[\mathcal{W} dF] = \int d^2\vec{p}_T d^2\vec{k}_T \delta^2\left(\vec{p}_T - \vec{k}_T - \frac{\vec{P}_{h\perp}}{z}\right)\mathcal{W}(\vec{p}_T, \vec{k}_T) d_q(x, p_T^2) F_q(z, z^2 k_T^2) \tag{2.65}$$

where $\mathcal{W}$ is a weight function, d_q is a distribution function and F_q is a fragmentation function. In particular we are interested in the following two structure functions that contain δq and $f_{1T}^{\perp}$:

$$F_{UT}^{sin(\phi+\phi_S)} \propto \mathcal{I}\left[-\frac{\hat{P}_{h\perp}\cdot\vec{k}_T}{M}\delta q H_1^{\perp}\right], \tag{2.66}$$

$$F_{UT}^{sin(\phi-\phi_S)} \propto \mathcal{I}\left[-\frac{\hat{P}_{h\perp}\cdot\vec{p}_T}{M} f_{1T}^{\perp} D_1\right], \tag{2.67}$$

with the versor $\hat{P}_{h\perp} = \frac{P_{h\perp}}{|P_{h\perp}|}$. It is worth noting that in (2.66) and (2.67), δq and $f_{1T}^{\perp}$ appear in combination with the Collins function and the spin independent fragmentation function, respectively. Then the contributions to σ_{UT} reads

$$d^6\sigma_{UT}(\phi + \phi_S) = -\frac{2\alpha^2}{sxy^2}|\vec{S}_T| B(y) sin(\phi + \phi_S) \sum_{q\bar{q}} e_q^2 \mathcal{I}\left[-\frac{\hat{P}_{h\perp}\cdot\vec{k}_T}{M}\delta q(x, p_T^2) H_1^{\perp q}(z, z^2 k_T^2)\right], \tag{2.68}$$

$$d^6\sigma_{UT}(\phi-\phi_S) = -\frac{2\alpha^2}{sxy^2}|\vec{S}_T|A(y)sin(\phi-\phi_S)\sum_{q\bar{q}}e_q^2\mathcal{I}\left[-\frac{\hat{P}_{h\perp}\cdot\vec{p}_T}{M}f_{1T}^{\perp q}(x,p_T^2)D_1^q(z,z^2k_T^2)\right]. \tag{2.69}$$

From the experimental point of view, one prefers to measure cross section asymmetries rather than to measure the absolute cross sections, since by measuring asymmetries many systematic uncertainties can be canceled. In particular, if one has a transversely polarized target, the asymmetries, defined Single Spin Asymmetries (SSA), are as follows:

$$A_{\text{Beam Target}} \equiv \frac{1}{|S_T|}\frac{d\sigma(\phi,\phi_S)-d\sigma(\phi,\phi_S+\pi)}{d\sigma(\phi,\phi_S)+d\sigma(\phi,\phi_S+\pi)}, \tag{2.70}$$

where the subscripts (Beam/Target) indicates the polarization of the beam and can be U=unpolarized, T= transversely polarized and L = longitudinally polarized. In order to extract the distribution and fragmentation functions, it is convenient to evaluate *azimuthal moments*, that are obtained from cross section asymmetries , as follows

$$\langle sin(n\phi+m\phi_S)\rangle^h_{\text{Beam Target}} \equiv \frac{\int d\phi_S d^2P_{h\perp}sin(n\phi+m\phi_S)d^6\sigma_{\text{Beam Target}}}{\int d\phi_S d^2P_{h\perp}d^6\sigma_{UU}}, \tag{2.71}$$

$$\langle cos(n\phi+m\phi_S)\rangle^h_{\text{Beam Target}} \equiv \frac{\int d\phi_S d^2P_{h\perp}cos(n\phi+m\phi_S)d^6\sigma_{\text{Beam Target}}}{\int d\phi_S d^2P_{h\perp}d^6\sigma_{UU}}, \tag{2.72}$$

where n and m are integers positive or negative, respectively, and h indicates the measured hadron. Indeed, in order to disentangle the polarized contribution from the total cross sections, one considers the differences between the cross sections corresponding to different polarizations of target and beam. In particular, let us consider the UT case. Since the unpolarized cross section, present in the decomposition of both (2.71) and (2.72), is given by

$$d^6\sigma_{UU} \equiv \frac{1}{2}(d^6\sigma_{U\uparrow}+d^6\sigma_{U\downarrow}) = \frac{1}{2}(d^6\sigma_{U\rightarrow}+d^6\sigma_{U\leftarrow}), \tag{2.73}$$

the azimuthal moments take exactly the structure of the above mentioned asymmetries (2.70). The so-called Collins ($n=1$, $m=1$) and Sivers ($n=1$, $m=-1$) moments, which are derived from the Eq. (2.68) and (2.69), respectively, are given by:

$$\langle sin(\phi+\phi_S)\rangle^h_{UT} = -|\vec{S}_T|\frac{\frac{1}{xy^2}B(y)\sum_{q\bar{q}}e_q^2\int d^2\vec{P}_{h\perp}\mathcal{I}\left[\frac{\vec{k}_T\cdot\hat{P}_{h\perp}}{M_h}\delta q(x,p_T^2)H_1^{\perp q}(z,z^2k_T^2)\right]}{2\frac{1}{xy^2}A(y)\sum_{q\bar{q}}e_q^2q(x)D_1^q(z)}, \tag{2.74}$$

$$\langle sin(\phi-\phi_S)\rangle^h_{UT} = -|\vec{S}_T|\frac{\frac{1}{xy^2}A(y)\sum_{q\bar{q}}e_q^2\int d^2\vec{P}_{h\perp}\mathcal{I}\left[\frac{\vec{p}_T\cdot\hat{P}_{h\perp}}{M}f_{1T}^{\perp q}(x,p_T^2)D_1^q(z,z^2k_T^2)\right]}{2\frac{1}{xy^2}\langle A(y)\rangle\sum_{q\bar{q}}e_q^2q(x)D_1^q(z)}, \tag{2.75}$$

The $A(y)$ and $\langle A(y)\rangle$ terms in (2.75) can not be simplified because the integrations of numerator and denominator are performed separately and related in general with different kinematical sets (and different kinds) of measures. The first asymmetry contains the product of the transversity distribution and the Collins fragmentation function (both T-odd and chiral-odd); the second, contains the product of Sivers function and the spin-independent fragmentation function. It should be pointed out that, after integrating over $P_{h\perp}$, these products, with a general form $f(p_\perp^2) \times g(k_\perp^2)$, are embedded in integrals over the transverse momenta of the initial and final quarks that do not factorize. As a matter of fact, this is due to the two weights, $\mathcal{W} = \frac{\vec{k}_T \cdot \hat{P}_{h\perp}}{M_h}$ for Collins and $\mathcal{W} = \frac{\vec{p}_T \cdot \hat{P}_{h\perp}}{M}$ for Sivers, with $\vec{P}_{h\perp} = z(\vec{k}_T - \vec{p}_T)$. Then, one has to make an analytic assumption on the transverse momentum dependence of the distribution and fragmentation functions. A simple, not realistic choice[4] is the so called *Gaussian ansatz*, that amounts to have a gaussian-like dependence upon $\vec{p}_T$ and $\vec{k}_T$, viz.

$$\delta q(x, p_T^2) \approx \frac{\delta q(x)}{\pi \left\langle p_T^2(x) \right\rangle} e^{-\frac{p_T^2}{\left\langle p_T^2(x) \right\rangle}}, \; H_{1T}^\perp(z, K_T^2) \approx \frac{H_{1T}^\perp(z)}{\pi \left\langle K_T^2(z) \right\rangle} e^{-\frac{K_T^2}{\left\langle K_T^2(x) \right\rangle}}, \tag{2.76}$$

where the relation $\vec{K}_T = -z\vec{k}_T$ is used and the mean values are given by

$$\left\langle p_T^2(x) \right\rangle = \frac{\int d^2\vec{p}_T p_T^2 q(x, p_T^2)}{q(x)}, \left\langle K_T^2(z) \right\rangle = \frac{\int d^2\vec{K}_T K_T^2 D_1(z, K_T^2)}{D_1(z)}. \tag{2.77}$$

By assuming Gaussian ansatz, distribution and fragmentation functions factorized and one obtains:

$$\langle sin(\phi + \phi_S) \rangle_{UT}^h = \frac{|\vec{S}_T|}{\sqrt{1 + z^2 \left\langle p_T^2 \right\rangle / \left\langle K_T^2 \right\rangle}} \frac{\frac{1}{xy^2} B(y) \sum_{q\bar{q}} e_q^2 \delta q(x) H_1^{\perp(1/2)q}(z)}{\frac{1}{xy^2} A(y) \sum_{q\bar{q}} e_q^2 q(x) D_1^q(z)}, \tag{2.78}$$

$$\langle sin(\phi - \phi_S) \rangle_{UT}^h = \frac{|\vec{S}_T|}{\sqrt{1 + \left\langle K_T^2 \right\rangle / (z^2 \left\langle p_T^2 \right\rangle)}} \frac{\frac{1}{xy^2} A(y) \sum_{q\bar{q}} e_q^2 f_{1T}^{\perp(1/2)q}(x) D_1^q(z)}{\frac{1}{xy^2} A(\bar{y}) \sum_{q\bar{q}} e_q^2 q(x) D_1^q(z)}. \tag{2.79}$$

A different choice, that avoids any assumption on the transverse momentum distributions, is made by constructing $P_{h\perp}$-weighted asymmetries in order to eliminate the cumbersome dependences in the weights. Then, Sivers and Collins moments reads:

$$\begin{aligned} \left\langle \frac{P_{h\perp}}{zM_h} sin(\phi + \phi_S) \right\rangle_{UT}^h &\equiv \frac{\int d\phi_S d^2\vec{P}_{h\perp} \frac{P_{h\perp}}{zM_h} sin(\phi + \phi_S) d^6\sigma_{UT}}{\int d\phi_S d^2\vec{P}_{h\perp} d^6\sigma_{UU}} \\ &= |\vec{S}_T| \frac{\frac{1}{xy^2} B(y) \sum_{q\bar{q}} e_q^2 \delta q(x) H_1^{\perp(1)q}(z)}{\frac{1}{xy^2} A(y) \sum_{q\bar{q}} e_q^2 q(x) D_1^q(z)} \end{aligned} \tag{2.80}$$

$$\begin{aligned} \left\langle \frac{P_{h\perp}}{zM_h} sin(\phi - \phi_S) \right\rangle_{UT}^h &\equiv \frac{\int d\phi_S d^2\vec{P}_{h\perp} \frac{P_{h\perp}}{zM_h} sin(\phi - \phi_S) d^6\sigma_{UT}}{\int d\phi_S d^2\vec{P}_{h\perp} d^6\sigma_{UU}} \\ &= -|\vec{S}_T| \frac{\frac{1}{xy^2} A(y) \sum_{q\bar{q}} e_q^2 f_{1T}^{\perp(1)q}(x) D_1^q(z)}{\frac{1}{xy^2} A(\bar{y}) \sum_{q\bar{q}} e_q^2 q(x) D_1^q(z)} \end{aligned} \tag{2.81}$$

For the extraction of the Sivers function, it is convenient to introduce the *purities*, defined as:

$$\mathcal{P}_q^h(x, z) \equiv \frac{e_q^2 q(x) D_1^{q \to h}(z)}{\sum_{q'\bar{q}'} e_{q'}^2 q'(x) D_1^{q' \to h}(z)}, \tag{2.82}$$

[4] What it is expected is that a Gauusian-like shape works in small transverse momentum regions, whereas for high transverse momenta a power low behavior is expected.

where $q(x)$ and $D_1(z)$ are the spin independent distribution and fragmentation functions extracted from the experiments, respectively. Then, the $P_{h\perp}$-weighted Sivers moment can be written as:

$$\left\langle \frac{P_{h\perp}}{zM_h} sin(\phi - \phi_S) \right\rangle_{UT}^{h} \equiv -|\vec{S}_T| \frac{\frac{1}{xy^2}A(y)}{\frac{1}{xy^2}A(\bar{y})} \sum_{q,\bar{q}} \mathcal{P}_q^h(x,z) \frac{f_{1T}^{\perp(1)q}(x)}{q(x)}, \tag{2.83}$$

where the ratio $f_{1T}^{\perp(1)q}(x)/q(x)$ is called *Sivers polarization*.
Recently, has been clearly shown for the case of the unpolarized TMD (see [36, 37, 38]) that the Gaussian hypothesis, adopted in order to simplify the analysis, is too strong and a more accurate functional form is needed. Furthermore, even assuming Gaussian distributions for the transverse momenta, a clear flavor dependence appears when a flavor-dependent Gaussian hypothesis is assumed. These two conditions lead immediately to the necessity of more accurate SIDIS data, and in particular concerning neutron, which becomes crucial in order to achieve a sound flavor decomposition of the TMDs and to fit more complicate functional forms.

2.3 Experimental and phenomenological overview

The first SIDIS experiments by using a transversely polarized target, aimed to measure Collins and Sivers asymmetries (preferred to cross sections for a better control of systematics) have been performed in the recent past by the HERMES, the COMPASS and the JLab Hall A collaborations. The first collaboration [39] exploited a polarized proton target, the second one used both polarized deuteron [40] and proton [41] targets and the third used polarized ^{3}He target as a neutron effective target [47]
The HERMES, COMPASS and JLab kinematic regions of investigation (Q^2_{HERMES} up to $\sim$ 10 GeV^2, $Q^2_{COMPASS}$ up to $\sim$100 GeV^2, Q^2_{JLab} up to $\sim$ 2.7 GeV^2)are quite different, even if they overlap in the x range. Therefore, a direct comparison of the three sets of experimental data requires a careful analysis: a consistent framework in which evolution equations of the TMDs are defined is needed in order to connect data at different Q^2. However, some general remarks can be put forward (see Fig. 2.8):

1. well established SIDIS measurements exist only for proton and deuteron targets.

2. the statistics for a kaon in the final hadronic state is limited. This kind of final state is useful for investigating the sea-quark distributions.

3. the results for the proton Collins asymmetries show that:

    - the asymmetries for the π^+ and the K^+ are positive and increasing with x (the K^+ result is about twice the π^+ one),
    - the asymmetry for the π^0, observed at HERMES, is compatible with a vanishing value,
    - the asymmetry is negative for the π^-,
    - the asymmetry for the K^- is compatible with a vanishing value,

4. the results for the proton Sivers asymmetries show that:
   - the asymmetry is clearly positive at HERMES for both π^+ and K^+ (the K^+ result is bigger than the π^+ one). It is increasing with z (that is the energy fraction of the final hadron) and at low $p_\perp$, pointing toward a plateau at high $p_\perp$. The latest results for the π^0 at COMPASS seem in agreement with the HERMES ones;
   - The K^- asymmetry seems to be slightly positive. Differently, the preliminary COMPASS result are compatible with a vanishing value.
5. the Collins and Sivers asymmetries on deuteron, observed by COMPASS, are compatible with a vanishing value for both π and K.
6. the Collins and Sivers asymmetries on ^{3}He (neutron), observed by Hall A, are compatible with a vanishing value for π (it can be seen one sigma effect at large x for Sivers), see Fig. 2.9.

From the most recent analysis of data taken at HERMES [42], the proton Collins and Sivers moments on a two-dimensional grid (with different binning on z and x) have been extracted, for the first time; in Fig.(2.8) the results for the Collins moments, corresponding to data from SIDIS with a final π^+ or π^- (upper row of each panel), are shown.

In parallel to the experimental efforts for gathering information on transversity, there has been the development of the phenomenological studies for extracting the relevant knowledge. It is worth noting that, in 2007 Anselmino and al. [43] have extracted the transversity and the Collins fragmentation function for the valence quarks u and d, by a global fit analysis of the HERMES proton data, the COMPASS deuteron data and also the BELLE e^+e^- data [43] at high Q^2 ∼110 GeV^2. In Fig.(2.10) the extracted transversities for the u and d quarks are shown. Some comments are in order:

- the transversity distributions of u and d quarks show the same general features of the helicity distributions (see e.g. ref. [18]): negative for the d quark and positive for the u quark;
- the distributions are smaller than model predictions. They are about half of the Soffer limit [44];
- the unfavored (see Eq. 2.50) Collins fragmentation functions is opposite in sign and larger than the favored one.

The same group has also extracted a new parametrization of the Sivers function, (see [45]), by fitting the HERMES and COMPASS proton and deuteron data, respectively. New fits have been recently obtained by adopting a Gaussian Ansatz for the $P_\perp$ dependence. In particular in Fig.(2.11) the x-dependence of the Sivers function is shown. It is possible to deduce that:

- the magnitude of the d and u distributions are very similar, but opposite in sign;
- the magnitude of the $\bar{s}$ quark distribution is no longer sizable;

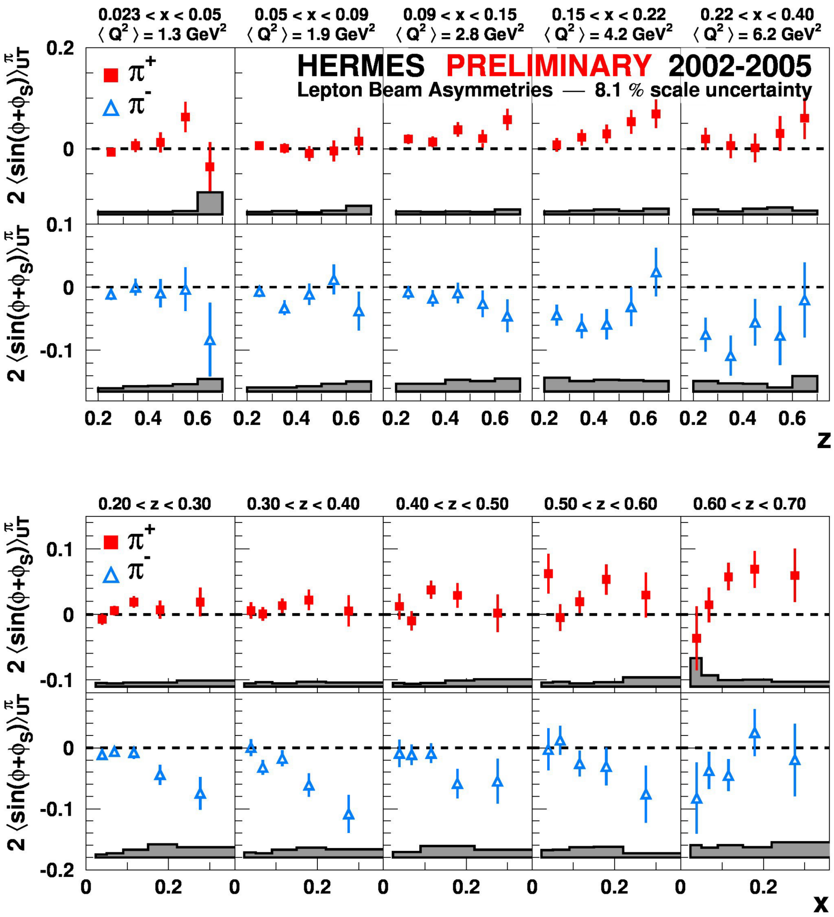

Figure 2.8: Proton Collins moments extracted (for the first and unique time) by HERMES and presented in [42], shown on a (x, z) grid.

- the overall sea quark distribution is relatively small.

The above SIDIS results are, for both transversity and Sivers functions, the first evidence of a non-zero chiral-odd parton distribution functions. Summarizing, both Sivers and Collins effects have been observed on proton, but unfortunately, the statistics do not allow an efficient multidimensional representation (x,z,$P_\perp$) of the data. Differently, the same asymmetries is compatible with zero for a deuteron target. It is important to point out that no data exist for x > 0.3, region where all the measured non-zero asymmetries are expected to be sizable. This makes difficult or even prevents the extraction of information on the neutron (namely the flavor decomposition of the TMD's is hindered), but future experimental activity at the intensity frontiers are planned at JLab, that aims at obtaining a high precision measurements also for the neutron DFs. In particular, in what follows, one of the main issues related to the possibility to get reliable data on the neutron will be addressed. To be more explicit, since neutron target does not exists one has to resort to nucler targets. Among them, a polarized ^{3}He is very effective, but one has to take care of the nuclear

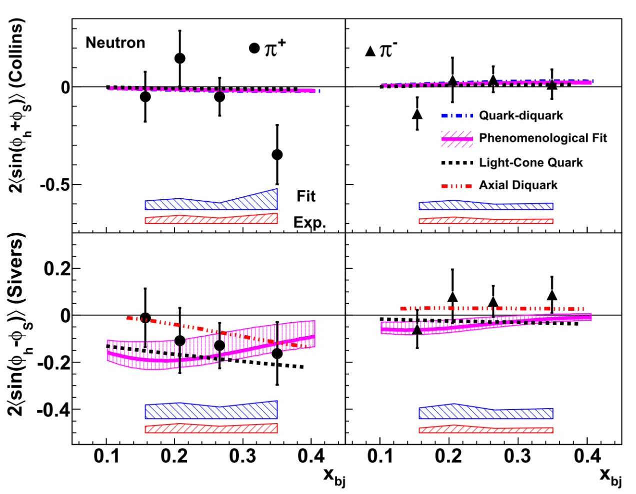

Figure 2.9: (Color online) The extracted neutron Collins and Sivers moments with uncertainty bands for both π^+ and π^- electro-production. (From [47])

effects in both initial and final states, involved in the extraction of the neutron DF and evaluate the effective weight of this systematic error in the context of an high luminosity experiment.

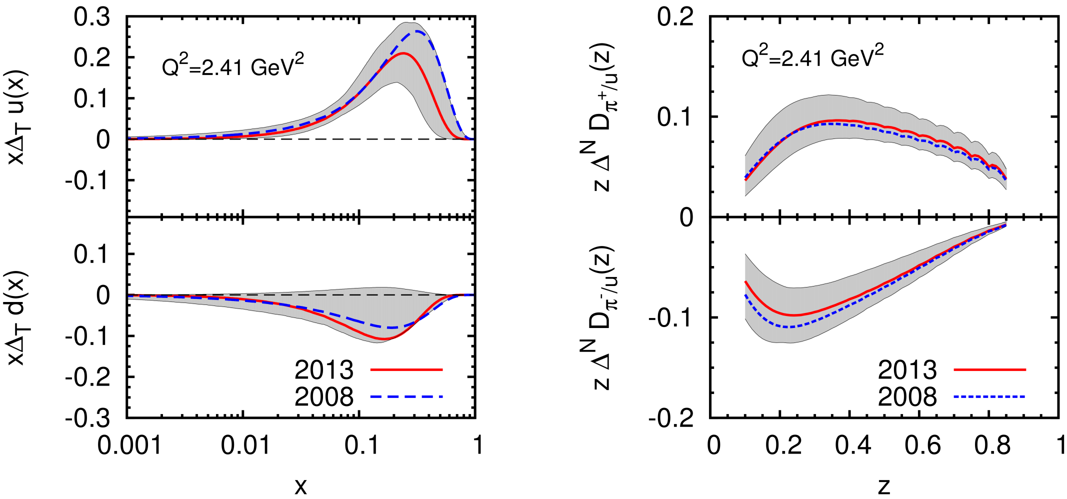

Figure 2.10: Left panel: the transversity distribution functions ($\Delta_T \equiv \delta$ in our notation) for u and d flavours as determined by the global fit (gray band); it is also show the Soffer bound (blue lines) and the (light gray) bands of Anselmino at al. previous extraction. Right panel: favoured and unfavoured Collins fragmentation functions ($\Delta^N D \equiv H_1^{\perp}$) as determined by the global fit (gray band); it is also show the positivity bound and the (light gray) bands as obtained in the previous extraction (After from [43])

.

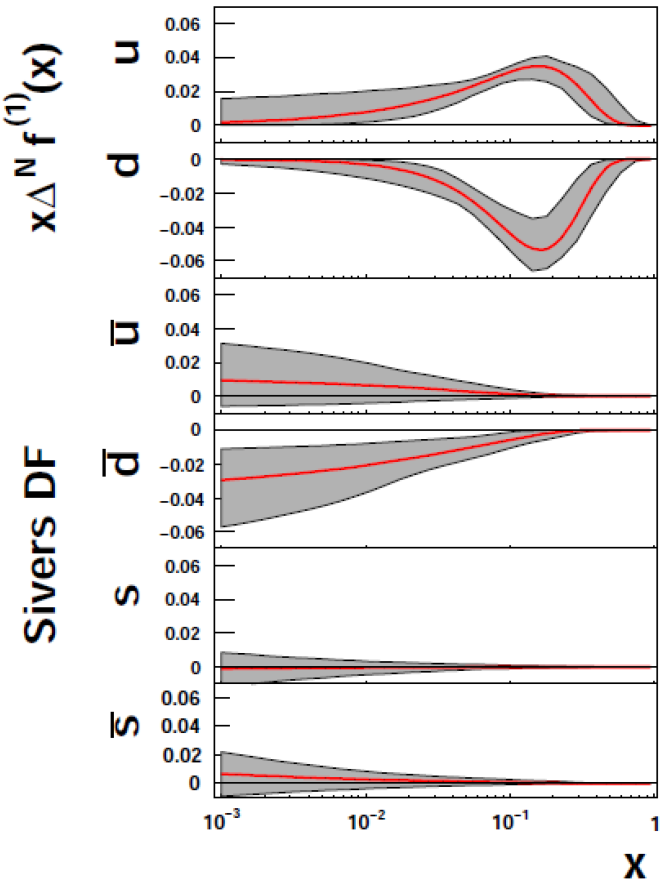

Figure 2.11: The Sivers functions ($\Delta^N f$ stands for $f_{1T}^{\perp}$ in our notation) for all 6 quark flavors, extracted from the HERMES and COMPASS data through a global fit by Anselmino at al. (After Ref. [46]). The gray bands are the uncertainties.

Chapter 3

Hall A planned transversity experiments

A SIDIS experiment requires a lepton beam that collides off an hadronic target (or beam) and the detection of the scattered lepton and of an hadron in coincidence. In addition, an extensive study of the transverse degree of freedom of the partons requires a polarized target and/or polarized beam. Finally, the relative weakness of the electromagnetic interaction demands for high intensity beam and target density and or large area detectors.
The Thomas Jefferson National Accelerator Facility (JLab) represents, trough the technological upgrade of the Continuous Electron Beam Accelerator Facility (CEBAF) at 12 GeV, one of the most important laboratory in which a SIDIS scientific program can be performed successfully, in the coming years. After the 12 GeV upgrade JLab will host four experimental halls (Hall A, Hall B, Hall C and new Hall D dedicated to the real photon physics). Hall A and the Hall C can exploit the full intensity of the electron beam. Furthermore, Hall A, the largest experimental Hall, allows the maximum flexibility for the optimal configuration of large experimental equipment.
The JLab Halls will be extensively devoted to the study of the nucleon structure and the hadron spectroscopy, parity violation experiment for precise QED test, search of dark matter (and more). The Hall B will be equipped with the new CLAS12 detector: a "4π" toroid detector that will benefit in few years of an extended hadron identification provided by a challenging RICH. A forward tagger will complement the CLAS12 for quasi real photons physics. The physical goals of Hall B are both nucleon structure (with a wide range of SIDIS measurements approved, in order to study proton TMDs) and hadron spectroscopy. Hall C is able to tolerate a 10^{38} $s^{-1}cm^{-2}$ luminosity, it is equipped with two small acceptance spectrometers providing precise event reconstruction: this will make possible precise measurements of production cross sections. The new Hall D, which uses a real photons beam derived from the 12 GeV electron beam, is devoted to hadron spectroscopy and search of exotic states. Hall A, which will be the topic of the following Sections, will be equipped with two spectrometers (one for the hadrons detections and one for the electrons) and after 2017 this configuration will be replaced by the SoLID, a "4π" detector. The physics program of Hall A on nucleon structure, concern mainly polarized SIDIS (3He and NH3 polarized targets)

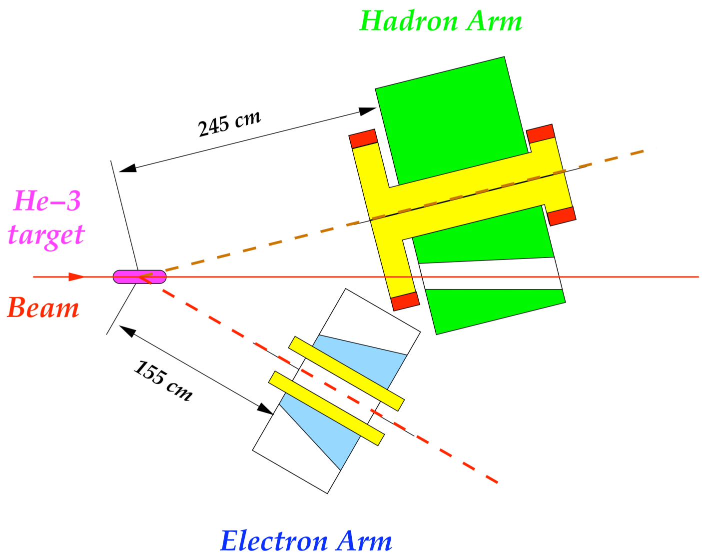

Figure 3.1: Schematic of SIDIS two-arm setup

experiments as well as extented measurements of the nucleon form factors. In the following we will focus on the experimental setup of the first SIDIS experiment on neutron that will likely be performed in Hall A in the coming years.

3.1 SIDIS experiments in Hall A

The first new high luminosity experiment on the neutron spin structure will likely be the approved E12-09-018 experiment (SIDIS for short) on transversely polarized neutron, the electron beam will scatter through a 60 cm long polarized ^{3}He target. The scattered electrons and the produced hadrons (pions or kaons) will be detected in the electromagnetic spectrometer (called BigBite) and in the new hadronic spectrometer (called SuperBigBite), respectively, as shown in Fig. 3.1.

The new important features of this experiment is the high luminosity: the projected luminosity corresponds to approximately $4 \cdot 10^{36}$electron-polarized neutron cm^{-2}/s (several times higher than any previous polarized SIDIS experiment). Hence the need of an experimental apparatus that operates correctly at the expected luminosity. The most critical elements in this sense, are the target, the Ring Imaging Cherenkov detector and the Gas Electron Multiplier (GEM) tracker in both spectrometers. For what concerns the target, operation on high intensity beam and fast polarization exchange (at the level of minutes) are the most challenging characteristics. A method was developed to reduce this time to 120 seconds (10 times shorter than before).

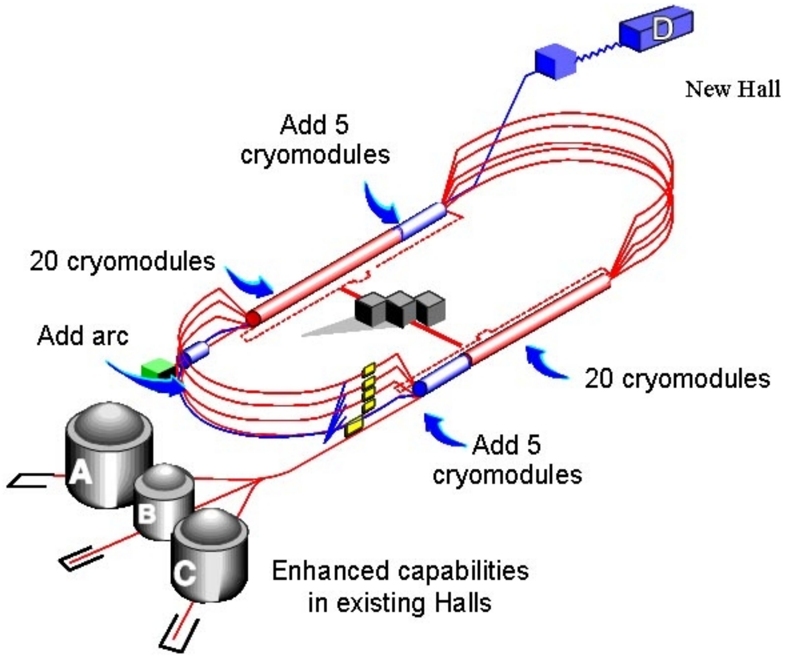

Figure 3.2: Schematic view of CEBAF accelerator and experimental Halls at JLab after the 12 GeV upgrade.

3.2 The CEBAF beam

The CEBAF electron accelerator (see Fig. 3.2) consists of one injector, two super-conducting linear accelerators (LINAC), and two recirculation arcs[5]. Electrons are accelerated through the LINACs and circulated up to five times (six for the Hall D). The photocathode gun system is used to deliver the continuous-wave (CW) beams of high polarization and high current to Hall A and C and low current to Hall B. The current of the beam may exceed 200 μA with a grade of longitudinal polarization of 85%, level obtained by shining the circularly polarized laser light on a strained gallium arsenide (GaAs) cathode. Then, the electrons are injected into the accelerator after initial acceleration to 45 MeV. Each LINAC can further accelerate the electron by up to about 1 GeV, through radio frequency (RF), superconducting cavities. At the end of the recirculation process, the maximum beam energy deliverable to the Halls is about 11 GeV (12 GeV for the Hall D).
The beam polarization is measured and monitored by Moller [48] and Compton [49] polarimeters (whose operating principles are based on the polarized Moller and Compton scattering, respectively). The spectrometers data are also used to monitor the correct operation of the whole apparatus, by means of specific well known physics processes. For instance, the counting rate in a well positioned counter, as observed in the GEn1 experiment [50], has significant helicity dependence due to the single spin asymmetry in $\vec{\gamma}\vec{n} \to \pi X$ process. Therefore, any change in the single spin asymmetry could establish a change in the target or beam polarization.

[5]Each arc consists of 5 staggered lines of bending magnets.

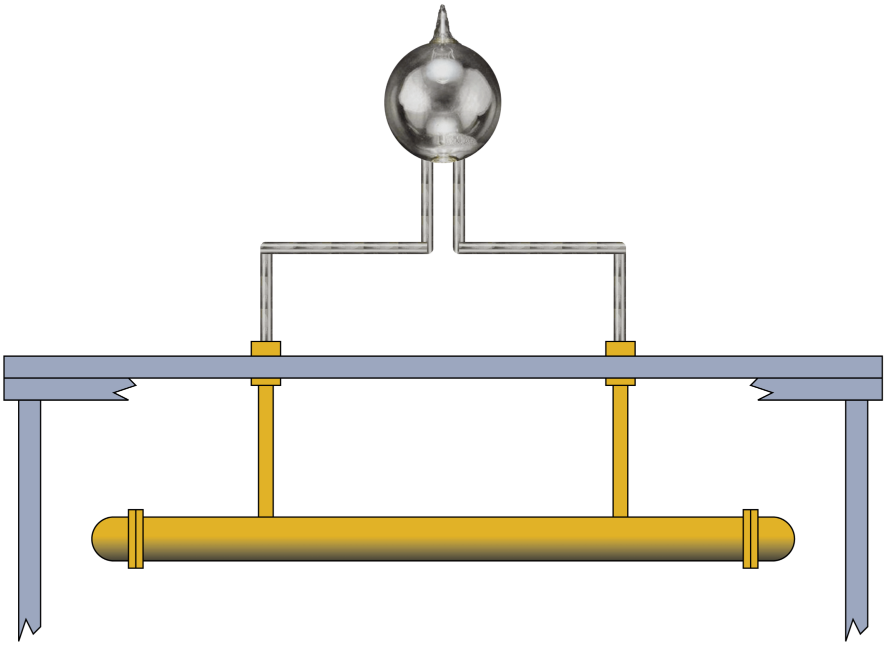

Figure 3.3: A straw-man sketch of the SIDIS target cell. Two transfers tubes connect the pumping cell to the target chamber to make it possible to drive convection between the two chambers. Also, the upper portion of the cell is made of glass, whereas the lower portion is made of metal, likely gold-plated copper. The two sections are connected to one another using a system that captures a gasket made of indium, and the metal portion of the setup is contained in an evacuated scattering chamber.

3.3 Polarized ^{3}He target

Pure neutron fixed target does not exist; a gaseous ^{3}He target is used as effective polarized neutron target. In fact the ground state wavefunction of the ^{3}He consists of the superposition of the S (88.2%), S' (1.4%) and D (9.8%) states; in the dominant S state the spins of the two protons do cancel out (see following Chapters for a detailed phenomenological description of ^{3}He).
60 cm long sealed glass cell containing ^{3}He gas with a density of $1.3 \times 10^{-4} g/cm^2$. The helium nuclei are polarized by means of the combination of the optical pumping and spin exchange techniques.
The target 3D drawing is shown in Fig. 3.3. The upper chamber, called *pumping chamber* (here the temperature is of order 270^o), is the part where spin-exchange optical pumping take place. The lower chamber, called *target chamber* (here the temperature is about 70^o), is the region trough which the electron passes. The *transfer tube* connects the two parts. In the original version, the ^{3}He passes from the pumping chamber to the target cell by means of the *diffusion* trough a single transfer tube; diffusion is relatively slow and require a short transfer tube; it therefore severely limits the maximum achievable luminosity to about 10^{36} cm^{-2}/s. In the new SIDIS experiment a new design of the target, with 2 transfer tubes will permit the ^{3}He exchange by convection, which is faster.

3.3.1 Operating principles and performances

The spin-exchange optical pumping polarization, can be schematically divided in three main steps (see Fig.3.4):

- a circularly polarized light (from high power laser) polarize the valence electrons of Rubidium (Rb) alkali atoms; the polarized light basically flips the Rb valence electrons with a defined spin direction by excitation and subsequent de-excitation of the valence electrons. The de-excitation is followed by the emission of photons that are absorbed by a small quantity of nitrogen, to avoid de-polarization of the Rb.
- the polarized Rb atoms transfer the polarization to Potassium (K) via atomic collisions.
- the polarized K atoms transfers the polarization to the ^{3}He through hyperfine like interactions; direct transfer of Rb to ^{3}He is inefficient.

Once the ^{3}He is polarized, it must be transferred to the scattering cell; the current technology is based on diffusion along a short transfer tube. The challenging convection-driven transfer, which is currently under testing, offers a number of advantages:

- The beam induced depolarization of the ^{3}He nuclei is drastically reduced by a faster exchange of the polarized nuclei.
- The distance between the region in which the ^{3}He is polarized from the region in which the ^{3}He serves as a target (pumping and target cells distance) can be increased.
- The previous point provides flexibility in the manner in which the holding magnetic fields are generated: in fact, a longer pumping-target cells distance permits to control the magnetic field at the target chamber independently from the magnetic field in the pumping chamber. Therefore, the two fields can point in different direction. The gas will take about 120 s to travel from the pumping chamber down to the target chamber and back into the pumping chamber. This is more than enough for the spins to adiabatically follow the magnetic field through an arbitrary change in direction with negligible loss in polarization. The magnetic field of the target can be flip in about 10 s (this time is the sum of the time for the field flip and the time for the polarization stabilization) and then is plan that the target direction will be flipped one every two minutes with a loss of data taking less than 10%.

The expected polarization performance with a beam current of 60μA and a target chamber length of 60 cm, is about 62%.

3.4 The electron Spectrometer BigBite

The BigBite spectrometer, shown in Fig. 3.5 will be used to detect the scattered electrons in coincidence with the produced hadrons. It will be placed (fixed) at 30°(on the opposite side of the beam respect to the SBS hadron spectrometer) and at a distance from the target of 155 cm due to

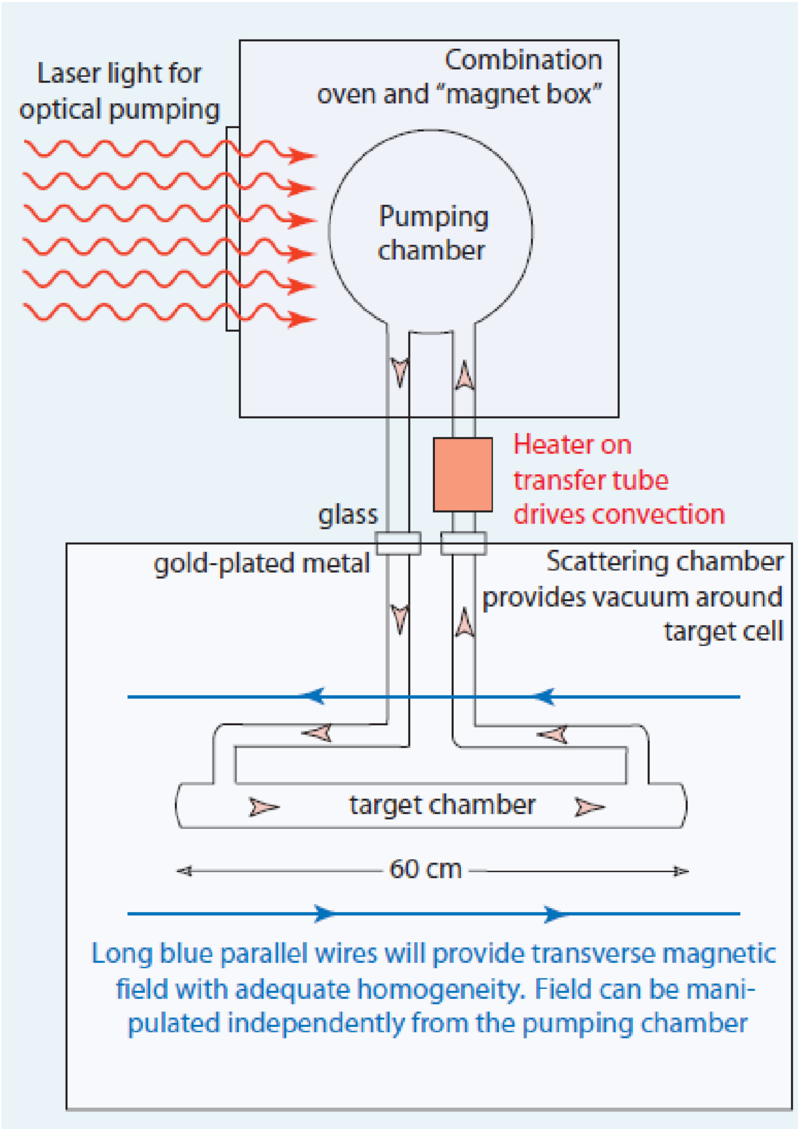

Figure 3.4: Targer operating principles.

the geometry constraints. The components of the electron spectrometer are a large dipole magnet which produces a field of about 1.2 T (with a current of 710 A), a GEM tracker (same design of the SBS, as discussed later), a Cherenkov detector, a two layer electromagnetic calorimeter and a scintillator hodoscope. For a 60 cm long target, the average value of the solid angle is about 45 msr. The momentum coverage is 0.6-2.5 GeV.

3.5 The hadron spectrometer Super Bigbite (SBS)

The SBS (Fig.3.6) consists of a dipole magnet, a high resolution tracker based on Gas Electron Multiplier (GEM) and small silicon microstrip detectors, a Ring Imaging Cherenkov detector and

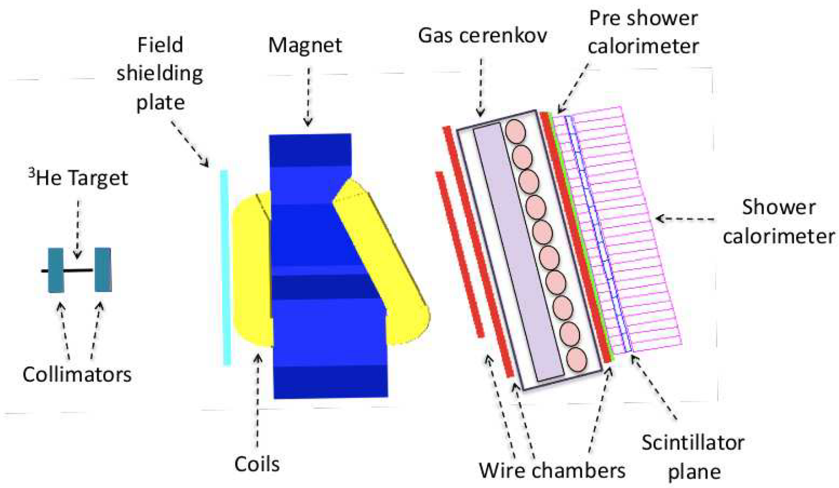

Figure 3.5: Layout of the current BigBite spectrometer; the wire drift chamber will be replaced by GEM modules in the SIDIS experiment.

SBS parameter	Symbol	Unit	Value
Distance from the target to the detector		(cm)	417
Central angle	θ_c	(degree)	14
Horizontal angular range	$\Delta\theta_h$	(degree)	± 3.6
Vertical angular range	$\Delta\theta_v$	(degree)	± 12
Momentum resolution	δ_p/p	(%)	$0.03p + 0.29$
Horizontal angular resolution	σ_{θ_h}	(mrad)	$0.09 + 0.59/p$
Vertical angular resolution	σ_{θ_v}	(mrad)	$0.14 + 1.34/p$
Vertex resolution (along beam)	σ_y	(mm)	$(0.53 + 4.49/p)/\sin\theta_c$

Table 3.1: The parameters of SBS in the SIDIS experiment.

a segmented calorimeter which will have the function of trigger and of electron rejection. An additional wide GEM chamber will possibly be placed behind the RICH mirror, just in front of the calorimeter to help in the localization of the shower in the calorimeter.

In Table 3.1 are reported the parameters of SBS for the approved SIDIS experiment [58]. To permit a forward position, the beam line must go through a hole in the dipole yoke. The residual field in the beam pipe shall be minimized.

Fig.3.7 represents the beam line configuration through the dipole magnet and the resulting magnetic field in the beam line. The magnet[6] will be placed at the distance of 245 cm from the target to the return yoke. The corresponding solid angle varies from 42 to 53 msr depending on the target position. At 16° central angle of SBS the 60 cm target will be seen with full solid angle.

The vertex resolution of about 6 mm and the expected momentum resolution of 0.5 % (at $p = 4$ GeV/c), should allow a good suppression of background from the end-cap window of the target cell and also suppression of accidental events by using the correlation between the vertexes

[6] A 48D48 dipole magnet designed and build by the Brookhaven National Laboratory.

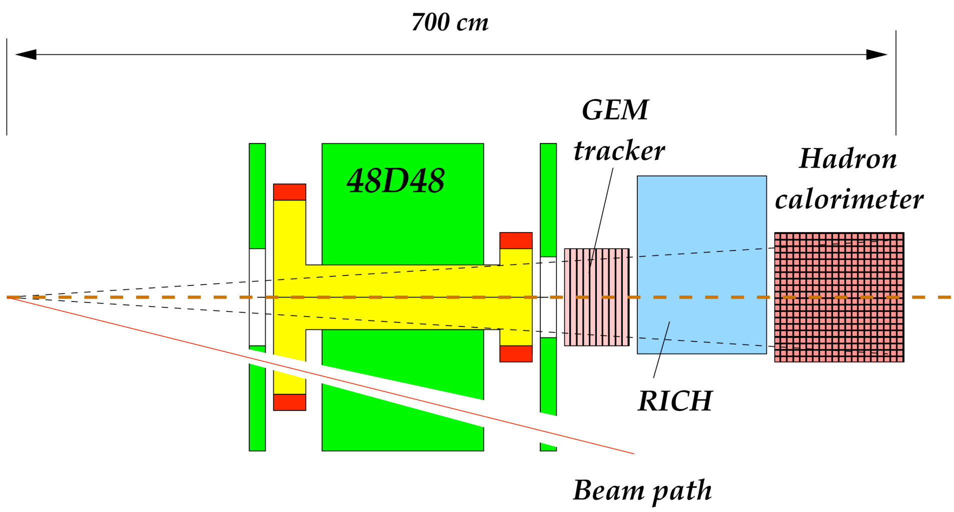

Figure 3.6: The schematic view of the SBS with the detector for the SIDIS experiment.

reconstructed in the electron and in the hadron arms.

3.5.1 RICH detector and calorimeters

In the following we quickly summarized the characteristics and the uses of the other detectors present in the SBS spectrometer.

The population of the kaons, for the proposed experiment, is expected to be about one order of magnitude less then the pion population, but of the same order of the proton population. From this, a very efficient system for hadron identification is necessary (also to permit a flavor decomposition of the SIDIS data). The concept and the design of the RICH as well as most of its components come from the dual radiator RICH of the HERMES experiment [52].

Figs. 3.8 and 3.9 show respectively the components of the HERMES RICH detector and a schematic figure of its working principle:

- photons are produced in 5.65 cm thick aerogel wall (the refraction index is 1.03 and the resulting weight is ≈ 0.8 g/cm^2) from over threshold charge hadrons at the entrance of the detector. The electron Cherenkov threshold energy in this aerogel is 2.1 MeV. Moreover photons are also produced by the gas between the aerogel and the mirrors, by more energetic particles (see Fig. 3.10)

- the generated photons are focused by an array of mirrors on a matrix of 3/4" diameter PMTs which is located in the focal surface of the mirror

- the signals from PMTs have characteristic rise time of about 2 ns and duration of the order of 4 ns. It will be amplified, discriminated and read out by LeCroy 1877 Fastbus TDCs with 0.5 ns count resolution. Then, in the offline analysis, the correlation between the RICH and hadron calorimeter timing signals (with a tolerance of about 5 ns) will be used to achieve signal to noise ratio for the photon rings reconstruction.

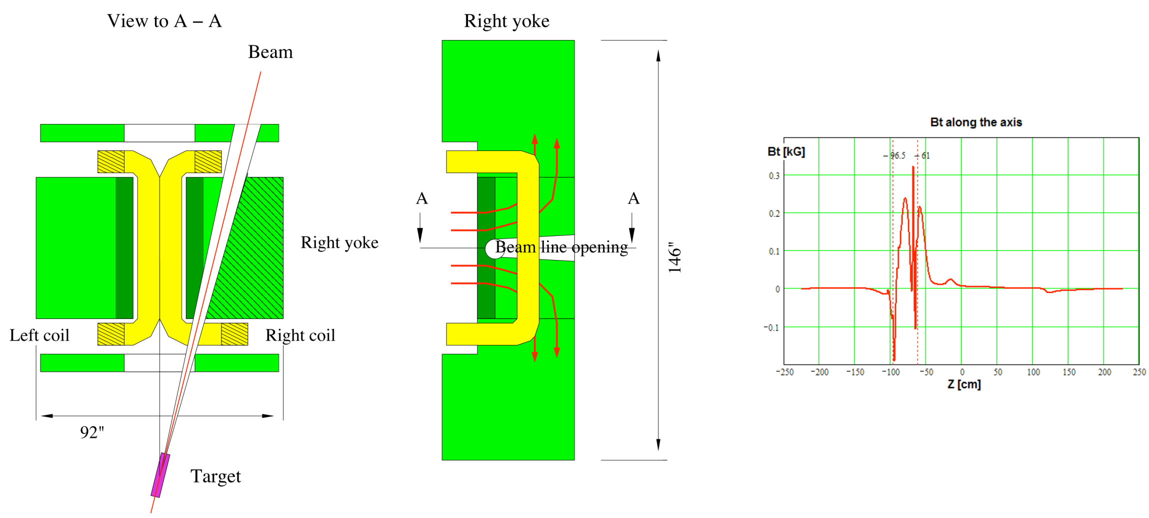

Figure 3.7: The beam path through 48D48 dipole.

Fig.3.8 shows a pictorial view of the HERMES RICH detector.

The HERMES RICH has an acceptance windows of 187×46 cm^2 which fits quite well to the acceptance of SBS. The very good stability of the HERMES RICH during the period of operation (from 1997 to 2007) is demonstrated in [53].

Although the nominal luminosity of the proposed experiment is orders of magnitude larger compared to the HERMES experiment the expected background in the RICH seems to be manageable. In fact the SBS magnet shields the RICH detector from low energy charged particles originating in the target, and therefore the main source of background are low energy photons that can reach the RICH and produce secondary electrons by Compton scattering and pair production (especially in the aerogel); those electrons can generate Cherenkov light in the aerogel and in the glas windows of the PMTs. A detailed Monte Carlo simulations has shown an average PMT occupancy (with a time resolution of 10 ns) of about 0.14 (without specific shielding), due mainly to radiating electrons in the aerogel and to a lesser extend ($\sim 1/4$) in the PMT glass window

The SBS hadron calorimeter measures the particle energy and provide a fast signal for online triggering. It is made of a modular structure with 242 blocks arranged in a matrix 11×12, at about 650 cm from the target. A single module consists of interleaved layers of 40 iron and scintillator plates. The thickness of the scintillator and iron plates is 5 mm and 20 mm, respectively. The cross sectional area of the plates is 142×146 mm^2. For the collection of the scintillation lights a wave length shifter is used (from 420 nm to 520 nm). The total length of a calorimeter module is 1450 mm. All the above mentioned components are enclosed in a rectangular container made of 1.4 mm thick steel sheets.

The main characteristics required for the scintillating plates are a high light yield and a uniform light collection over the scintillator surface. High radiation tolerance is also required.

With this setup, the expected spatial resolution is better than 5 cm, energy resolution at the

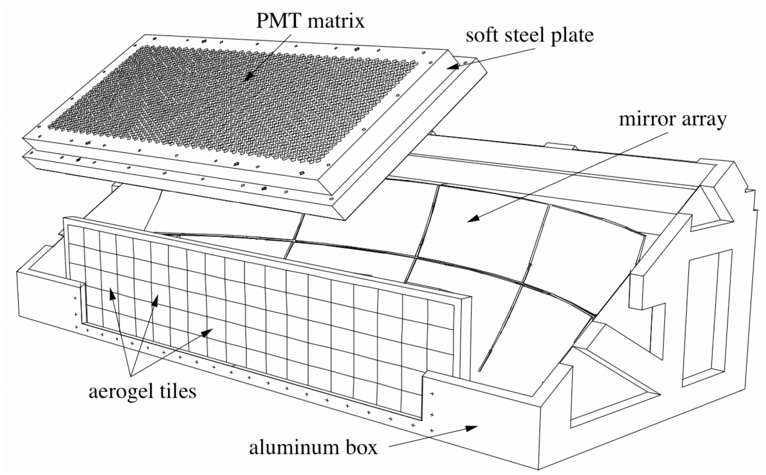

Figure 3.8: A pictorial view of the HERMES RICH.

level of 5-10% and formation of the output signal compatible to the designed 50 ns gate width.

3.6 Tracking detector: GEM chambers

The GEM (invented by Fabio Sauli in 1996 [51]) is a charge amplifier in gas-filled volumes. The active element of GEM consists of a thin composite mesh: a insulating polymer foil (e.g. kapton) whose both sides are metalized, with a holes pattern as shown in Fig. 3.11, generally obtained by consolidated photo-lithographic procedure. The GEM is a specific type of Micro Pattern Gaseous Detector.

The typical GEM is made of 50 μm thick kapton foil clad on both sides with 5 μm copper. The hole diameter in the copper is 75 μm and the distance between any two neighbor hole centers is 140 μm (see Fig. 3.12).

The simplest GEM chamber consists of a stack made of a drift foil, a drift cathode (or gap), a GEM foil, acting as an amplifier, followed by an induction gap and a readout foil. The gaps are filled by a suitable gas (depending on application) and permeated by an electrostatic fields obtained powering at high voltage the drift foil and the two sides of the GEM foil.

A ionizing particle traveling the drift gap produces primary ionizing electrons, that move toward the GEM holes due to the electrostatic field in the gap. The voltage difference between the two sides of the GEM foils generate a strong electric field inside the holes[7]. Therefore, the electrons that are in the negative side are attracted toward the holes and are accelerated (the same occurs for the positive ions in the opposite direction) to an energy that is able to generate additional secondary electrons (like in a proportional chamber). At the exit of the GEM hole a single electron may have generate typically about 20 secondaries. These electrons are collected by the readout foil which face the exit side of the GEM foil.

[7]A difference of 200 V generates a field along the axis of the hole that reaches 40 kV cm^{-1}.

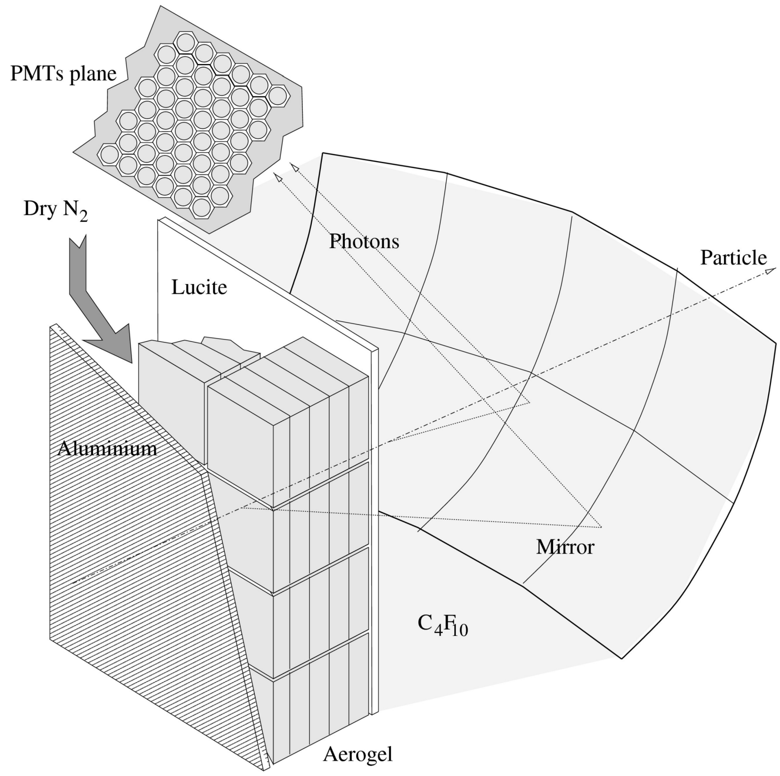

Figure 3.9: The working principle of the HERMES RICH.

It is worth nothing that the primary ionization, the charge amplification and the charge collection (readout) happen in different parts of a GEM chamber, and to a large extent can be considered independent.
Fig. 3.13 shows the typical field line in the GEM hole.

One peculiarity of the GEM technology is the possibility to increase the gain stacking several consecutive GEM foils, keeping the High voltage relatively low. Essentially, a GEM foil act as a preamplifier for the next GEM. Such a detector consists of a drift region, several multiplier layers (one for GEM) and finally the readout plane (see Fig. 3.14). Among the primary ionization charge produced by the ionizing particles that traverse the gas volume, only the charge produced in the first gap contribute significantly to the signal. Indeed, the charge produced for the first time in the subsequent steps is affected by missing at last of one multiplication step.
The field E_D, present in the drift gap, forces the electrons produced by ionization to pass into the first GEM foil holes where the potential difference ΔU_{GEM1} between the two sides of the GEM foils induces the multiplication. The amplification is iterate in the subsequent GEM foils. After the last GEM foil there is the collection gap, where the electrons are drifted by a collection field E_T to a readout plane.
Studies on the GEM gain performances showed that the gain increases with the decreasing of holes diameter, up to a plateau of about 70μm. The gain of the multi-GEM detector increases with the

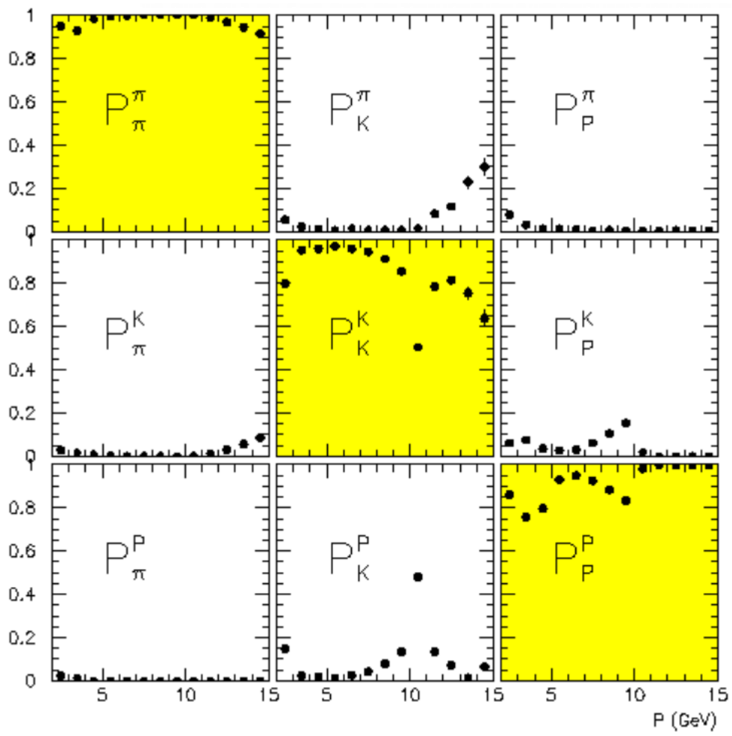

Figure 3.10: The performances of HERMES RICH. Along the diagonal there are the probabilities of identification of pions, kaons and protons respectively as a function of the momentum, off diagonal are probabilities of misidentified a particle. (After [53])

collection field, until avalanche multiplication occurs in the collection gap. Concomitantly with the optimal performance (that is with higher voltage difference) increases also the probability of discharges into the gaps, therefore a compromise configuration must be chosen. Also the electric transparency of the GEM depends on the drift field and on the difference of voltage across the GEM. Typical values of $\Delta U_{GEM} \sim 400$ V and drift fields (in the 3 mm pre-amplification region Fig. 3.14) of $2 \div 3$ kV/cm are used in standard GEM geometry. The resulting transparency is of the order of 90%.

In the triple-GEM geometry (the case of the detector in SBS and BB, see Fig. 3.14) the total gain is the product of the individual gains except for minor charge loses. As mentioned above, a possible inconvenient of the GEM (and of gaseous detector in general) is the occurrence of discharge at high voltage. In most cases in which discharge happens it remains localized in one foil and in this case the readout is only partially involved. However, also discharge that propagates in all planes can happen and, in this second case, the readout can be severely damaged. The amount of charge transfered to the readout in case of discharge depends on the capacitance of the foils. To reduce the risk of damage, the GEM voltage distribution is segmented on the more negative side; typical segment has an area of 100 cm^2. Obviously, in the case of multi-GEM detectors the probability of discharge is maximum at last multiplication step, where the avalanche is the biggest.

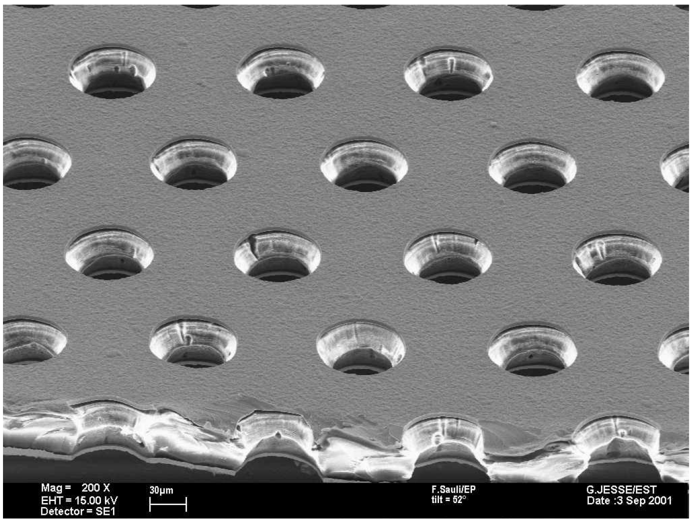

Figure 3.11: Picture of a GEM foil taken with an electron microscope.

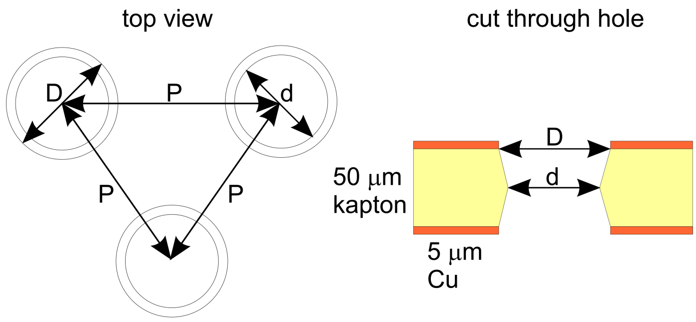

Figure 3.12: The parameters of the GEM foil, $D = 75\mu m$ and $P = 150\mu m$.

3.6.1 GEM trackers in SBS and BigBite

The triple GEM detector is expected to satisfy the requirements of the hadronic and leptonic trackers in the spectrometers for the proposed SIDIS experiment. The BB tracker will be made by 4 large 40×150 cm^2 GEM chambers and a small microstrip silicon detector. The SBS tracker will consists of 3 large 50×200 cm^2 GEM chambers.

Both GEM chambers are made by smaller identical GEM modules $40{\times}50$ cm^2 or $50{\times}50$ cm^2 properly combined as shown in Fig. 3.15 for the BB case.

To extend the tracking lever arm and also suppress the combinatorial background due to the large occupancy, two small planes of silicon detector in the SBS will consist of two planes (x and y) of about $10{\times}20$ cm^2 and each plane will be made of two identical tiles of $10{\times}10$ cm^2 area. Each plane will consist of microstrip with 50 μm pitch. The two planes will provide a track point right before the SBS magnet and therefore extending significantly the whole tracker arm in order

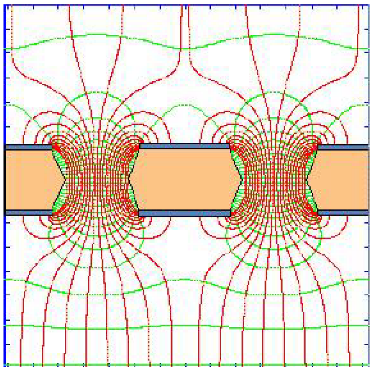

Figure 3.13: Electric field in GEM hole.

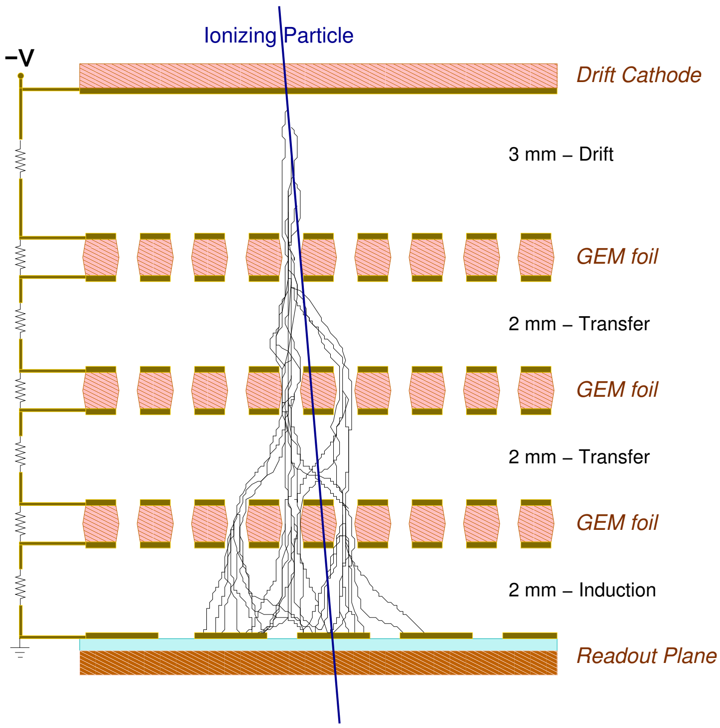

Figure 3.14: Schematic view of the three-GEM detector with the working principle (top)

to improve track reconstruction.

3.6.1.1 GEM electronics

An essential part of the GEM detector, due to its very high segmentation (number of active channels), is certainly the readout electronics. This is based on the analog APV25 chip developed by the Imperial College for CMS silicon detectors [56] and firstly used in a GEM detector by COMPASS. The APV25 is designed to be radiation tolerant (at lead up to 10 MRad); it has an high channel density (128 channels/chip) and a rather fast readout (up to 40 Mhz). Each APV25

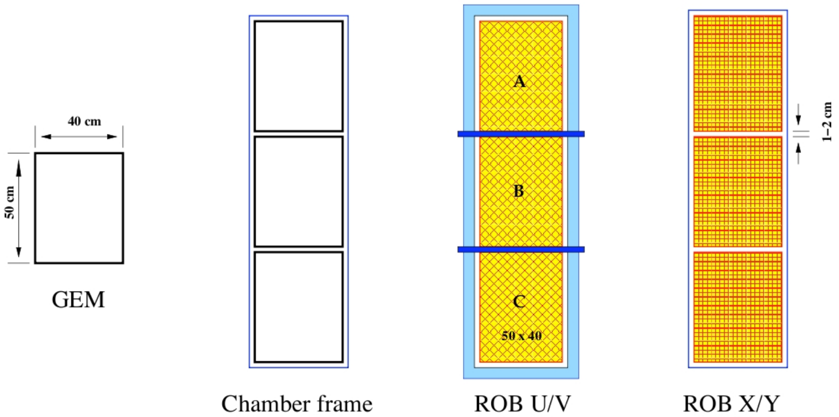

Figure 3.15: Schematic view of a single whole GEM chamber in SBS made of 3 adijacent GEM 40×50 GEM modules.

channel consists of a preamplifier followed by a shaper and a 192 cell analog pipeline, where the shaped signal (charge on the strip) is continuously sampled at 20 or 40 MHz (user selectable). The samples awaiting readout are flagged by external triggers, with adjustable latency. Multiple samples (up to 3) per channel and event will be converted and acquired by the GEM electronics. Apart from potential rate issues, the acquired information permits a simple signal analysis which provide: time information (with resolution at the level of 5 ns, though 3 ns has been measured) and charge information. The correlation of such information in the x and y plane shall permit a quite larger suppresione of the background and ghost hits.

3.7 Phase space simulation in the SIDIS experiment

The central scattering angles of the spectrometers (14 and 30 degree for SBS and BB respectively) are chosen to be as forward as possible compatible with the obstruction of the spectrometers and the fact of having the direction of the scattered hadron around the direction of the exchanged photon. The range of momenta of the scattered particles are basically determined by the spectrometer characteristics and cannot be changed.

The energies of the beam have been chosen at 8.8 and 11 GeV; the latter is the maximum achievable beam energy at CEBAF after the 12 GeV upgrade, while the former is the best compromise (in terms of phase space overlapping and yields) between the existing course data (at 5.7 GeV) and the upper value. These tree values permit an investigation of the asymmetries at different Q^2 that may reveal some QCD evolution effects.

The results for the central kinematics of five x bins, at the two different beam energies of 8.8 and 11 GeV, are showed in Tab. 3.2 and 3.3, respectively. The cumulated (Q^2, x) coverage of the two kinematics at $E = 8.8$ GeV and $E = 11$ GeV is also shown in Fig. 3.16.

Table 3.2: Kinematics at E=8.8 GeV for positive pions for different x bins. The central value and the approximate range is also shown.

x	E' GeV	P_π GeV	Q^2 GeV^2	z	$P_\perp$ GeV
0.20 ± 0.05	1.25 ± 0.16	3.40 ± 1.09	2.93 ± 0.34	0.45 ± 0.25	0.61 ± 0.24
0.30 ± 0.05	1.65 ± 0.21	3.19 ± 1.02	4.01 ± 0.33	0.45 ± 0.25	0.49 ± 0.21
0.40 ± 0.05	2.07 ± 0.23	3.02 ± 0.97	5.03 ± 0.32	0.45 ± 0.25	0.37 ± 0.18
0.50 ± 0.05	2.44 ± 0.26	2.77 ± 0.88	5.95 ± 0.33	0.44 ± 0.24	0.28 ± 0.14
0.60 ± 0.05	2.65 ± 0.22	2.53 ± 0.79	6.70 ± 0.33	0.41 ± 0.24	0.23 ± 0.13

Table 3.3: Kinematics at E=11 GeV for positive pions for different x bins. The central value and the approximate range is also shown.

x	E' GeV	P_π GeV	Q^2 GeV^2	z	$P_\perp$ GeV
0.20 ± 0.05	1.32 ± 0.15	4.29 ± 1.37	3.82 ± 0.43	0.44 ± 0.25	0.82 ± 0.30
0.30 ± 0.05	1.72 ± 0.23	4.11 ± 1.32	5.20 ± 0.44	0.44 ± 0.25	0.69 ± 0.27
0.40 ± 0.05	2.17 ± 0.26	3.89 ± 1.24	6.60 ± 0.42	0.44 ± 0.25	0.56 ± 0.24
0.50 ± 0.05	2.58 ± 0.28	3.71 ± 1.17	7.86 ± 0.42	0.44 ± 0.25	0.45 ± 0.20
0.60 ± 0.05	2.97 ± 0.30	3.40 ± 1.08	9.02 ± 0.44	0.42 ± 0.24	0.35 ± 0.17

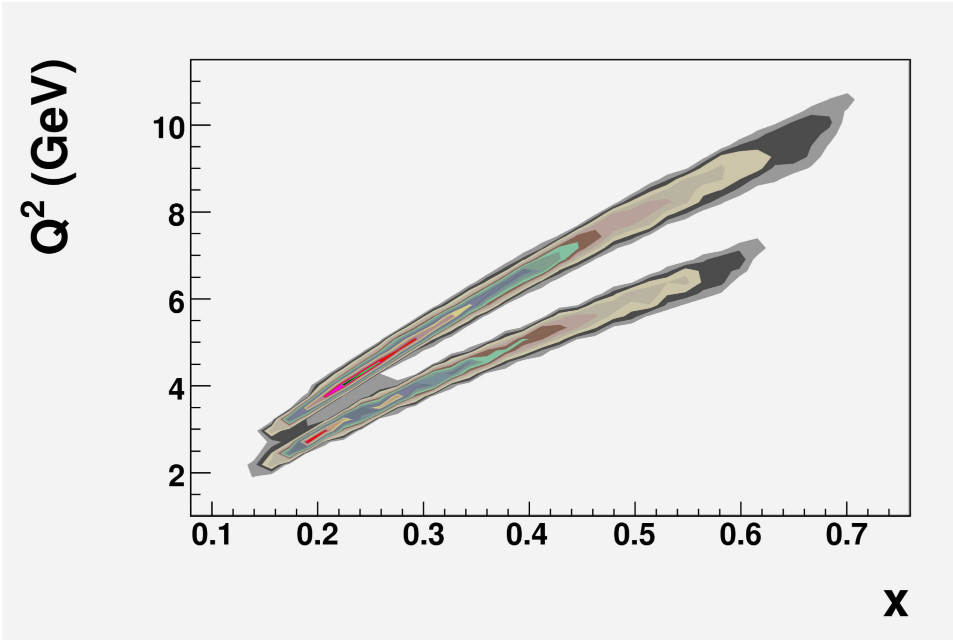

Figure 3.16: Cumulated $E = 8.8$ and $E = 11$ GeV Q^2 vs x phase space (SIDIS cuts applied); upper band refer to $E = 11$ GeV.

3.8 Extraction of the Sivers and Collins Asymmetries

The Collins and Sivers asymmetries are extracted from the measured total asymmetry by a proper fit in the azimuthal sinusoidal modulations (see angular dependent part of Eq. (2.63)). In order to estimate the error of the extraction, we consider the simple Least Square method, where for each kinematical bin, the total measured asymmetry is sampled at various ϕ^i and ϕ_S^j bins, obtaining the following relations:

$$A_{UT}^{exp}(\phi^i, \phi_S^j) = A_{UT}^{Collins,exp} \sin(\phi^i + \phi_S^j) + A_{UT}^{Sivers,exp} \sin(\phi^i - \phi_S^j) + C \tag{3.1}$$

where i) Collins and Sivers amplitudes and ii) the constant C, (which should vanish) represent the unknown parameters to be estimated by a linear fit[8]. For the consistency of this procedure, the full coverage of the Sivers ($\phi - \phi_S$) and Collins ($\phi + \phi_S$) angles is important. The errors on both asymmetries ($\sigma_{A^\pm}$ in short) can be estimated as variance of the parameters in the standard linear least square method:

$$\sigma_{A^\pm} = \frac{1}{\Delta} \cdot \sum_{i,j} \frac{\sin^2(\phi^i \pm \phi_S^j)}{\sigma^2_{A(i,j)}} \tag{3.2}$$

with

$$\Delta = \left| \sum_{i,j} \frac{\sin^2(\phi^i + \phi_S^j)}{\sigma^2_{A(i,j)}} \sum_{i,j} \frac{\sin^2(\phi^i - \phi_S^j)}{\sigma^2_{A(i,j)}} - \left(\sum_{i,j} \frac{\sin(\phi^i + \phi_S^j)\sin(\phi^i - \phi_S^j)}{\sigma^2_{A(i,j)}} \right)^2 \right| \tag{3.3}$$

[8] Suppressed asymmetries modulated by the corresponding sin or cos functions can be included in the expression and considered as additional parameters of the fit.

Table 3.4: $E = 11$ GeV, π^+ total events and corresponding asymmetry accuracy for $3.9 \cdot 10^{36}$ neutron/cm^2/s luminosity, single target setting, 40 days of running, both x and z binning (bin width 0.1×0.1).

$E = 11$ GeV, π^+ Semi-Inclusive Event Statistics and Asymmetry Accuracy												
	$\langle z \rangle = 0.25$		$\langle z \rangle = 0.35$		$\langle z \rangle = 0.45$		$\langle z \rangle = 0.55$		$\langle z \rangle = 0.65$		full z range	
$\langle x \rangle$	$N_{\pi+}$	σ_A	$N_{\pi+}$	σ_A	$N_{\pi+}$	σ_A	$N_{\pi+}$	σ_A	$N_{\pi+}$	σ_A	$N_{\pi+}$	σ_A
	kEvts	%	kEvts	%	kEvts	%	kEvts	%	kEvts	%	kEvts	%
0.20	29766	0.13	17045	0.18	10030	0.24	5405	0.33	3264	0.44	65510	0.09
0.30	18960	0.19	11207	0.26	6353	0.35	3801	0.46	2320	0.60	42640	0.13
0.40	8832	0.32	5215	0.44	3156	0.58	1730	0.79	1084	1.03	20017	0.22
0.50	4126	0.53	2535	0.72	1358	1.01	848	1.30	437	1.88	9306	0.37
0.60	1099	1.13	592	1.68	361	2.22	206	3.00	51	6.25	2310	0.83

Table 3.5: $E = 11$ GeV, K^+ total events and corresponding asymmetry accuracy for $3.9 \cdot 10^{36}$ neutron/cm^2/s luminosity, single target setting, 40 days of running, both x and z binning (bin width 0.1×0.1).

$E = 11$ GeV, K^+ Semi-Inclusive Event Statistics and Asymmetry Accuracy												
	$\langle z \rangle = 0.25$		$\langle z \rangle = 0.35$		$\langle z \rangle = 0.45$		$\langle z \rangle = 0.55$		$\langle z \rangle = 0.65$		full z range	
$\langle x \rangle$	N_{K+}	σ_A	N_{K+}	σ_A	N_{K+}	σ_A	N_{K+}	σ_A	N_{K+}	σ_A	N_{K+}	σ_A
	kEvts	%	kEvts	%	kEvts	%	kEvts	%	kEvts	%	kEvts	%
0.20	4917	0.33	3017	0.44	1541	0.62	907	0.82	495	1.13	10878	0.23
0.30	3289	0.46	2070	0.61	1207	0.81	680	1.09	367	1.53	7612	0.31
0.40	1731	0.72	976	1.02	579	1.35	328	1.82	182	2.52	3796	0.51
0.50	757	1.23	450	1.72	255	2.34	151	3.09	71	4.69	1684	0.87
0.60	330	2.12	197	3.01	111	4.09	56	5.91	18	10.96	712	1.53

where $A(i,j) = A_{UT}^{exp}(\phi^i, \phi_S^j)$.

Replacing the sums on the modulation sin's by the angular integral on $[0.2\pi]$ and assuming the constant error $\sigma_A^{bin} =\sim \sigma_A\sqrt{N}/\sqrt{N/n_b} = \sigma_A\sqrt{n_b}$ on the binned $A(i,j)$ (scaled by the number of bins n_b) uncertainties on both asymmetries are equal to $\sigma_{AC/S} \sim \sigma_A\sqrt{n_b}/(\pi\sqrt{2}) \sim 2\sigma_A$, for a reasonable number of bins $n_b \sim 64 \div 100$, σ_A is given in Tab. 3.4 and Tab. 3.5. Similar tables have been extracted for the negative hadrons with a statistical accuracy slightly higher (up to 70% for K^-).

The statistical accuracies in the case of a 2D extraction, are therefore expected to stay well below 10% except for few marginal points. In this context a deep knowledge of the systematic effects is needed, among them the nuclear target systematics effects play a sizable role. Therefore, the focus of the following two Chapters will be on the nuclear structure of the ^{3}He target and on a new phenomenological description developed in order to better describe the nuclear structure of the polarized ^{3}He target.

Chapter 4

The ^{3}He distorted spectral function

As discussed in the previous Chapters, to achieve a sound flavor decomposition of the TMDs, and in particular of the Sivers and transversity functions, data concerning neutron partonic structure are needed. To gather information on the neutron by using an electromagnetic probe, the most convenient choice is to use a polarized ^{3}He as an effective neutron target (the em response of a polarized ^{3}He is at $\sim$ 90 % the one given by a neutron). Indeed, first results, but affected by sizable statistical errors has been already obtained and used (see Fig.2.9). The phenomenological model adopted for extracting the neutron SSA [57] is based on the knowledge of the ^{3}He nuclear Spectral Function calculated in the so-called Plane Wave Impulse Approximation (PWIA), where in nuclear final state is disregarded *only the final state interaction (FSI) between the struck nucleon and the spectator pair* (see the next Section). Such a residual FSI effect, that could play, in principle, a non trivial role in the extraction of the neutron information from the experimental data, is one of the issues addressed by the present thesis, through the development of a suitable approach. As mentioned before, the next generation fixed target experiments will be on the edge of the intensity frontier. Therefore, since the statistical error on the measurements will be extremely small, (i) a better knowledge of the reaction mechanisms involved in ^{3}He SSA (from which one extract the neutron SSA) becomes crucial in all the planned experiments which are going to use such a target [58] and (ii) the investigation of the assumption that FSI play a negligible role in the description of SIDIS processes has to be carefully carried out.
In this Chapter, our aim is to extensively study the properties of an $A = 3$ nucleus em response after introducing the (residual) FSI effects through the so-called Generalized Eikonal Approximation. In such a way a new *Spectral Function*, which is the key quantity needed to describe the structure of a nuclear system, has been calculated including FSI. We will show that a better knowledge of this function is very important in SIDIS processes.
In particular two kinds of SIDIS can be considered: i) the one we call *standard SIDIS* that is the one in which a leading meson is detected in coincidence of the scattered lepton (as described in Chapter 2); ii) the one we call *spectator SIDIS* where the spectator (no electromagnetically interacting) system is detected in coincidence with the scattered lepton. The following results, which are part of the work carried out for present thesis, are obtained in the context of the spectator SIDIS (considering a deuteron as hadron detected state); the results have been already published

in Ref.[59], where asymmetries and cross sections of a spectator SIDIS process are also shown.

4.1 The cross section

In a SIDIS process, a polarized lepton (in the actual case an electron) is scattered by a polarized nuclear target, with A nucleons, and a final state containing a hadron, a $(A-1)$-spectator system and a residual X' is produced, viz (see Fig.3.1 for a pictorial representation)

$$\vec{l} + \vec{A} \to l' + h + (A-1) + X'$$

Indeed, one has two possible experimental goals: (i) detecting the final hadron h, e.g. a pion or

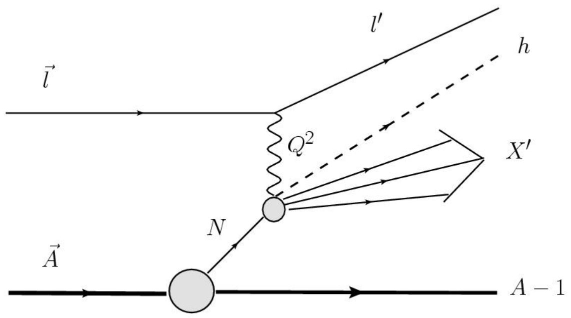

Figure 4.1: Diagrammatic representation of SIDIS processes in PWIA. In standard SiDIS reactions, the hadron h, originated from the current quark fragmentation, is detected. In spectator SiDIS processes, the $(A-1)$-nucleon system is detected in place of the hadronic state h.

a kaon, originating from the struck quark or (ii) detecting the recoiling $(A-1)$-spectator system. The first type of experimental setup allows one to investigate the so-called standard SIDIS, while the second one access the information of the spectator SIDIS. The differential cross section for a generic SIDIS with an incoming electron, can be written as follows (see,e.g., [23, 60])

$$\frac{d\sigma}{d\varphi_e dx_{Bj} dy} = \frac{\alpha_{em}^2 \, m_N y}{Q^4} \, L^{\mu\nu}(\ell) W_{\mu\nu}^{s.i.}(S_A, Q^2, P_h). \tag{4.1}$$

where $Q^2 = -q^2 = -(l-l')^2 = \vec{q}^{\,2} - \nu^2 = 4\mathcal{E}\mathcal{E}' \sin^2(\theta_e/2)$ (with $\vec{q} = \vec{l} - \vec{l}'$, $\nu = \mathcal{E} - \mathcal{E}'$ and $\theta_e \equiv \theta_{\widehat{\vec{k}\vec{k}'}}$); $y = \nu/\mathcal{E}$, $x_{Bj} = Q^2/2m_N\nu$ the Bjorken scaling variable, m_N the nucleon mass, α_{em} the electromagnetic fine structure constant and P_h the detected-hadron 4-momentum.
The leptonic tensor $L_{\mu\nu}$ is the same of (2.3) and it is a calculable quantity in QED. The semi inclusive (s.i.) hadronic tensor of the target with polarization four-vector S_A and mass $M_A^2 = P_A^2$ is defined as

$$\begin{aligned} W_{\mu\nu}^{s.i.}(S_A, Q^2, P_h) = \quad & \frac{1}{4\pi M_A} \sum_X \langle S_A, P_A | J_\mu | P_h, X \rangle \langle P_h, X | J_\nu | S_A, P_A \rangle \\ & (2\pi)^4 \delta^4 \left(P_A + q - P_X - P_h \right) \, d\tau_X \, \frac{d\mathbf{P}_h}{2E_h (2\pi)^3}. \end{aligned} \tag{4.2}$$

where the covariant normalization $\langle p|p'\rangle = 2E(2\pi)^3\delta(\mathbf{p}-\mathbf{p}')$ has been assumed and $d\tau_X$ indicates the suitable phase-space factor for the undetected hadronic state $X \equiv (A-1)+X'$. It should be pointed out that in Eq. (4.2) the integration over the phase-space volume of the detected hadron, h, does not have to be performed.

4.1.1 The Plain Wave Impulse Approximation

Within PWIA, one can relate the nuclear tensor $W^{s.i.}_{\mu\nu}(S_A, Q^2, P_h)$ to the one of a single nucleon $w^{s.i.}_{\mu\nu}(S_N, Q^2, P_h)$, by using the following standard assumptions [61]:

i) the nuclear current operator J_μ is approximated by a sum of single nucleon free current operators j^N_μ ,

ii) the interaction of the debris originating by the struck nucleon with the fully interacting $(A-1)$ nuclear system is disregarded, as suggested by the kinematics of the processes under investigation (notice that in this case the channel $1+(A-1)$ is the dominant one in the A-nucleon final states);

iii) the coupling of the virtual photon with the spectator $(A-1)$ system is neglected (given the high momentum transfer),

iv) the effect of the boosts is not considered.

Due to the assumption ii) here above, the complicated final hadron states $|P_h, X\rangle$ (where $X \equiv (A-1)+X'$) in Eq. (4.2) are approximated by a tensor product of hadronic states, viz

$$|P_h, X\rangle \overset{PWIA}{\approx} |P_{A-1}\rangle \otimes |P_h\rangle \otimes |X'\rangle \,, \tag{4.3}$$

where $|P_{A-1}\rangle$ is a short notation for indicating the state of the fully-interacting $(A-1)$-nucleon system, which acts merely as a spectator, $|X'\rangle$ the baryonic state, that originates together with $|P_h\rangle$ from the hadronization of the quark which has absorbed the virtual photon, and of the other colored remnants. The completeness of the $|P_{A-1}\rangle$ states is written as follows

$$\sum\!\!\!\!\!\!\!\int_{\epsilon^*_{A-1}} \rho\left(\epsilon^*_{A-1}\right) \int \frac{d\mathbf{P}_{A-1}}{2E_{A-1}(2\pi)^3} |\Phi_{\epsilon^*_{A-1}}, \mathbf{P}_{A-1}\rangle\langle\Phi_{\epsilon^*_{A-1}}, \mathbf{P}_{A-1}| = 1 \,, \tag{4.4}$$

where $\Phi_{\epsilon^*_{A-1}}$ is the intrinsic part of the $(A-1)$-nucleon state, with eigenvalue ϵ^*_{A-1}, and $E_{A-1} = \sqrt{(M^*_{A-1})^2 + |\mathbf{P}_{A-1}|^2}$ with $M^*_{A-1} = Z_{A-1}m_p + (A-1-Z_{A-1})m_n + \epsilon^*_{A-1}$. The symbol with the sum overlapping the integral indicates that the $(A-1)$ system has both discrete and continuum energy spectra: this corresponds to negative and positive values of the eigenvalue ϵ^*_{A-1}, respectively. In Eq. (4.4), $\rho\left(\epsilon^*_{A-1}\right)$ is the proper state density, that for $A=3$ in the two-body break-up (2bbu) and three-body break-up (3bbu) reads

$$\rho_{2bbu} = \frac{1}{(2\pi)^3} \,, \qquad \rho_{3bbu} = \frac{1}{(2\pi)^6}\frac{m_N\sqrt{m_N\epsilon^*_2}}{2} \tag{4.5}$$

By using the assumptions i) - iv) and the approximate final state of Eq. (4.3), one gets the following approximation for the matrix elements of the full current in Eq. (4.2)

$$\langle P_h, X|J_\nu|S_A, P_A\rangle \approx \sum_\lambda \int \frac{d\mathbf{P}_N}{2\mathcal{E}_N(2\pi)^3} \langle P_h; X'|j_{1\nu}|\lambda, P_N\rangle\langle\lambda, P_N; \Phi_{\epsilon^*_{A-1}}, \mathbf{P}_{A-1}|S_A, P_A\rangle \tag{4.6}$$

where $P_N \equiv \{\mathcal{E}_N = \sqrt{m_N^2 + |\mathbf{P}_N|^2}, \mathbf{P}_N\}$, λ is the spin projection and the notation $\langle A; B|$ represents the Cartesian product of the two states $\langle A|$ and $\langle B|$. Moreover, it has been inserted a complete set of nucleon plane waves, normalized as follows

$$\sum_\lambda \int \frac{d\mathbf{P}_N}{2\mathcal{E}_N(2\pi)^3} |\lambda, P_N\rangle\langle\lambda, P_N| = 1 , \tag{4.7}$$

between the current operator and the A particle state $|P_A, S_A\rangle$. Obviously, the antisymmetry of the identical nucleons is properly implemented in both the the ground state $|P_A, S_A\rangle$ and the $(A-1)$ states. It is worth noting that the overlap $\langle\lambda, P_N; \Phi_{\epsilon^*_{A-1}}, \mathbf{P}_{A-1}|S_A, P_A\rangle$ represents the building block of the notion of spin-dependent spectral function mentioned in the Introduction (see, e.g., [63, 64, 65], for more details and below).
In conclusion, within PWIA one obtains the following expression for the nuclear tensor

$$\begin{aligned} &W^{s.i.}_{\mu\nu}(S^A, Q^2, P_h) = \\ &= \Bigg[\sum_{X',\lambda\lambda'} \sum_N \int \frac{dE}{(2\pi)} \mathcal{O}^{\hat{\mathbf{S}}_A}_{\lambda\lambda'}(\mathbf{p}_N, E)\frac{1}{2E_N}\langle\lambda', \tilde{p}_N|j^N_\mu|P_h, X'\rangle\langle P_h, X'|j^N_\nu|\lambda, \tilde{p}_N\rangle \\ &\times (2\pi)^4\delta^4(P_A + q - P_{A-1} - P_h - P_{X'})\, d\tau_{X'}\Bigg]\, d\mathbf{P}_{A-1}\frac{d\mathbf{P}_h}{2E_h(2\pi)^3}, \end{aligned} \tag{4.8}$$

where $P_{X'} + P_{A-1}$ is in place of P_X; the on-mass-shell four-momentum of the nucleon is $\tilde{p}_N \equiv \{E_N = \sqrt{m_N^2 + |\mathbf{p}_N|^2}, \mathbf{p}_N\}$ with $\mathbf{p}_N = \mathbf{P}_A - \mathbf{P}_{A-1}$ the nucleon three-momentum, fixed by the translational invariance of the initial nuclear vertex (c.f. Fig.4.1) and $(P_A - P_{A-1})^2 \neq m_N^2$.
It should be pointed out that once the assumptions i) - iii) described at the begining of the subsection are introduced, the hadronic tensor in Eq. (4.8) does not longer fulfill the current conservation, and only phenomenological prescriptions can be adopted (see [59] for details) . In what follows, it is relevant the antisymmetric part of the hadronic tensor, that can be modeled by using the factor $\epsilon^{\mu\nu\alpha\beta}q_\alpha$ (see below) and therefore it explicitly fulfills the current conservation.

In Eq. (4.8), the effects of the nuclear structure are encoded in the PWIA overlaps $\mathcal{O}^{\hat{\mathbf{S}}_A}_{\lambda'\lambda}(\mathbf{p}_N, E)$, defined as

$$\begin{aligned} \mathcal{O}^{\hat{\mathbf{S}}_A}_{\lambda\lambda'}(\mathbf{p}_N, E) = &\sum\!\!\!\!\!\!\int_{\epsilon^*_{A-1}} \rho\left(\epsilon^*_{A-1}\right) \langle\Phi_{\epsilon^*_{A-1}}, \lambda, \mathbf{p}_N|S_A, \Phi_A\rangle\langle S_A, \Phi_A|\Phi_{\epsilon^*_{A-1}}, \lambda', \mathbf{p}_N\rangle \times \\ &\delta\left(E + M_A - m_N - M^*_{A-1} - T_{A-1}\right). \end{aligned} \tag{4.9}$$

where T_{A-1} is the kinetic energy of the $A-1$ system. In a non relativistic approach such contribution is disregarded, leading to the identification of E with the usual missing energy,

$E = \epsilon^*_{A-1} + B_A$, with B_A the binding energy of the target nucleus. It should be pointed out that $m_N - E$ is the energy of a nucleon inside the target nucleus, where the $A-1$ system acts as a spectator ($m_N - E = M_A - M^*_{A-1}$ and recall that $M^*_{A-1} = Z_{A-1}m_p + (A-1-Z_{A-1})m_n + \epsilon^*_{A-1}$). To obtain the above expression, it has been exploited the translational invariance to the overlaps that are present in the rhs of Eq. (4.6), viz

$$\langle \Phi_{\epsilon^*_{A-1}}, \mathbf{P}_{A-1}\lambda, \tilde{p}_N | S_A, P_A\rangle = \sqrt{2E_N\, 2E_{A-1}\, 2M_A}\,(2\pi)^3 \times$$
$$\delta\left(\mathbf{P}_A - \mathbf{P}_{A-1} - \mathbf{p}_N\right)\ \langle \Phi_{\epsilon^*_{A-1}}, \mathbf{P}_{A-1}\lambda, \mathbf{p}_N | S_A, \Phi_A\rangle \tag{4.10}$$

where Φ_A is the intrinsic wave function of the target nucleus, with mass M_A and the factor in front of the delta function has been chosen in order to keep the notation of the intrinsic nuclear part as close as possible to the non relativistic case, where the plane waves have the normalization given by $\langle \mathbf{p}|\mathbf{p}'\rangle = (2\pi)^3\,\delta(\mathbf{p}-\mathbf{p}')$.

It is important to emphasize that the overlaps in Eq. (4.9) are nothing else but the matrix elements of the $2 \otimes 2$ spin-dependent spectral function of a nucleon inside the nucleus A, with polarization $\mathbf{S}_A$ [65], the crucial quantity to be introduced in the next section. The diagonal part yields the probability distribution to find a nucleon in the nucleus A with three-momentum $\mathbf{p}_N$, missing energy E and spin projection equal to λ. This entails the following normalization

$$\frac{1}{2}\sum_\lambda \int dE \int d\mathbf{p}_N\, \mathcal{O}^{\hat{\mathbf{S}}_A}_{\lambda\lambda}(\mathbf{p}_N, E) = 1\ . \tag{4.11}$$

In what follows we consider the polarized target in a pure state with the nuclear wave functions having definite spin projections on the spin quantization axis, usually chosen along the polarization vector $\mathbf{S}_A$. Accordingly, in the complete set of the nucleon plane waves, the spin projections λ and λ' are defined with respect to this direction. As for the Cartesian coordinates, we adopt the DIS convention, i.e. the z axis is directed along the three-momentum transfer $\mathbf{q}$ and the plane (x,z) is the scattering plane. Moreover, in the DIS limit ($Q^2 \to \infty$), the direction of the three-momentum transfer coincides with that of the lepton beam, $\mathbf{q} \,||\, \mathbf{k}_e$.

Notice that the semi-inclusive tensor defined by Eq. (4.8) refers to both kinds of SIDIS. Indeed, the standard SIDIS (which is the one we have extensively described in the previous chapter) implies integrations over $d\tau_{X'}$ and $d\mathbf{P}_{A-1}$, while for the spectator process the integrations are performed over $d\tau_{X'}$ and $d\mathbf{P}_h/[2E_h(2\pi)^3]$, respectively. By inserting Eq. (4.8) in Eq. (4.1), the cross section for standard SIDIS, namely when the hadron h is detected, is written within PWIA as follows

$$2E_h\,\frac{d\sigma(h_l)}{d\varphi_e dx_{Bj} dy d\mathbf{P}_h} =$$
$$\frac{\alpha^2_{em}\, y}{2Q^4}\, L^{\mu\nu}(h_l) \sum_{\lambda\lambda'}\sum_N \int d\mathbf{p}_N \int dE\, \frac{m_N}{E_N}\, w^{s.i.}_{\mu\nu}(p_N, P_h, \lambda\lambda')\mathcal{O}^{\hat{\mathbf{S}}_A}_{\lambda\lambda'}(\mathbf{p}_N, E)\ , \tag{4.12}$$

where the integration over $\mathbf{P}_{A-1}$ has been traded off with the one over $\mathbf{p}_N = \mathbf{P}_A - \mathbf{P}_{A-1}$, and the semi-inclusive nucleon tensor (cf. Eq. (4.2)) is given by

$$w^{s.i.}_{\mu\nu}(p_N, P_h, \lambda'\lambda) = \sum_{X'} \langle \tilde{p}_N, \lambda' | j_\mu | P_h, X' \rangle \langle P_h, X' | j_\nu | \tilde{p}_N, \lambda \rangle \delta^4 \left(p_N + q - P_h - P_{X'} \right) d\tau_{X'} \, . \tag{4.13}$$

where $p_N = P_A - P_{A-1} \equiv \{m_N - E, \mathbf{p}_N\}$ is such that $p_N^2 \neq m_N^2 = \tilde{p}_N^2$. This corresponds in the general case to the (2.59) which contains all the leading-twist polarized structure functions contributions. Let us anticipate that within the Light-front description of a Hamiltonian system [71, 72] combined with the Bakamjian-Thomas construction of the Poincaré generators [73], the constituents are on their own mass-shell, and only the Light-front three-momentum is conserved at the interaction vertex where a constituent interacting with the other constituents is involved. This framework represents an alternative to the one adopted in the covariant approaches in Refs. [67, 68, 69] and will be described in the next Chapter.

The cross section for the spectator SIDIS, namely when the slow $(A-1)$ system is detected, is obtained by integrating over the hadronic variables P_h and exploiting the nucleon tensor of a pure inclusive DIS nature, viz

$$\begin{aligned} & w^{DIS}_{\mu\nu}(p_N, Q^2, \lambda'\lambda) = \\ & \frac{1}{(2\pi)} \sum_{X''} \langle \tilde{p}_N, \lambda' | j_\mu | X'' \rangle \langle X'' | j_\nu | \tilde{p}_N, \lambda \rangle (2\pi)^4 \delta^4 \left(p_N + q - P_{X''} \right) \, d\tau_{X''} \, . \end{aligned} \tag{4.14}$$

In Eq. (4.14), the final state X'' could be $X' + h$, with the notation in Fig. (4.1), but, obviously, could be any other state accessible from the given initial state. In conclusion, within PWIA the cross section for a spectator SIDIS becomes

$$\frac{d\sigma(h_l)}{d\varphi_e dx_{Bj} dy d\mathbf{P}_{A-1}} = \frac{\alpha^2_{em} \, y}{2Q^4} \, L^{\mu\nu}(h_l) \sum_{\lambda\lambda'} \sum_N \int dE \, \frac{m_N}{E_N} \, w^{DIS}_{\mu\nu}(p_N, Q^2, \lambda'\lambda) \mathcal{O}^{\hat{\mathbf{S}}_A}_{\lambda\lambda'}(\mathbf{p}_N, E) \tag{4.15}$$

Summarizing, Eqs. (4.12) and (4.15) show that the central quantities for describing SIDIS reactions in PWIA are i) the overlap integrals $\mathcal{O}^{\hat{\mathbf{S}}_A}_{\lambda\lambda'}(\mathbf{p}_N, E)$ which contain information on the nuclear structure effects and ii) the suitable tensor $w_{\mu\nu}$ of a moving nucleon. In particular, the antisymmetric part of the nucleon tensor is the basic ingredient in the evaluation of proper cross section asymmetries, that represent the main goal of the experimental investigation of SIDIS reactions.

4.1.2 The antisymmetric tensor $w^{aDIS}_{\mu\nu}$ of a moving nucleon

Now are we going to consider the spectator SIDIS case, which involves a more simple hadronic tensor than the one needed for standard SIDIS, with the aim to show the main features of the nuclear spectral function without loss of generality. Therefore, the antisymmetric part of the nucleon tensor $w^{DIS}_{\mu\nu}$ (cf Eq. (4.14)) is the relevant quantity. Following Ref. [65] (see also Ref. [64]), the antisymmetric part of the tensor for a nucleon with a definite polarization S_N is given by

$$w^{a,DIS}_{\mu\nu}(p_N, Q^2, \lambda'\lambda) = \langle \lambda' | \hat{w}^{aN}_{\mu\nu} | \lambda \rangle \tag{4.16}$$

where the operator $\hat{w}^{aN}_{\mu\nu}(p_N, Q^2, S_N)$ in Eq. (4.16) can be written as [64, 65, 62, 77, 68, 69]

$$\hat{w}^{aN}_{\mu\nu}(p_N, Q^2, S_N) = i\varepsilon_{\mu\nu\alpha\beta}q^\alpha \Big[m_N \hat{S}^\beta_N G^N_1(Q^2, p_N \cdot q) \\ + \frac{G^N_2(Q^2, p_N \cdot q)}{m_N} \Big((p_N \cdot q)\hat{S}^\beta_N - (S_N \cdot q) p^\beta_N \Big) \Big] , \tag{4.17}$$

In the above expression, the two scalar functions $G_{1,2}$ are the polarized DIS structure functions. and the quantity $\hat{S}_N$ is the four-vector polarization operator acting in the 2×2 spin space. It is defined as

$$\hat{S}^\beta_N = \begin{cases} \dfrac{(\boldsymbol{\sigma}\mathbf{p}_N)}{m_N}, & \beta = 0 \\ \boldsymbol{\sigma} + \mathbf{p}_N \dfrac{(\boldsymbol{\sigma}\mathbf{p}_N)}{m_N(E_N + m_N)}, & \beta = 1,2,3 \end{cases} , \tag{4.18}$$

with $\boldsymbol{\sigma}$ the usual Pauli matrices. As previously announced, the antisymmetric part of the nucleon tensor we are adopting is explicitly current-conserved and, in turn, the corresponding hadronic tensor does. In the present calculation, as in the Relativistic Hamiltonian Dynamics framework, e.g., the one adopted in Ref. [75], the dependence on $p^2_N \neq m^2_N$ of the nucleon structure functions $G_{1,2}$ is neglected.

In standard SiDIS, the analogous of the operator $\hat{w}^{aN}_{\mu\nu}(p_N, Q^2, S_N)$ becomes a more complicated object, since, within the quark parton model, it can be expressed as a convolution of the TMDs with different quark fragmentation functions 2.53 .

4.2 Spectator SIDIS by a polarized ^{3}He target

As shown in Eqs. (4.12) and (4.15), the nuclear effects in both SIDIS reactions are governed by the overlap integrals $\mathcal{O}^{\hat{\mathbf{S}}_A}_{\lambda\lambda'}(\mathbf{p}_N, E)$. In this chapter we focus mostly on the investigation of nuclear effects, and therefore we consider the spectator SIDIS, that has a nucleon tensor, $w^{DIS}_{\mu\nu}$, with less uncertainties in the parton structure. In particular, we consider the case of a polarized ^{3}He target, (one can repeat the same considerations for ^{3}H, modulo the Coulomb effects). For the sake of simplicity, we choose the simplest channel, namely the one with a deuteron in the final state ($A - 1 = D$), this means that one can address the proton structure functions inside the ^{3}He target, while in the mirror nucleus one can study the neutron structure functions. Generalization to the case when the detected system is a two-particle state in the continuum is straightforward, but more involved. In particular, we analyze polarized SIDIS with a longitudinal set up, i.e. the polarization of the initial electron and the target nucleus are defined with respect to the direction of the momentum transfer $\mathbf{q}$. If the detected unpolarized $(A-1)$-nucleon system is a deuteron, $\epsilon^*_{A-1} = -B_D$ and therefore the nucleon missing energy is just the two body break-up (2bbu) threshold energy of ^{3}He, i.e. $E_{2bbu} = B_{^3\mathrm{He}} - B_D$. For the final state we have chosen, the cross section reads

$$\frac{d\sigma^{\hat{\mathbf{S}}_A}(h_e)}{d\varphi_e dx_{Bj} dy d\mathbf{P}_D} = \frac{\alpha^2_{em}\, m_N\, y}{Q^4}\, L^{\mu\nu}(h_e) W^{s.i.}_{\mu\nu}(S^A, Q^2, P_D) \tag{4.19}$$

In this kind of experiments, the observables are asymmetries, i.e.

$$\frac{\Delta\sigma^{\hat{\mathbf{S}}_A}}{d\varphi_e dx_{Bj} dy d\mathbf{P}_D} \equiv \frac{d\sigma^{\hat{\mathbf{S}}_A}(h_e = 1) - d\sigma^{\hat{\mathbf{S}}_A}(h_e = -1)}{d\varphi_e dx_{Bj} dy d\mathbf{P}_D}, \tag{4.20}$$

and only the antisymmetric part of both leptonic and nuclear tensors are involved. In particular, the antisymmetric part of the hadronic tensor $W^{s.i.}_{\mu\nu}$ in Eq. (4.19) reads

$$W^{a,s.i.}_{\mu\nu}(S^A, Q^2, P_D) = \sum_{\lambda\lambda'} \frac{1}{2E_N} \langle\lambda'|\hat{w}^{aN}_{\mu\nu}(p_N, Q^2, S_N)|\lambda\rangle \mathcal{O}^{\hat{\mathbf{S}}_A}_{\lambda\lambda'}(p_N, E_{2bbu}) \ . \tag{4.21}$$

with the nucleon DIS tensor $w^{DIS}_{\mu\nu}(p_N, Q^2, \lambda, \lambda')$ given formally in Eqs. (4.14) and then explicitly in Eqs. (4.16) and (4.17). In the DIS limit, the nucleon structure function G^N_2 yields, at the leading twist, a vanishing contribution to the measured cross section (see i.e. [76]). Therefore, in all the following calculations, contributions from G^N_2 are neglected. Then, the antisymmetric part of the nucleon tensor becomes

$$\begin{aligned}\langle\lambda'|\hat{w}^{aN}_{\mu\nu}|\lambda\rangle &= iG^N_1(Q^2, p_N\cdot q)\varepsilon_{\mu\nu\alpha\beta} m_N q^\alpha \sum_\kappa (-1)^\kappa \ \langle\lambda'|\sigma_{-\kappa}|\lambda\rangle Tr\left(\frac{1}{2}\sigma_\kappa \hat{S}^\beta_N\right). \\ &= -i\sqrt{3}G^N_1(Q^2, p_N\cdot q)\varepsilon_{\mu\nu\alpha\beta} m_N q^\alpha \sum_\kappa (-1)^\kappa \langle 1 - \kappa \frac{1}{2}\lambda|\frac{1}{2}\lambda'\rangle \ \mathcal{B}^\beta_\kappa\end{aligned} \tag{4.22}$$

with

$$\mathcal{B}^\beta_\kappa \equiv Tr\left(\frac{1}{2}\sigma_\kappa \hat{S}^\beta_N\right). \tag{4.23}$$

Notice that Eq. (4.23) defines a "double" vector with double indices: the index $\kappa = 0, \pm 1$, labels three four-vectors, with Lorentz index β. The latter has to be contracted with the corresponding index in the Levi-Civita tensor $\varepsilon_{\mu\nu\alpha\beta}$, see Eq. (4.17). The Cartesian components of $\boldsymbol{\mathcal{B}}^\beta$ are given by (a mixed notation is adopted, but self-explaining)

$$\mathcal{B}^\beta_i = \begin{cases} \dfrac{(\mathbf{p}_N)_i}{m_N}, & \beta = 0 \\ \delta_{\beta i} + (\mathbf{p}_N)^\beta \ \dfrac{(\mathbf{p}_N)_i}{m_N(E_N + m_N)}, & \beta = 1, 2, 3 \end{cases} \tag{4.24}$$

By placing Eq. (4.22) into Eq. (4.21), one can write the nuclear tensor as follows

$$\begin{aligned}W^{a,s.i.}_{\mu\nu} \ (\ S^A, Q^2, P_D) = & \ i\frac{1}{2} G^N_1(Q^2, p_N\cdot q)\varepsilon_{\mu\nu\alpha\beta} \frac{m_N}{E_N} q^\alpha \times \\ & \times \sum_{\lambda\lambda'} \sum_\kappa (-1)^\kappa \left[-\sqrt{3}\langle 1 - \kappa\frac{1}{2}\lambda|\frac{1}{2}\lambda'\rangle \mathcal{O}^{\hat{\mathbf{S}}_A}_{\lambda\lambda'}(\mathbf{p}_N, E_{2bbu}) \right] \ \mathcal{B}^\beta_\kappa\end{aligned} \tag{4.25}$$

It can be seen that the dependence upon the index κ leads to a scalar product of two vectors, viz

$$(\boldsymbol{\mathcal{P}}^{\hat{\mathbf{S}}_A} \cdot \boldsymbol{\mathcal{B}}^\beta) \equiv \sum_\kappa (-1)^\kappa \mathcal{P}^{\hat{\mathbf{S}}_A}_{-\kappa} \mathcal{B}^\beta_\kappa, \tag{4.26}$$

where

$$\mathcal{P}^{\hat{\mathbf{S}}_A}_{\kappa}(\mathbf{p}_N, E_{2bbu}) \equiv -\sqrt{3}\sum_{\lambda\lambda'}\langle 1 - \kappa\frac{1}{2}\lambda|\frac{1}{2}\lambda'\rangle \mathcal{O}^{\hat{\mathbf{S}}_A}_{\lambda\lambda'}(\mathbf{p}_N, E_{2bbu}) \tag{4.27}$$

are the spherical components of the vector $\boldsymbol{\mathcal{P}}^{\hat{\mathbf{S}}_A}$, that represents the contribution to the spin-dependent spectral function from the polarization of the target nucleus (see Ref. [65] for details) in a pure state with polarization $\mathbf{S}_A$ (we reiterate that in Eq. (4.27) the spin quantization is along the nuclear polarization $\mathbf{S}_A$). Then, the antisymmetric part of the nuclear tensor reads

$$W^{as.i.}_{\mu\nu}(S^A, Q^2, P_D) = i\frac{1}{2}G_1^N(Q^2, p_N \cdot q)\, \varepsilon_{\mu\nu\alpha\beta}\frac{m_N}{E_N}q^\alpha \left(\boldsymbol{\mathcal{P}}^{\hat{\mathbf{S}}_A} \cdot \boldsymbol{\mathcal{B}}^\beta\right) \tag{4.28}$$

For further purposes, let us write more explicitly the components of $\boldsymbol{\mathcal{P}}^{\hat{\mathbf{S}}_A}$ both in spherical and Cartesian coordinates. By using the spherical versors, one has

$$\boldsymbol{\mathcal{P}}^{\hat{\mathbf{S}}_A} = \mathcal{P}^{\hat{\mathbf{S}}_A}_{||}\,\mathbf{e}_0 + \mathcal{P}^{\hat{\mathbf{S}}_A}_{1\perp}\,\mathbf{e}_+ + \mathcal{P}^{\hat{\mathbf{S}}_A}_{2\perp}\,\mathbf{e}_- \tag{4.29}$$

where $\mathbf{e}_0||\mathbf{S}_A$ (see, also [62, 65]) and

$$\mathbf{e_0} = \begin{pmatrix} 0 \\ 0 \\ 1 \end{pmatrix}, \quad \mathbf{e}_+ = -\frac{\mathbf{1}}{\sqrt{\mathbf{2}}}\begin{pmatrix} 1 \\ i \\ 0 \end{pmatrix}, \quad \mathbf{e}_- = \frac{\mathbf{1}}{\sqrt{\mathbf{2}}}\begin{pmatrix} 1 \\ -i \\ 0 \end{pmatrix}, \tag{4.30}$$

or, in terms of Cartesian versors

$$\boldsymbol{\mathcal{P}}^{\hat{\mathbf{S}}_A} = \mathcal{P}^{\hat{\mathbf{S}}_A}_x\,\mathbf{e}_x + \mathcal{P}^{\hat{\mathbf{S}}_A}_y\,\mathbf{e}_y + \mathcal{P}^{\hat{\mathbf{S}}_A}_z\,\mathbf{e}_z. \tag{4.31}$$

Usually, the DIS kinematics is defined in a coordinate system with the z-axis along the three-momentum transfer $\mathbf{q}$, whereas the quantization direction to determine the particle polarizations is along the beam direction $\mathbf{k_e}$. In the Bjorken limit $\mathbf{q} \simeq \mathbf{k}_e$ and the two directions coincide. This remark will become helpful once FSI are introduced. The x-axis is then chosen to be either in the scattering or in the reaction plane; however, $\mathbf{e}_y = [\mathbf{e}_z \times \mathbf{e}_x]$.

In terms of the overlap integrals, Eq. (4.9), the components of $\boldsymbol{\mathcal{P}}^{\hat{\mathbf{S}}_A}$ are expressed in spherical basis by

$$\mathcal{P}^{\hat{\mathbf{S}}_A}_{||} = \mathcal{O}^{\hat{\mathbf{S}}_A}_{\frac{1}{2}\frac{1}{2}} - \mathcal{O}^{\hat{\mathbf{S}}_A}_{-\frac{1}{2}-\frac{1}{2}}; \quad \mathcal{P}^{\hat{\mathbf{S}}_A}_{1\perp} = -\sqrt{2}\mathcal{O}^{\hat{\mathbf{S}}_A}_{\frac{1}{2}-\frac{1}{2}}; \quad \mathcal{P}^{\hat{\mathbf{S}}_A}_{2\perp} = \sqrt{2}\mathcal{O}^{\hat{\mathbf{S}}_A}_{-\frac{1}{2}\frac{1}{2}}, \tag{4.32}$$

and in Cartesian basis by

$$\mathcal{P}^{\hat{\mathbf{S}}_A}_z = \mathcal{P}^{\hat{\mathbf{S}}_A}_{||}; \quad \mathcal{P}^{\hat{\mathbf{S}}_A}_x = 2\Re\,\mathcal{O}^{\hat{\mathbf{S}}_A}_{\frac{1}{2}-\frac{1}{2}}; \quad \mathcal{P}^{\hat{\mathbf{S}}_A}_y = -2\Im\,\mathcal{O}^{\hat{\mathbf{S}}_A}_{\frac{1}{2}-\frac{1}{2}}, \tag{4.33}$$

It should be noted that, since in Eq. (4.29) the last two terms are mutually complex conjugated, one has only only two independent components, e.g., $\mathcal{P}^{\hat{\mathbf{S}}_A}_{||}$ and $\mathcal{P}^{\hat{\mathbf{S}}_A}_{1\perp}$. This is a consequence of the fact that in the considered reaction one has at disposal only two vectors, $\mathbf{S}_A$ and $\mathbf{p}_N$ from which a pseudovector $\boldsymbol{\mathcal{P}}^{\hat{\mathbf{S}}_A}$ can be constructed [65, 88], viz

$$\boldsymbol{\mathcal{P}}^{\hat{\mathbf{S}}_A}(\mathbf{p}_N, E) = \mathbf{S}_A B_1(|\mathbf{p}_N|, E) + \hat{\mathbf{p}}_N\,(\hat{\mathbf{p}}_N \cdot \mathbf{S}_A)\, B_2(|\mathbf{p}_N|, E)\,. \tag{4.34}$$

where $B_1(|\mathbf{p}_N|, E)$ and $B_2(|\mathbf{p}_N|, E)$ are scalar functions to be constructed from the overlaps. By using Eqs. (4.32) and some algebra, it is easily seen that Eqs. (4.29) and (4.34) become equivalent. It should be emphasized that in presence of FSI the spin-dependent spectral function additionally depends upon the direction of the momentum transfer $\mathbf{q}$, so that the simple form given in Eq. (4.34) does not longer hold.

Let us analyze in more details the 2bbu contribution to the spin-dependent spectral function of a $A = 3$ nucleus, within the PWIA framework. In the actual calculations, both the ^{3}He (target) wave function and the deuteron one correspond to exact solutions of the Schrödinger equation with the AV18 nucleon-nucleon potential [55]. In particular, for ^{3}He, the wave function of Ref. [78], but without Coulomb effects, has been adopted, namely it can be applied for describing also ^{3}H.

The overlaps $\mathcal{O}^{\hat{\mathbf{S}}_A}_{\lambda\lambda'}$ in Eqs. (4.8) and (4.9) are explicitly written as

$$\mathcal{O}^{\hat{\mathbf{S}}_A}_{\lambda\lambda'}(\mathbf{p}_N, E_{2bbu}) = \sum_{M_D} \Bigg[\sum_{\{\alpha,\tilde{\alpha}\}} \langle X M_X L_\rho M_\rho | \frac{1}{2} M_A \rangle \langle \tilde{X} \tilde{M}_X \tilde{L}_\rho \tilde{M}_\rho | \frac{1}{2} M_A \rangle \langle 1 M_D \frac{1}{2} \lambda | X M_X \rangle$$

$$\langle 1 M_D \frac{1}{2} \lambda' | \tilde{X} \tilde{M}_X \rangle (4\pi)^2 i^{L_\rho} (-i)^{\tilde{L}_\rho} \mathrm{Y}_{L_\rho M_\rho}(\hat{\mathbf{p}}_N) \mathrm{Y}^*{}_{\tilde{L}_\rho \tilde{M}_\rho}(\hat{\mathbf{p}}_N) O_\alpha(|\mathbf{p}_N|, E_{2bbu}) O_{\tilde{\alpha}}(|\mathbf{p}_N|, E_{2bbu}) \Bigg] \quad (4.35)$$

where the radial overlaps $O_\alpha(|\mathbf{p}_N|)$ are given by

$$O_\alpha(|\mathbf{p}_N|, E_{2bbu}) = \int d\rho\, \rho^2 \int dr_{23}\, r_{23}\, j_{L_\rho}(\rho|\mathbf{p}_N|) R_\alpha(r_{23}, \rho) \Psi_{L_D}(r_{23}) \quad (4.36)$$

with $\boldsymbol{\rho}$ and $\mathbf{r}_{23}$ the two Jacobi coordinates: $\mathbf{r}_{23} = \mathbf{r}_2 - \mathbf{r}_3$ and $\boldsymbol{\rho} = \mathbf{r}_1 - (\mathbf{r}_2 + \mathbf{r}_3)/2$. In Eq. (4.35), $\{\alpha\}$ denotes the quantum numbers of a "deuteron-like" configuration, i.e. $L_\rho, X, j_{23} = 1, L_{23} = L_D = 0, 2$ with the corresponding projections M_ρ, M_X, M_D (see below). Eventually $R_\alpha(r_{23}, \rho)$ and $\Psi_{L_D}(r_{23})$ describe the target and deuteron radial wave functions, respectively, viz

$$\begin{aligned}
&\langle \sigma_1, \sigma_2, \sigma_3; T_{23}, \tau_{23}, \tau; \boldsymbol{\rho}, \mathbf{r}_{23} | ^3\mathrm{He}; \frac{1}{2} M_A; \frac{1}{2} T_z \rangle = \\
&= \langle T_{23} \tau_{23} \frac{1}{2} \tau | \frac{1}{2} T_z \rangle \sum_{L_\rho M_\rho} \sum_{X M_X} \sum_{j_{23} m_{23}} \langle X M_X L_\rho M_\rho | \frac{1}{2} M_A \rangle\; \langle j_{23} m_{23} \frac{1}{2} \sigma_1 | X M_X \rangle \\
&\times \sum_{S_{23} m_{S_{23}}} \sum_{L_{23} M_{23}} \langle \frac{1}{2} \sigma_2 \frac{1}{2} \sigma_3 | S_{23} m_{S_{23}} \rangle \langle L_{23} M_{23} S_{23} m_{S_{23}} | j_{23} m_{23} \rangle \\
&\times Y_{L_{23} M_{23}}(\hat{\mathbf{r}}_{23})\; Y_{L_\rho M_\rho}(\hat{\boldsymbol{\rho}})\; \phi^{j_{23} L_{23} S_{23}}_{L_\rho X}(r_{23}, \rho)
\end{aligned} \quad (4.37)$$

with $\phi^{j_{23} L_{23} S_{23}}_{L_\rho X}(r_{23}, \rho) \equiv R_\alpha(r_{23}, \rho)$, and

$$\langle \mathbf{r}_{23}, | D; 1 M_D \rangle = \frac{\Psi_{0_D}(r_{23})}{r_{23}}\, \mathcal{Y}^{M_D}_{011}(\hat{\mathbf{r}}_{23}) + \frac{\Psi_{2_D}(r_{23})}{r_{23}}\, \mathcal{Y}^{M_D}_{211}(\hat{\mathbf{r}}_{23}) \quad (4.38)$$

In Eq. (4.35), the ϕ-dependence of the overlaps, and in turn of $\boldsymbol{\mathcal{P}}^{\hat{\mathbf{S}}_A}$ (cf Eq. (4.33)) is entirely governed by the difference $M_\rho - \tilde{M}_\rho$, which does not depend upon the internal summation, namely

$M_\rho - \tilde{M}_\rho = \lambda' - \lambda$. This implies, according to Eq. (4.32), that the parallel component $\mathcal{P}_{||}(\mathbf{p}_N, E)$ does not depend upon ϕ, while the perpendicular ones, $\mathcal{P}_{1\perp}(\mathbf{p}_N, E)$ and $\mathcal{P}_{2\perp}(\mathbf{p}_N, E)$, have a functional dependence given by $\exp(\mp i\phi)$, respectively (see Ref. [62]).

4.2.1 Final state interaction effects

Let us now consider the FSI effects, that hav not taken into account within PWIA (recall that the $(A-1)$-nucleon spectator system is fully interacting in PWIA). In what follows, we shortly indicated the residual interaction as *FSI effects* They are due to

i) the propagation of the nucleon debris formed after the γ^* absorption by a target quark, followed by its hadronization

ii) the interactions of the produced hadrons with the $(A-1)$ spectator system, as schematically depicted in Fig. 4.2.

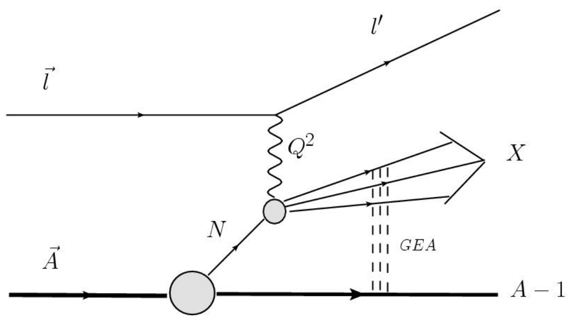

Figure 4.2: A diagrammatic illustration of FSI in spectator SiDIS. The rescattering processes between the quark debris and the nucleons inside the $(A-1)$ system are treated within a generalized eikonal approximation (GEA) [79].

Indeed, the calculation of such FSI effects from first principles represents a very complicated many-body problem, so that proper model approaches have to be developed. To this end, one is guided by the observation that in the DIS kinematics we are considering: i) the momentum of the spectator nucleus $|\mathbf{P}_{A-1}|$ is small; ii) the large momentum transfer $|\mathbf{q}|$ leads to a very large relative momentum between the debris (with momentum $\mathbf{p}_X$) and the nucleon i (with momentum $\mathbf{k}_i$) inside the $(A-1)$ system, i.e. $|(\mathbf{p}_X - \mathbf{k}_i)| \simeq |\mathbf{q}| \gg |\mathbf{k}_i|$ (remind that the distribution of $|\mathbf{k}_i|$ is driven by the target wave function); iii) the momentum transfer in the rescattering processes $|\mathbf{p}'_X - \mathbf{p}_X|$, i.e. when the debris interacts with the nucleons inside the $(A-1)$ system, has the typical magnitude of the high-energy elastic NN scattering, i.e. much smaller than the incident momentum $|\mathbf{p}_X|$ of the debris. In this case, the rescattering wave function can be approximated by its eikonal form (in terms of T-matrix: $T(\mathbf{p}_X, \mathbf{k}_i; \mathbf{p}'_X, \mathbf{k}'_i) \to T^{eik}(\mathbf{p}_X)$, that allows one to describe the propagation of the debris produced after the γ^* absorption by a target quark, while both hadronization processes and interactions between the just produced pre-hadrons and the spectator nucleons take place. This series of soft interactions with the spectator system can be characterized by an effective cross section $\sigma_{eff}(z, Q^2, x)$ that depends upon time (or the distance z traveled by the system X). Such an effective cross section allows one to construct a realistic profile function, that determines the eikonal approximation (see below) [79, 80, 81, 82]. As a result, in presence of FSI, the PWIA overlaps given in Eq. (4.9) should be replaced by the suitable ones that encode FSI effects. In the 2bbu channel, where the asymptotic three-momentum of the spectator system is $\mathbf{P}_{A-1} = \mathbf{P}_D$ (we are considering a ^{3}He target), one has, for the matrix elements of the one-body current, an expression that has the following schematic form

$$\langle \hat{S}(1,2,3)\{\mathbf{p}_X; \mathbf{P}_D\Psi_D\}|j_\mu^N|\Psi_{He}\rangle = \int d\mathbf{p}_N \langle \mathbf{p}_X|j_\mu^N|\mathbf{p}_N\rangle \ \langle \mathbf{p}_N; \mathbf{P}_D\Psi_D|\hat{S}_{Gl}(1,2,3)|\Psi_{He}\rangle \tag{4.39}$$

where $\hat{S}_{Gl}(1,2,3)$, represents the debris-nucleon eikonal scattering S-matrix, that depends upon the relative coordinates only, and it has been assumed to commute with j^μ. This leads to consider overlaps like $\langle \mathbf{p}_N; \mathbf{P}_D\Psi_D|\hat{S}_{Gl}(1,2,3)|\Psi_{He}\rangle$ (cf Eq. (6) in Ref. [79]). The operator $\hat{S}_{Gl}(1,2,3)$ can be written as follows

$$\hat{S}_{Gl}(\mathbf{r}_1, \mathbf{r}_2, \mathbf{r}_3) = \prod_{i=2,3} \left[1 - \theta(z_i - z_1)\Gamma(\mathbf{b}_1 - \mathbf{b}_i, z_1 - z_i)\right] , \tag{4.40}$$

where $\mathbf{b}_i$ and z_i are the perpendicular and parallel components of $\mathbf{r}_i$ (remind that $\mathbf{r}_1 + \mathbf{r}_2 + \mathbf{r}_3 = 0$), with respect to the direction of the propagation of the debris $\mathbf{p}_X$. In the DIS limit, one has $\mathbf{p}_X \simeq \mathbf{q}$ and the eikonal S-matrix is defined with respect to $\mathbf{q}$. This implies that a dependence upon $\mathbf{q}$ has to be taken into account, but it is not explicitly indicated to avoid a too heavy notation; however this will be recalled at the proper places. The profile function, Γ, is given by

$$\Gamma(\mathbf{b}_{1i}, z_{1i}) \ = \ \frac{(1 - i\,\alpha) \ \sigma_{eff}(z_{1i})}{4\,\pi\, b_0^2} \ \exp\left[-\frac{\mathbf{b}_{1i}^2}{2\, b_0^2}\right] \ . \tag{4.41}$$

where $\mathbf{r}_{1i} = \{\mathbf{b}_{1i}, \mathbf{z}_{1i}\}$ with $\mathbf{z}_{1i} = \mathbf{z}_1 - \mathbf{z}_i$ and $\mathbf{b}_{1i} = \mathbf{b}_1 - \mathbf{b}_i$. It can be seen that, in the present generalized eikonal approximation, unlike in the standard Glauber approach, the profile function Γ depends not only upon the transverse relative separation but also upon the longitudinal separation $z_{1,i}$ due to the z- (or time) dependence of the effective cross section $\sigma_{eff}(z_{1i})$ and the causal θ-function, $\theta(z_i - z_1)$. In principle, the effective cross section, $\sigma_{eff}(z_{1i})$ also depends on the total energy of the debris, $W^2 \equiv P_X^2 = (p_N + q)^2$. However, if the energy is not too large and the hadronization process takes place inside the nucleus $(A-1)$, the dependence on W^2 is weak, and the number of produced hadrons can be taken constant.

Therefore, one can assume $\sigma_{eff}(z_{1i}, x_{Bj}, Q^2) \sim \sigma_{eff}(z_{1i})$ [82, 79]. Let us briefly discuss the parameters entering Eq. (4.41), i.e. the profile function adopted in our model. Indeed, it is the same expression exploited in Ref. [79] in order to nicely describe the data measured at JLab [82], corresponding to the unpolarized spectator SIDIS off the deuteron. Also the numerical values of the parameters present in Eq. (4.41) are the same as in [79], and obviously, given the lack of data for the polarized case (as well as theoretical calculations), the choice should be considered as a conservative one. In particular, σ_{eff} is the cross section for the interaction of the formed hadrons (assumed to be a nucleon and a few pions) with the remnant nucleons. Hence, σ_{eff} is given by the sum of two contributions: i) the nucleon-nucleon cross section, σ_{NN}, and ii) $\sigma_{\pi N}\ N_\pi^{eff}$, i.e. the nucleon-pion cross section times the effective number of pions which are produced, N_π^{eff} (cf Ref. [81] for the explicit evaluation). As to the parameter α in Eq. (4.41), it represents the ratio of the real to the imaginary part of the forward scattering amplitude of the process. At the energies we are considering, α is basically the same for NN and for πN interactions, and in our calculation it has been taken constant, namely, $\alpha = -0.5$, following [79]. Finally, the slope parameter, b_0, is determined by the optical theorem, which yields $b_0^2 = \sigma_{eff}^2(1+\alpha^2)/[16\pi\sigma^{el}]$, where σ^{el} is the elastic part of the total effective cross section σ_{eff}. The values we used for the relevant cross sections are the same as in Ref. [79], i.e. $\sigma_{NN}^{el} = 20$ mb, $\sigma_{\pi N}^{el} = 10$ mb, $\sigma_{NN}^{tot} = 40$ mb, $\sigma_{\pi N}^{tot} = 25$ mb. As a general remark, it should be pointed out that GEA has been successfully applied for studying at high energy both semi-inclusive and exclusive quasi-elastic scattering off nuclei (see, e.g. Refs. [83, 84, 85]).

In conclusion, within the adopted approximation, the overlaps that include the FSI effects are given by

$$\begin{aligned}
&\mathcal{O}_{\lambda\lambda'}^{S_A(FSI)}(\mathbf{P_D}, E_{2bbu}) = \\
&\left\langle \hat{S}_{Gl}(1,2,3)\left\{\Psi_{\mathbf{P}_D},\lambda,\mathbf{p}_N\right\}|S_A,\Phi_A\right\rangle \left\langle \Phi_A, S_A|\hat{S}_{Gl}(1,2,3)\left\{\Psi_{\mathbf{P}_D},\lambda',\mathbf{p}_N\right\}\right\rangle = \\
&\sum_{M_D}\left[\sum_{\{\alpha,\tilde{\alpha}\}}\langle XM_X L_\rho M_\rho|\frac{1}{2}M_A\rangle\langle \tilde{X}\tilde{M}_X\tilde{L}_\rho\tilde{M}_\rho|\frac{1}{2}M_A\rangle\langle j_{23}m_{23}\frac{1}{2}\lambda|XM_X\rangle\langle \tilde{j}_{23}\tilde{m}_{23}\frac{1}{2}\lambda'|\tilde{X}\tilde{M}_X\rangle\right. \\
&\langle l_{23}\mu_{23}1M_S|j_{23}m_{23}\rangle\langle \tilde{l}_{23}\tilde{\mu}_{23}\tilde{1}M_S|\tilde{j}_{23}\tilde{m}_{23}\rangle\langle L_D m_L 1M_S|1M_D\rangle\langle \tilde{L}_D\tilde{m}_L\tilde{1}M_S|1M_D\rangle \\
&O_\alpha^{(FSI)}(\mathbf{P}_D, E_{2bbu})\, O_{\tilde{\alpha}}^{(FSI)}(\mathbf{P}_D, E_{2bbu}),
\end{aligned} \tag{4.42}$$

where

$$\begin{aligned}
O_\alpha^{(FSI)}(\mathbf{P}_D, E_{2bbu}) &= \int d\boldsymbol{\rho}\int d\mathbf{r}_{23} e^{i\mathbf{P}_D\boldsymbol{\rho}} S_{Gl}(\mathbf{r}_{23},\boldsymbol{\rho})\frac{\Psi_{L_D}(|\mathbf{r}_{23}|)}{|\mathbf{r}_{23}|}\, \mathrm{Y}_{L_D m_L}(\hat{\mathbf{r}}_{23}) \\
&\times \mathrm{Y}_{L_\rho M_\rho}(\hat{\boldsymbol{\rho}})\mathrm{Y}_{l_{23}\mu_{23}}(\hat{\mathbf{r}}_{23})\, R_\alpha(|\mathbf{r}_{23}|,|\boldsymbol{\rho}|).
\end{aligned} \tag{4.43}$$

with $S_{Gl}(\mathbf{r}_{23},\boldsymbol{\rho})$ the non-singular part of the matrix elements of $\hat{S}_{Gl}(1,2,3)$ (remind that the adopted eikonal S-matrix is diagonal in the Jacobi-coordinate basis). A further issue is represented by the fact that the direction of the target polarization-axis, $\hat{\mathbf{k}}_e$, is not totally parallel to the the direction which determines the eikonal S-matrix, i.e. $\hat{\mathbf{p}}_X$. Indeed, in the Bjorken limit, the momentum transfer $\mathbf{q}$ is almost parallel to the beam direction $\mathbf{k}_e$ so that in this case one can choose the quantization z-axis along the beam direction and perform calculations of FSI effects within such a coordinate system, since $\hat{\mathbf{k}}_e \simeq \hat{\mathbf{q}} \simeq \hat{\mathbf{p}}_X$. However, at finite values of $|\mathbf{q}|$, the beam direction differs from the direction which determines the eikonal S-matrix. To reconcile the polarization axis and the eikonal approximation, one needs to rotate the target wave function from the quantization axis of the polarization $\mathbf{S}_A$ to the system with z-axis along $\mathbf{q}$, namely

$$\langle \theta, \phi | \Psi_{^3He} \rangle_{\hat{\mathbf{S}}_A} = \langle \theta', \phi' | D(0, \alpha, 0) | \Psi_{^3He} \rangle_{\hat{\mathbf{q}}} = \\ = \cos(\alpha/2) \, \langle \theta', \phi' | \Psi_{^3He}^{\mathcal{M}=1/2} \rangle_{\hat{\mathbf{q}}} + \sin(\alpha/2) \, \langle \theta', \phi' | \Psi_{^3He}^{\mathcal{M}=-1/2} \rangle_{\hat{\mathbf{q}}} \tag{4.44}$$

where the subscript indicate the direction of the z-axis with $\cos\alpha = \hat{\mathbf{S}}_A \cdot \hat{\mathbf{q}}$. In this case, the tensor $W^{s.i.}_{\mu\nu}(S_A, Q^2, P_h)$ in Eq. (4.8) is modified and reads as

$$W^{s.i.}_{\mu\nu}(S_A, Q^2, P_h) = \\ \cos^2(\alpha/2) \, W_{\mu\nu}^{\frac{1}{2}\frac{1}{2}} + \sin^2(\alpha/2) W_{\mu\nu}^{-\frac{1}{2}-\frac{1}{2}} + \sin\alpha \, \left[\frac{1}{2} \left(W_{\mu\nu}^{\frac{1}{2}-\frac{1}{2}} + W_{\mu\nu}^{-\frac{1}{2}\frac{1}{2}} \right) \right] \tag{4.45}$$

where $W_{\mu\nu}^{\mathcal{M}\mathcal{M}'}$ are defined with respect to the new axis, i.e. parallel to $\mathbf{q}$. Then, introducing the following overlaps with quantization axis $\hat{\mathbf{q}}$

$$\mathcal{O}_{\lambda\lambda'}^{\mathcal{M}\mathcal{M}'(FSI)}(\mathbf{P_D}, E_{2bbu}) = \\ \left\langle \hat{S}_{Gl}(1,2,3) \left\{ \Psi_{\mathbf{P}_D}, \lambda, \mathbf{p}_N \right\} | \Psi_A^{\mathcal{M}} \right\rangle_{\hat{\mathbf{q}}} \, \left\langle \Psi_A^{\mathcal{M}'} | \hat{S}_{Gl}(1,2,3) \left\{ \Psi_{\mathbf{P}_D}, \lambda', \mathbf{p}_N \right\} \right\rangle_{\hat{\mathbf{q}}} \tag{4.46}$$

and making use of their property under complex conjugation, namely

$$\mathcal{O}_{\lambda\lambda'}^{\mathcal{M}\mathcal{M}'}(\mathbf{P}_{A-1}, E) = (-1)^{\mathcal{M}+\mathcal{M}'+\lambda+\lambda'} \left(\mathcal{O}_{-\lambda-\lambda'}^{-\mathcal{M}-\mathcal{M}'}(\mathbf{P}_{A-1}, E) \right)^* \,, \tag{4.47}$$

it can be shown that the contribution to the distorted spin-dependent spectral function due to the target polarization takes the form

$$\boldsymbol{\mathcal{P}}_{(FSI)}^{\hat{\mathbf{S}}_A} = \cos\alpha \boldsymbol{\mathcal{P}}_{(FSI)}^{\frac{1}{2}\frac{1}{2}} + \sin\alpha \boldsymbol{\mathcal{P}}_{(FSI)}^{\frac{1}{2}-\frac{1}{2}} \,. \tag{4.48}$$

where $\boldsymbol{\mathcal{P}}_{(FSI)}^{\mathcal{M}\mathcal{M}'}$ are evaluated with quantization axis $\hat{\mathbf{q}}$ and the relations $\boldsymbol{\mathcal{P}}_{(FSI)}^{-\frac{1}{2}-\frac{1}{2}} = -\boldsymbol{\mathcal{P}}_{(FSI)}^{\frac{1}{2}\frac{1}{2}}$ and $\boldsymbol{\mathcal{P}}_{(FSI)}^{-\frac{1}{2}\frac{1}{2}} = \boldsymbol{\mathcal{P}}_{(FSI)}^{\frac{1}{2}-\frac{1}{2}}$ have been exploited (see Ref. [65]). As it happens in PWIA, $\boldsymbol{\mathcal{P}}_{(FSI)}^{\mathcal{M}\mathcal{M}'}$ can be can be decomposed as follows

$$\boldsymbol{\mathcal{P}}_{(FSI)}^{\mathcal{M}\mathcal{M}'} = \mathcal{P}_{||(FSI)}^{\mathcal{M}\mathcal{M}'} \, \mathbf{e}_0 + \mathcal{P}_{1\perp(FSI)}^{\mathcal{M}\mathcal{M}'} \, \mathbf{e}_+ + \mathcal{P}_{2\perp(FSI)}^{\mathcal{M}\mathcal{M}'} \, \mathbf{e}_- \,, \tag{4.49}$$

where $\mathcal{P}_{||(\perp)}^{\mathcal{M}\mathcal{M}}$ are defined in full analogy with Eq. (4.33), while $\mathcal{P}_{||(\perp)}^{\mathcal{M}-\mathcal{M}}$ are given by

$$\mathcal{P}_{||(FSI)}^{\frac{1}{2}-\frac{1}{2}} = \frac{1}{2} \left[\mathcal{O}_{\frac{1}{2}\frac{1}{2}}^{\frac{1}{2}-\frac{1}{2}(FSI)} - \mathcal{O}_{-\frac{1}{2}-\frac{1}{2}}^{\frac{1}{2}-\frac{1}{2}(FSI)} + c.c. \right] \,, \\ \mathcal{P}_{1\perp(FSI)}^{\frac{1}{2}-\frac{1}{2}} = -\frac{1}{\sqrt{2}} \left[\mathcal{O}_{\frac{1}{2}-\frac{1}{2}}^{\frac{1}{2}-\frac{1}{2}(FSI)} + \mathcal{O}^{*\,\frac{1}{2}-\frac{1}{2}(FSI)}_{-\frac{1}{2}\frac{1}{2}} \right] \,, \\ \mathcal{P}_{2\perp(FSI)}^{\frac{1}{2}-\frac{1}{2}} = \frac{1}{\sqrt{2}} \left[\mathcal{O}_{-\frac{1}{2}\frac{1}{2}}^{\frac{1}{2}-\frac{1}{2}(FSI)} + \mathcal{O}^{*\,\frac{1}{2}-\frac{1}{2}(FSI)}_{\frac{1}{2}-\frac{1}{2}} \right] \,, \tag{4.50}$$

In what follows, for the sake of brevity the diagonal components will be indicated by only one projection, i.e. $\mathcal{P}^{\mathcal{M}\mathcal{M}}(\mathcal{O}^{\mathcal{M}\mathcal{M}}) \to \mathcal{P}^{\mathcal{M}}(\mathcal{O}^{\mathcal{M}})$.

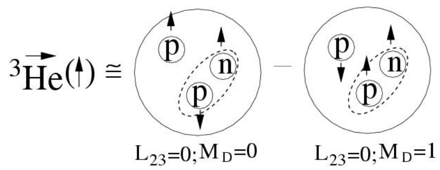

Figure 4.3: In a polarized ^{3}He, the total spin of the proton pair is basically zero, so that the neutron spin is mainly directed along the target polarization. The proton-neutron spectator pair "23" forms (preferentially) the deuteron with $L_{23} \sim 0$ in the final state. For an easy representation, the contribution of the D-state is not depicted.

4.3 Numerical results and spectral function properties

In this section, numerical calculations of the distorted spin-dependent spectral function in the 2bbu channel (that represent part of the work carried out for this thesis) are presented. Particular attention is paid to two typical kinematics, known as parallel ($\hat{\mathbf{p}}_N \parallel \hat{z}$, with $\hat{z} \equiv \hat{\mathbf{q}}$) and perpendicular ($\hat{\mathbf{p}}_N \perp \hat{z}$) kinematics. In the unpolarized case, the spectral function within these two kinematics is influenced by rather different physical effects. Namely, in the parallel kinematics, FSI are found to be negligibly small and, accordingly, the process is suitable for studying the DIS structure function of a bound nucleon; differently, in the perpendicular kinematics the FSI effects are predominant, so that details of the hadronization mechanism can be probed [79]. Bearing this in mind, let us consider the spectator SIDIS by a polarized target. Usually, all quantities are presented in terms of the asymptotic three-momentum of the spectator system, $\mathbf{P}_{A-1}$. Moreover, to keep the notation as close as possible to the one in the quasi elastic $A(e,e'p)$-reactions, we introduce the missing momentum $\mathbf{p}_{mis} \equiv \mathbf{P}_{A-1}$ (and in the following again $\mathbf{p}_{mis} \equiv \mathbf{P}_D$). Before going into the numerical analysis, let us have a qualitative glance at the intrinsic structure of a polarized ^{3}He nucleus (that represents our test ground). It is known that such a nucleus basically represents a "polarized neutron". As a matter of fact, in the polarized ^{3}He the spin projections of the protons almost ($\sim 90\%$) cancel each other, and the nuclear polarization is governed by that of the neutron [86] (see Fig. 4.3). This implies that, within PWIA when a deuteron acts as a spectator, the spin of the neutron in the final deuteron is expected to be directed along its initial polarization, i.e. along the polarization of the target. Correspondingly, the parallel component of the spin-dependent spectral function, $\mathcal{P}_{||}^{\frac{1}{2}} = \mathcal{O}^{\frac{1}{2}}_{\frac{1}{2}\frac{1}{2}} - \mathcal{O}^{\frac{1}{2}}_{-\frac{1}{2}-\frac{1}{2}}$, gets the main contribution from the deuteron configurations with $M_D = 0$ and $M_D = 1$. This can be easily understood considering only the deuteron S-wave in Eq. (4.42). Indeed putting $L_\rho = L_D = l_{23} = 0$, one can see that in $\mathcal{O}^{\frac{1}{2}}_{\frac{1}{2}\frac{1}{2}}$ the component with $M_D = 0$ contributes and in $\mathcal{O}^{\frac{1}{2}}_{-\frac{1}{2}-\frac{1}{2}}$ the component with $M_D = 1$ acts (cf Eq. (4.38)). Moreover, it turns out that the contributions from $M_D = 0$ (with an upward neutron polarization) and from $M_D = 1$ have relative size $1/2 : 1$, so that $\mathcal{P}_{||}^{\frac{1}{2}} \simeq -\frac{1}{2}\,\mathcal{O}^{\frac{1}{2}}_{-\frac{1}{2}-\frac{1}{2}}$ and negative. Although the presence of i) P- and D-waves in ^{3}He and ii) the D-wave in the deuteron changes the simple scenario depicted in Fig. 4.3, at low missing momenta one still expects that $\mathcal{P}_{||}^{\frac{1}{2}} \simeq -\frac{1}{2}\,\mathcal{O}^{\frac{1}{2}}_{-\frac{1}{2}-\frac{1}{2}}$.

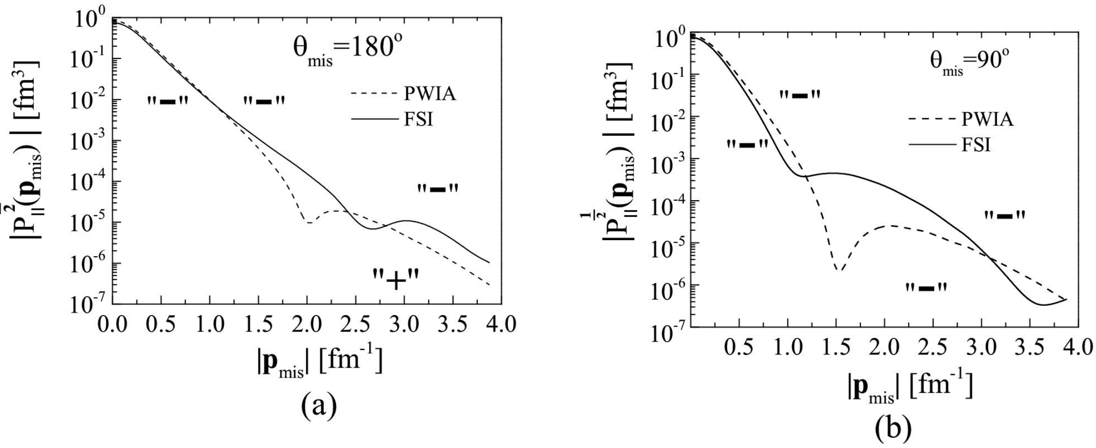

Figure 4.4: The absolute value $\left|\mathcal{P}_{||}^{\frac{1}{2}}\right|$, relevant for a spectator SiDIS with a deuteron in the final state, for the reaction $^3\vec{H}e(\vec{e}, e'\,^2H)X$, in the Bjorken limit, vs the missing momentum ($\mathbf{p}_{mis} \equiv \mathbf{P}_D$), in parallel, $\theta_{mis} = 180^o$ and $\phi_{mis} = 180^o$ (left panel), and perpendicular, $\theta_{mis} = 90^o$ and $\phi_{mis} = 180^o$ (right panel) kinematics. Dashed line: PWIA calculations. Solid line: calculations with FSI effects. The inset symbols, $+$ and $-$, indicate the sign of $\mathcal{P}_{||}^{\frac{1}{2}}$. Notice that $\mathcal{P}_{||}^{\frac{1}{2}}$ with FSI effects remains always negative, while $\mathcal{P}_{||}^{\frac{1}{2}}$ in PWIA changes sign only in parallel kinematics.

In Fig. 4.4, the absolute value of $\mathcal{P}_{||}^{\frac{1}{2}}$ (we need to use absolute value in a log scale in order to better visualize the result) is shown as a function of the missing momentum in both the parallel ($\theta_{mis} = 180^o$, $\phi_{mis} = 180^o$), and perpendicular ($\theta_{mis} = 90^o$ and $\phi_{mis} = 180^o$), kinematics. The dashed lines correspond to the PWIA case, the solid line is $\left|\mathcal{P}_{||}^{\frac{1}{2}}\right|$ with FSI effects included. As mentioned above, $\mathcal{P}_{||}^{\frac{1}{2}}$ at low missing momenta is negative within both kinematics, as indicated by the inset "minus" sign. In the parallel kinematics (left panel) at moderate values of $|\mathbf{p}_{mis}| \sim 2fm^{-1}$, $\mathcal{P}_{||}^{\frac{1}{2}}$ in PWIA vanishes and at higher $|\mathbf{p}_{mis}| > 2fm^{-1}$ becomes positive. This is an important feature of the parallel component of the spin-dependent spectral function since, as seen from Fig. 4.4, $\mathcal{P}_{||}^{\frac{1}{2}}$ with FSI effects never changes the sign, in both kinematics. This can be exploited to determine the presence (and strength) of FSI. Notice that, similarly to the unpolarized case [79], FSI are negligible at low values of $|\mathbf{p}_{mis}|$ (since in this case one has a fast final debris, given $\mathbf{p}_X \sim \mathbf{q}$) while the FSI contribution becomes sizable for $|\mathbf{p}_{mis}| \geq 1fm^{-1}$, where the equal sign holds for the perpendicular kinematics (right panel). Furthermore, because of the non trivial angular dependence in $\mathcal{P}_{||}^{\frac{1}{2}}$ (cf Fig. 4.5), though in PWIA there be a zero at $|\mathbf{p}_{mis}| \sim 2fm^{-1}$ in parallel kinematics and a minimum at $|\mathbf{p}_{mis}| \sim 1.5fm^{-1}$ in perpendicular kinematics, the magnitude of FSI effects is much larger in this last setting. (cf. Fig. 4 of Ref. [79]).

In Fig. 4.5 we present the angular dependence of $\mathcal{P}_{||}^{\frac{1}{2}}(\mathbf{p}_{mis})$ for fixed values of the missing momentum: $|\mathbf{p}_{mis}| = 1fm^{-1}$ (left panel) and $|\mathbf{p}_{mis}| = 1.8fm^{-1}$ (right panel). The choice $|\mathbf{p}_{mis}| = 1fm^{-1}$ has been inspired by the fact that, as seen from Fig. 4.4, FSI effects are still negligibly small (at least in the parallel kinematics), whereas $|\mathbf{p}_{mis}| = 1.8fm^{-1}$ corresponds to the

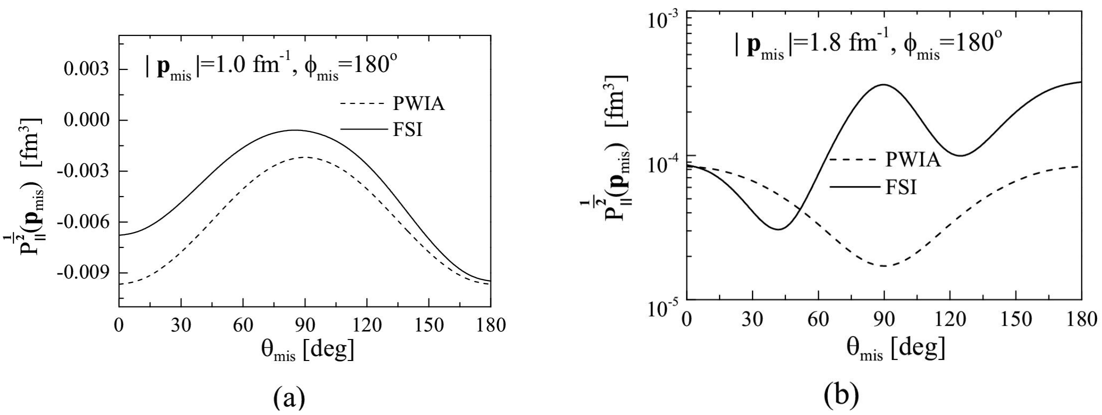

Figure 4.5: The angular dependence of $\mathcal{P}_{||}^{\frac{1}{2}}$, for two values of the missing momentum. Dashed lines correspond to the PWIA calculations. Solid lines include FSI effects.

region where the PWIA spectral function has a minimum, hence the FSI effects are maximized. It can be seen that, at lower missing momenta, FSI effects are small and in the backward hemisphere they can be safely neglected; at $|\mathbf{p}_{mis}| = 1.8 fm^{-1}$ the effects of FSI are considerable, even predominant, in the whole range of the missing angle. It is worth noting that Figs. 4.4 and 4.5 can offer hints for choosing the kinematics for both spectator and standard SIDIS, in order to minimize or maximize FSI effects. Let us remind that for the spectator SIDIS, in the first case one can address the structure functions of bound nucleons, and in the second kinematics the hadronization mechanism can be probed (see below). As we will see in the next Chapter the standard SIDIS is experimentally achieved by tagging at least one high momentum meson, and this is exactly the condition of low $|\mathbf{p}_{mis}|$ in the spectator SIDIS.

Let us now briefly discuss the perpendicular components of the spin-dependent spectral function, see Eqs. (4.32),(4.33) and (4.50). In the Bjorken limit, when $\hat{\mathbf{q}}$ becomes parallel to the z-axis, that in our analysis is also the target polarization axis, i.e. $\hat{z}||\mathbf{S}_A$, one can clearly see from Eq. (4.34) that $\mathcal{P}_{\perp}^{\hat{\mathbf{S}}_A}$ in PWIA is exactly zero within both the parallel (i.e. $\hat{\mathbf{p}}_N||\mathbf{S}_A$) and perpendicular (i.e. $\hat{\mathbf{p}}_N \perp \mathbf{S}_A$) kinematics, (recall that only the term $\hat{\mathbf{p}}_N\,(\hat{\mathbf{p}}_N \cdot \mathbf{S}_A)\,B_2(|\mathbf{p}_N|, E)$ can contribute to the perpendicular component of the spectral function, since the term proportional to $\mathbf{S}_A B_1(|\mathbf{p}_N|, E)$ can contribute only to the parallel one). [9]. But in presence of FSI, the spectral function depends also upon the vector $\mathbf{q}$ (cf below Eq. (4.40)), so that in Eq. (4.34) terms proportional to $\mathbf{q}$ must be included. In particular, a term like $\sim \hat{\mathbf{p}}_N\,(\mathbf{q} \cdot \mathbf{S}_A)$ will contribute in the perpendicular kinematics, causing $\mathcal{P}_{\perp}^{\hat{\mathbf{S}}_A}$ to be different from zero. Therefore a nonzero value of $\mathcal{P}_{1(2)\perp}^{\hat{\mathbf{S}}_A}$, in the perpendicular kinematics, undoubtedly points to FSI effects. Such a qualitative result can be obtained in a more rigorous way by closely inspecting Eq. (4.35), and investigating the dependence upon both ϕ_{mis} and θ_{mis}. It can be seen that the dependence upon ϕ_{mis} is determined by $M_\rho - \tilde{M}_\rho = \lambda' - \lambda$. This means that the parallel spectral function does not depend at all upon ϕ_{mis},

[9] One should not confuse the perpendicular and parallel kinematics, which refer to the direction of nucleon momentum $\mathbf{p}_N$ with the parallel and perpendicular components of the spectral function, which refer to the direction of the vector $\boldsymbol{\mathcal{P}}^{\hat{\mathbf{S}}_A}$

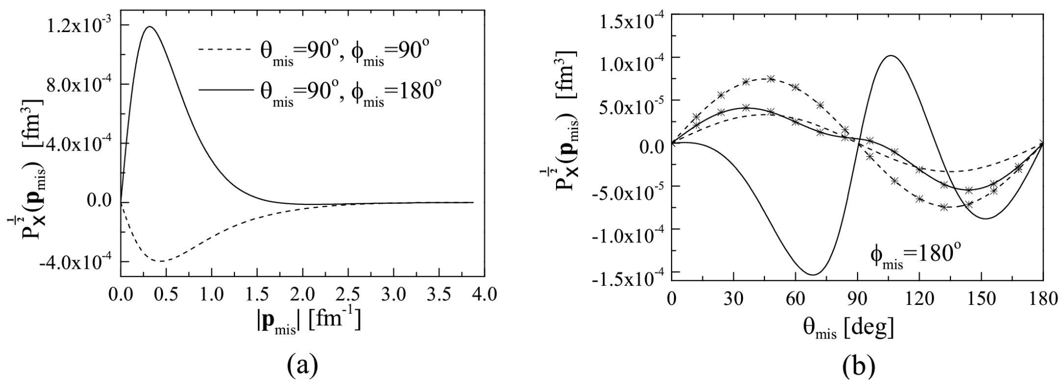

Figure 4.6: The x-component of the spin-dependent spectral function, relevant for a spectator SiDIS with a deuteron in the final state. Left panel: $\mathcal{P}_x^{\frac{1}{2}}(\mathbf{p}_{mis})$ vs $|\mathbf{p}|_{mis}$, in perpendicular kinematics, $\theta_{mis} = 90^o$, for two values of ϕ_{mis}, 180^o (solid line) and 90^o (dashed line). Within such a kinematics the PWIA spectral function is exactly zero, so that the $\mathcal{P}_x^{\frac{1}{2}}(\mathbf{p}_{mis})$ is entirely due to the FSI effects. Right panel: angular dependence of $\mathcal{P}_x^{\frac{1}{2}}(\mathbf{p}_{mis})$ for two values of the missing momentum, $|\mathbf{p}_{mis}| = 0.5 fm^{-1}$ (crossed lines) and $|\mathbf{p}_{mis}| = 1.8 fm^{-1}$. Dashed lines: PWIA. Solid lines: FSI effects are taken into account. Notice that, for a convenient presentation, the results corresponding to $|\mathbf{p}_{mis}| = 0.5 fm^{-1}$ have been rescaled by a factor $2 \cdot 10^{-2}$.

while the ϕ_{mis} dependence of the perpendicular spectral function will be $\mathcal{P}^{\hat{\mathbf{S}}_A}_{1(2)\perp} \sim \exp(\pm i\phi_{mis})$. Moreover, the presence of the term $\sim \mathrm{Y}_{L_\rho M_\rho}(\hat{\mathbf{p}}_N)\mathrm{Y}^*{}_{\tilde{L}_\rho \tilde{M}_\rho}(\hat{\mathbf{p}}_N)$ demonstrates that $\mathcal{P}^{\hat{\mathbf{S}}_A}_{1(2)\perp}$ identically vanish at $\theta_{mis} = 0,\ \pi/2,\ \pi$ in PWIA, since $M_\rho - \tilde{M}_\rho = \pm 1$. As well-known, the two spherical harmonics can be expanded on terms like $\langle L_\rho M_\rho \tilde{L}_\rho - \tilde{M}_\rho | \mathcal{L} \pm 1\rangle \mathrm{Y}_{\mathcal{L}\pm 1}(\hat{\mathbf{p}}_N)$ that vanish for $\theta_{mis} = 0,\ \pi$. For $\theta_{mis} = \pi/2$ the argument is less direct. The two spherical harmonics are different from zero only if $\tilde{L}_\rho + \tilde{M}_\rho$ and $L_\rho + M_\rho$ are both even, but $\tilde{L}_\rho + L_\rho$ is even and $\tilde{M}_\rho + M_\rho$ is odd. When the FSI effects are taken in to account, the previous product is replaced with $\int d\rho_\perp .... J_\mathcal{M}(|\mathbf{p}_{mis\perp}|\rho_\perp) \cdot \int d\tilde{\rho}_\perp .... J_{\mathcal{M}'}(|\mathbf{p}_{mis\perp}|\tilde{\rho}_\perp)$, where $J_{\mathcal{M}(\mathcal{M}')}$ are the cylindrical Bessel functions and one has still $\mathcal{M} - \mathcal{M}' = \pm 1$. It is clear that, in the parallel kinematics (i.e. $\mathbf{p}_{mis\perp} = 0$), at most only one Bessel function cannot vanish ($J_\mathcal{M}(0) \neq 0$ only for $\mathcal{M} = 0$) and therefore $\mathcal{P}^{\hat{\mathbf{S}}_A}_\perp$ is zero even in presence of FSI for $\mathbf{p}_{mis\perp} = 0$.

One should notice that for the spherical components one has $\mathcal{P}^{\hat{\mathbf{S}}_A}_{1\perp} = \left[\mathcal{P}^{\hat{\mathbf{S}}_A}_{2\perp}\right]^*$, see Eq. (4.32), but for numerical analysis it is more convenient to deal with real quantities, e.g. with the Cartesian components $\mathcal{P}^{\hat{\mathbf{S}}_A}_x$ and $\mathcal{P}^{\hat{\mathbf{S}}_A}_y$, see Eq. (4.33). Since $\mathcal{P}^{\hat{\mathbf{S}}_A}_y(\phi_{mis}) = -\mathcal{P}^{\hat{\mathbf{S}}_A}_x(\pi/2 + \phi_{mis})$, it is sufficient to analyze only one component, say $\mathcal{P}^{\hat{\mathbf{S}}_A}_x$. In the left panel of Fig. 4.6, the Bjorken limit of $\mathcal{P}_x^{\frac{1}{2}}(\phi_{mis})$ is shown as a function of $|\mathbf{p}_{mis}|$, in the perpendicular kinematics and two values of ϕ_{mis}. It can be seen that $\mathcal{P}_x^{\frac{1}{2}}$, in comparison with $\mathcal{P}_{||}^{\frac{1}{2}}$ (Fig. 6), is negligibly small, and in the perpendicular kinematics is entirely governed by FSI. In the right panel of Fig. 4.6, the angular dependence of $\mathcal{P}_x^{\frac{1}{2}}$, both without and with FSI effects, is presented for two values of missing momentum. As already mentioned, the PWIA calculations vanish at $\theta_{mis} = 0,\ \pi/2,\ \pi$. Moreover, it is seen that the x-component is much smaller then the parallel $\mathcal{P}_{||}^{\frac{1}{2}}$ in the whole range of θ_{mis}. Finally, from Fig. 4.6, one could get the impression that, at $\theta_{mis} = 90^o$ the x-component of the spin-dependent spectral functions vanishes both without and with FSI effects. This is because of the adopted linear scale of the figure. Actually, while in PWIA $\mathcal{P}_x^{\frac{1}{2}}$ is exactly zero, the calculations with FSI show that $\mathcal{P}_x^{\frac{1}{2}}(\theta_{mis} = 90^o) \sim 10^{-3}$.

The results we have shown are preparatory to better understand how and if the FSI play sizable role in the extraction of the neutron SSA. To summarize, we introduced a novel nuclear distribution function for investigating the semi inclusive deep-inelastic scattering of polarized leptons by a polarized $A = 3$ nucleus. Such a spin-dependent spectral function has been evaluated by using the three body wave function [55] corresponding to a realistic AV18 NN interaction [78]. Our calculation should make more reliable the extraction information on a bond nucleon, with an aim of providing a refined treatment of a polarized ^{3}He target, that represents an effective neutron target and plays a fundamental role for obtaining neutron single spin asymmetries and consequently observables like transitivity, and Sivers functions, i.e. the main physical motivations of forthcoming experiments with a transversely polarized ^{3}He target [58].

A quick look on the extraction method used until now [57] will be presented in the next Chapter.

Chapter 5

The neutron single spin asymmetries by a polarized ^{3}He target

In this Chapter, the distorted spectral function formalism, previously described, will be applied for a first evaluation of the effects of the FSI in the extraction procedure nowadays used [47] in order to get the neutron SSAs from the one measured on a polarized ^{3}He target. Then, a relativistic extension of the description of the spectral function in PWIA will be presented, with the first results of the relativistic corrections on the effective polarizations of the nucleon in the ^{3}He nucleus. The corresponding results, have been also illustrated in Ref.[87, 88, 90, 91, 89].

5.1 Polarized ^{3}He nucleus and neutron properties

A polarized ^{3}He nucleus at a 90% level is equivalent to a polarized neutron: in a polarized ^{3}He, the total spin of the proton pair is basically zero, so that the neutron spin is mainly directed along the target polarization. Let us remind that the ground state wave function of ^{3}He consist of the superposition of S(88.2%), S'(1.4%) and D(9.8%) states. In PWIA, to disentangle the nucleon structure from the dynamical nuclear effects, one can use the spin-dependent spectral function of 4.34, (see, e.g. [63]) that allows one to calculate the probability distribution to find a nucleon with given missing energy, three-momentum and polarization inside the nucleus. With this formalism, one can safely extract [62] the neutron longitudinal asymmetry from the corresponding ^{3}He observable, A_3^{exp}, obtained from the reaction $^3\vec{\mathrm{He}}(\vec{e}, e')X$ in DIS regime, viz

$$A_n \simeq \left(A_3^{exp} - 2p_p f_p A_p^{exp}\right) / (p_n f_n) \,, \tag{5.1}$$

where $p_{n(p)}$ is the neutron (proton) effective polarization inside the polarized ^{3}He, and $f_{p(n)}(x, z) = \sum_q e_q^2 f_1^{q,p(n)}(x)\, D_1^{q,h}(z) \,/\, \sum_{N=p,n} \sum_q e_q^2 f_1^{q,N}(x) D_1^{q,h}(z)$, the dilution factor.
Realistic values of p_n and p_p are: $p_p = -0.023$, $p_n = 0.878$ (see, e.g., [62, 57]). In [57], an analogous approach was applied to the SSAs of a transversely polarized $^3\vec{\mathrm{He}}$ target (namely Collins and Sivers asymmetries), obtained from the process $^3\vec{\mathrm{He}}(e, e'\pi)X$, in order to extract the SSAs of a transversely polarized neutron. In PWIA and in the Bjorken limit, the SSAs of $^3\vec{\mathrm{He}}$ are a con-

volution of $\mathcal{O}^{\hat{\mathbf{S}}_A}_{\lambda'\lambda}(\mathbf{p}_N, E)$, and the nucleon SSAs, that in turn are convolutions of suitable TMDs and fragmentation functions, that describe the hadronization of the hit quark. This approach has been used in combination with a Monte Carlo code reproducing the experimental conditions and the proper kinematics of [58]: a MC C++ program that simulates the detector responses (in a box like way) to generate the phase space and the particle rates of experiment described in Chapter 3. In some details, the MC calculates all the kinematical relevant variables fulfilling all the 4-momenta conservation and calculates cross sections (for the DIS and SIDIS polarized and unpolarized cases) and rates, for the considered kinematical range and for a specific detected hadron, using the available models and parametrization of distribution functions and fragmentation functions. (for more details on the MC see the first of [58]). In Fig.5.1 the nuclear structure effects, based on the previous assumptions are illustrated for a particular choice of the relevant experimental kinematical variables.

The phase space of the scattered electrons and the produced hadrons is used as input for the asymmetry extraction. Together with the free neutron asymmetries for both Collins and Sivers cases. A calculation gives the following quantities

$$\bar{A}^i_n \simeq \frac{1}{f_n} A_3^{exp,i} \,, \tag{5.2}$$

where $A_3^{exp,i}$ is the result of the full calculation described in [57] and simulating data; f_n is the neutron dilution factor. Equation (5.2) represents the ideal case in which ^{3}He is a system of free nucleons in a pure S wave. Clearly, it can be obtained from Eq. (5.1) by imposing $p_n = 1$ and $p_p = 0$. The second calculation is obtained from Eq.(5.1). From this result we learn that it is not sufficient to describe the ^{3}He system as a nucleus pure S wave state and that, neglecting FSI and relativistic effects a relative systematic error not greater than 7% is expected. But, reminding that due to high luminosity the expected statistical error in the future experiments will be order a percent, a further investigation of the neglected effects should be addressed.

5.2 The distorted spin-dependent spectral function and the neutron SSAs extraction

In order to carefully investigate the validity of the extraction method previously outlined, one has to release some of the assumptions which has been proven to be reasonable in the case of DIS (namely, in the nowadays adopted neutron single spin asymmetry extraction scheme FSI has been disregarded, but it is not obvious that nuclear FSI effects are negligible in SIDIS processes). Mostly the FSIs play a big role in the transverse TMDs, therefore it is crucial to carefully disentangle the contribution of the nucleonic FSI from that which can be eventually came from the nuclear FSI interaction, which in PWIA is assumed negligible small.
The key quantity to introduce the FSI effects is the distorted spin-dependent spectral function, whose relevant part in the evaluation of SSAs is:

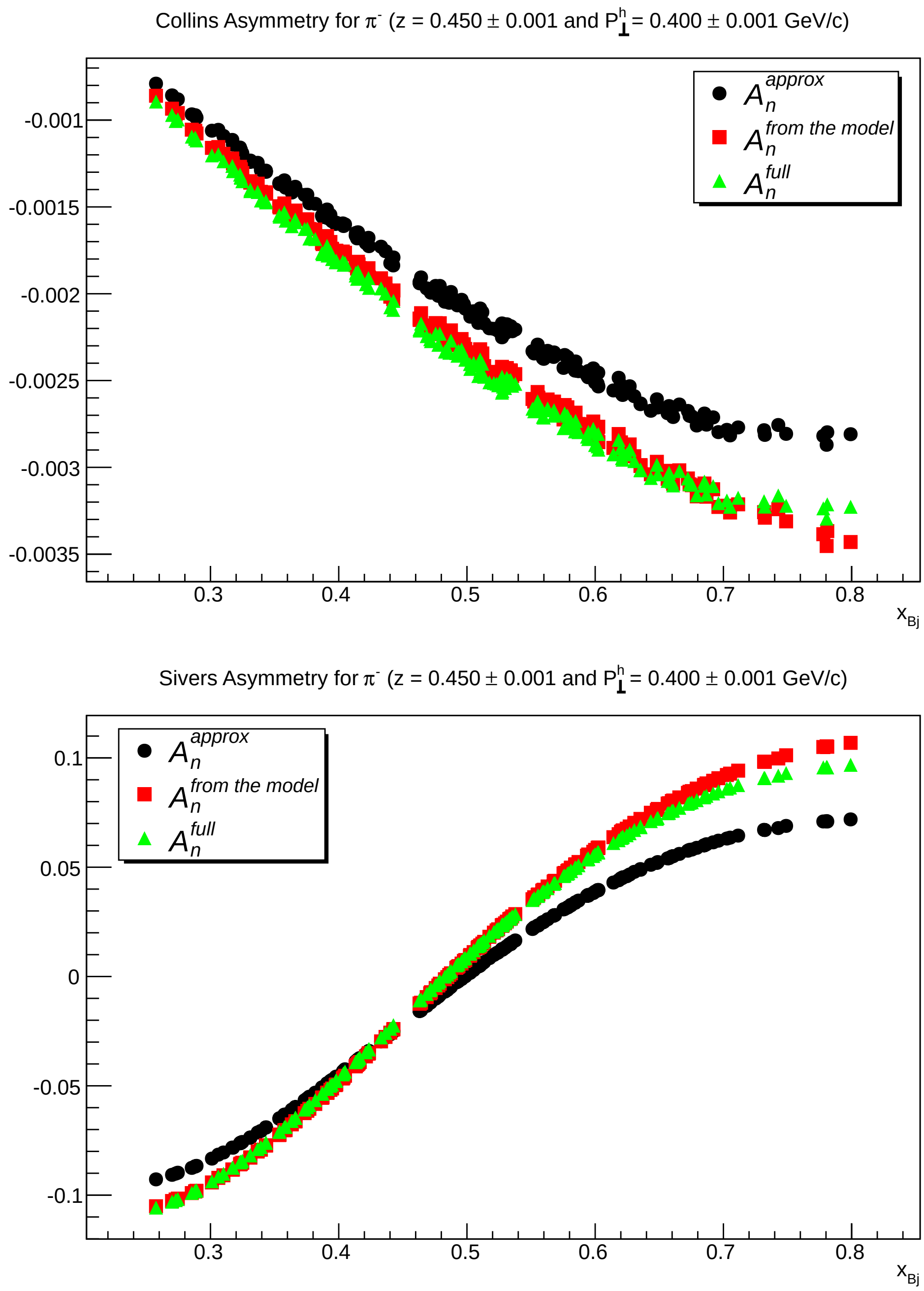

Figure 5.1: The neutron Collins (upper panel) and Sivers (lower panel) SSAs for the production of π^- vs x_{Bj}, for $z = 0.450 \pm 0.001$ and $P_\perp^h = 0.400\ GeV/c$, with electron beam energy of 11 GeV. Red squares: neutron input model A_n [57]. Green triangles: A_n^{full} extracted from Eq. (5.1). Black dots: $A_n^{approx} \simeq \frac{1}{f_n} A_3^{exp,i}$.

$$\mathcal{P}_{||}^{PWIA(FSI)} = \mathcal{O}^{IA(FSI)}_{\frac{1}{2}\frac{1}{2}} - \mathcal{O}^{IA(FSI)}_{-\frac{1}{2}-\frac{1}{2}} \tag{5.3}$$

with:

$$\mathcal{O}^{IA}_{\lambda\lambda'}(\vec{p},E) = \sum\!\!\!\!\!\!\!\int d\epsilon^*_{A-1}\, \rho\left(\epsilon^*_{A-1}\right)\, \langle S_A, \mathbf{P}_A|\Phi_{\epsilon^*_{A-1}}, \lambda', \vec{p}\rangle \times$$
$$\langle \Phi_{\epsilon^*_{A-1}}, \lambda, \vec{p}|S_A, \mathbf{P}_A\rangle\, \delta\left(E - B_A - \epsilon^*_{A-1}\right)\ , \tag{5.4}$$

when the PWIA framework is adopted and

$$\mathcal{O}^{FSI}_{\lambda\lambda'}(\vec{p},E) = \sum\!\!\!\!\!\!\!\int d\epsilon^*_{A-1}\, \rho\left(\epsilon^*_{A-1}\right)\, \langle S_A, \mathbf{P}_A|(\hat{S}_{Gl})\{\Phi_{\epsilon^*_{A-1}}, \lambda', \vec{p}\}\rangle \times$$
$$\langle (\hat{S}_{Gl})\{\Phi_{\epsilon^*_{A-1}}, \lambda, \vec{p}\}|S_A, \mathbf{P}_A\rangle\, \delta\left(E - B_A - \epsilon^*_{A-1}\right)\ , \tag{5.5}$$

when the FSI effects are taken into account as illustrated in the previous Chapter (cf the overlap functions in Eq. (4.9)). Let us recall that in the non relativistic limit $\mathcal{P}_{||}^{\hat{S}_A\equiv\hat{z}} = \mathcal{P}_{\perp}^{\hat{S}_A\equiv\hat{y}}$, therefore neglecting relativistic effects, the SF entering in the case of longitudinal and transverse polarization of the target (with respect to the virtual photon direction $\hat{q}\equiv\hat{z}$) are the same.
Let us recall that in Eqs. (5.4) and (5.5) $\rho\left(\epsilon^*_{A-1}\right)$ is the proper density of the $(A-1)$-system states (which in this case it is not the deuteron) with intrinsic energy ϵ^*_{A-1} (namely, (4.5)), and $|S_A, \mathbf{P}_A\rangle$ is the ground state of the A-nucleons nucleus with polarization S_A, and quantity $\hat{S}_{Gl}$ is the Glauber operator (4.40).
It occurs that $\mathcal{P}_{||}^{PWIA}$ and $\mathcal{P}_{||}^{FSI}$ can be very different, but the relevant observables for the SSAs involve integrals, dominated by the low momentum region, where the FSI effects on $\mathcal{P}_{||}$ are minimized and the spectral function is large [79]. As a consequence the effective nucleon polarizations that enter the factorized expression in Eq. (5.1) change from $p_p = -0.023$, $p_n = 0.878$ to new quantities that we evaluated to amount to $p_p^{FSI} = -0.027$, $p_n^{FSI} = 0.756$, this values have been calculated from

$$p^{FSI}_{p(n)} = \int d\epsilon_S \int d\mathbf{p}\; Tr[\mathbf{S}_{He}\cdot\sigma\; P^{p(n)}_{FSI}(\vec{p},E,S_{He})]\ , \tag{5.6}$$

with $P^{p(n)}_{FSI}(\vec{p},E,S_{He})$ the distorted spin-dependent spectral function, defined in terms of the overlaps of Eq. (5.5) [87]. Then $p_{p(n)}$ with and without the FSI differ by 10-15% . As to the SSAs extraction, one has to consider the effects of the FSI also in the dilution factor

$$f^{FSI}_{n,(p)}(x,z) = \frac{\sum_q e_q^2 f_1^{q,n(p)}(x) D_1^{q,h}(z)}{\langle N_n\rangle_{FSI}\sum_q\; e_q^2 f_1^{q,n}(x) D_1^{q,h}(z) + 2\langle N_p\rangle_{FSI}\sum_q\; e_q^2 f_1^{q,p}(x) D_1^{q,h}(z)}. \tag{5.7}$$

with $\langle N_{n,(p)}\rangle_{FSI} = \int d\epsilon_S \int d\tilde{\mathbf{k}}\; Tr[\mathcal{P}^{p(n)}_{FSI}(\tilde{\mathbf{k}},\epsilon_S,S_{He})]/2$ ($\langle N_{n,(p)}\rangle_{FSI}$ should be considered an effective number and could be less than one), $f_1^{q,n(p)}(x)$ the partonic unpolarized distribution

Table 5.1: Preliminary results on the effect of FSI on the products $p_n f_n$ and $p_p f_p$ in a relevant kinematics for the planned Hall A experiment described in Chapter 3. The upper Table shows the results for the case of PWIA, the lover one shows the results for the case in which FSI is considered.

1) PWIA: p_n= 0.878, p_p= -0.023, $\theta_e = 30^o$, $\theta_\pi = 14^o$, $z = 0.45$

E_{beam}, GeV	x_{Bj}	ν GeV	p_π GeV/c	$f_n(x,z)$	$p_n\ f_n$	$f_p(x,z)$	$p_p\ f_p$
8.8	0.21	7.55	3.40	0.304	0.266	0.348	-8.4$10^{-3}$
8.8	0.29	7.15	3.19	0.286	0.251	0.357	-8.5$10^{-3}$
8.8	0.48	6.36	2.77	0.257	0.225	0.372	-8.9$10^{-3}$
11	0.21	9.68	4.29	0.302	0.265	0.349	-8.3$10^{-3}$
11	0.29	9.28	4.11	0.285	0.250	0.357	-8.5$10^{-3}$

2) FSI: p_n= 0.756, p_p= -0.027, $\langle\sigma_{eff}\rangle = 71\ mb$, $z = 0.45$

E_{beam}, GeV	x_{Bj}	ν GeV	p_π GeV/c	$f_n(x,z)$	$p_n\ f_n$	$f_p(x,z)$	$p_p\ f_p$
8.8	0.21	7.55	3.40	0.353	0.267	0.405	-1.1$10^{-2}$
8.8	0.29	7.15	3.19	0.332	0.251	0.415	-1.1$10^{-2}$
8.8	0.48	6.36	2.77	0.298	0.225	0.432	-1.2$10^{-2}$
11	0.21	9.68	4.29	0.351	0.266	0.405	-1.10$0^{-2}$
11	0.29	9.28	4.11	0.331	0.250	0.415	-1.1$10^{-2}$

function and $D_1^{q,h}(z)$ the unpolarized fragmentation function [57].

As shown in Tab. 5.1, FSI can sizably modify the overlaps given in Eq. (4.9), with respect to the PWIA values. But, even if there is a rather sizable change of the net polarization and of the dilution factors in Eq. (5.1) due to the presence of FSI, fortunately their product ($p_n f_n$ and $p_p f_p$) does not (see Tab. 5.1). Therefore the extraction procedure, appear to be safe:

$$A_n \simeq \frac{1}{p_n^{FSI} f_n^{FSI}} \left(A_3^{exp} - 2p_p^{FSI} f_p^{FSI} A_p^{exp}\right) \simeq \frac{1}{p_n f_n} \left(A_3^{exp} - 2p_p f_p\ A_p^{exp}\right) \tag{5.8}$$

5.3 Relativistic description of the spectral function

In the phenomenological framework adopted in [57] and also in Fig. 5.1, the calculation are performed using a non relativistic approach for the spectral function, but adopting the Bjorken limit for what pertains the kinematics. However, since for JLab at 12 GeV one has to deal with a drastic reduction of the statistical uncertainties, also the role played by relativity has to be investigated.
To study the effect of the relativistic corrections in the experimental kinematics of [58] the Relativistic Hamiltonian Dynamics (RHD) introduced by Dirac in Ref.[71] has been adopted in combination with the Bakamijan - Thomas construction of the Poincaré generators [73]. This approach leads to a description of a SIDIS process on ^{3}He which: i) is fully Poincaré covariant; ii) has a fixed number of on-mass-shell constituents; iii) allows one to decompose the wave function as in the non relativistic case. Among the three possible forms of RHD the *Light Front* one has been adopted due to the following advantages: i) it has seven kinematical generators: three LF boosts,

Table 5.2: Proton and neutron effective polarizations within the non relativistic appproach (NR) and preliminary results within the light-front relativistic dynamics approach (LF). First line : longitudinal effective polarizations; second line : transverse effective polarizations (errors are on the last digit).

	$proton\, NR$	$proton\, LF$	$neutron\, NR$	$neutron\, LF$
$\int\ dEd\vec{p}\ \ Tr(\mathcal{P}\sigma_z)_{\vec{S}_A=\widehat{z}}$	-0.02263	-0.02231	0.87805	0.87248
$\int\ dEd\vec{p}\ \ Tr(\mathcal{P}\sigma_y)_{\vec{S}_A=\widehat{y}}$	-0.02263	-0.02268	0.87805	0.87494

three component of the LF momentum $\tilde{\mathbf{P}} \equiv \{\mathbf{P}^+, \mathbf{P}_\perp\}$ and the rotation around the z axis; ii) the separation of the intrinsic motion from that of the center of mass is achieved as in the non relativistic case; iii) $\mathbf{P}^+ > \mathbf{0}$ leads to a meaningful Fock expansion, in presence of massive boson exchange; iv) there is no square root in the operator P^- propagating the state in the LF time; v) the IMF description of DIS or SIDIS is easily included. On the other hand the LF rotations are dynamical. The key quantity to consider in SIDIS processes is the LF relativistic spectral function, $\mathcal{P}^\tau_{\sigma'\sigma}(\tilde{\kappa}, \epsilon_S, S_{He})$, with $\tilde{\kappa}$ an intrinsic nucleon momentum and ϵ_S the energy of the two-nucleon spectator system, $\sigma'\sigma$ are the nucleon spin projections and τ the isospin of the produced pseudo-scalar meson. In PWIA the LF hadronic tensor for the ^{3}He nucleus is:

$$\mathcal{W}^{\mu\nu}(Q^2, x_B, z, \tau_{hf}, \hat{\mathbf{h}}, S_{He}) \propto \sum_{\sigma,\sigma'} \sum_{\tau_{hf}} \sum\!\!\!\!\!\!\!\int_{\epsilon_S^{min}}^{\epsilon_S^{max}} d\epsilon_S \int_{M_N^2}^{(M_X-M_S)^2} dM_f^2 \int_{\xi_{lo}}^{\xi_{up}} \frac{d\xi}{(2\pi)^3} \times$$
$$\frac{1}{\xi^2(1-\xi)} \int_{P_\perp^{min}}^{P_\perp^{max}} \frac{dP_\perp}{sin\theta} \left(P^+ + q^+ - h^+\right) w^{\mu\nu}_{\sigma\sigma'} \left(\tilde{\mathbf{q}}, \tau_{hf}, \tilde{\mathbf{h}}, \tilde{\mathbf{P}}\right) \mathcal{P}^{\tau_{hf}}_{\sigma'\sigma}(\tilde{\mathbf{k}}, \epsilon_S, S_{He})\,. \tag{5.9}$$

where $z = P_{He} \cdot h/(P_{He} \cdot q)$, $\tilde{\mathbf{q}}$ is the virtual photon momentum, $\tilde{\mathbf{h}}$ the detected pion momentum, M_f the mass of the remnant (X', see Fig.4.1), $\xi = p^+/P^+_{He}$, θ is the angle between $\mathbf{p}_\perp$ and $(\mathbf{q}_\perp - \mathbf{h}_\perp)$, $w^{\mu\nu}_{\sigma\sigma',\tau}\left(\tilde{\mathbf{q}}, \tau_h, \tilde{\mathbf{h}}, \tilde{\mathbf{p}}\right)$ the nucleon hadronic tensor, with $\tilde{\mathbf{h}}$ the LF momentum of the produced pseudo-scalar meson.

The LF nuclear spectral function is defined as

$$\mathcal{P}^\tau_{\sigma'\sigma}(\tilde{\mathbf{k}}, \epsilon_S, S_{He}) \propto \sum_{\sigma_1\sigma'_1} D^{\frac{1}{2}}[\mathcal{R}^\dagger_M(\tilde{\mathbf{k}})]_{\sigma'\sigma'_1}\ \mathcal{S}^\tau_{\sigma'_1\sigma_1}(\tilde{\mathbf{k}}, \epsilon_S, S_{He}) D^{\frac{1}{2}}[\mathcal{R}_M(\tilde{\mathbf{k}})]_{\sigma_1\sigma}\ , \tag{5.10}$$

with $D^{\frac{1}{2}}[\mathcal{R}_M(\tilde{\mathbf{k}})] = \ m + k^+ - \imath\boldsymbol{\sigma} \cdot (\hat{z} \times \mathbf{k}_\perp)/\sqrt{(m + k^+)^2 + |\mathbf{k}_\perp|^2}$ the unitary Melosh Rotations.

The instant-form spectral function (disregarding FSI) $S^\tau_{\sigma'_1\sigma_1}(\mathbf{p}, \epsilon_S, S_{He})$ [10] can be given in terms of three independent functions, B_0, B_1, B_2, where the function B_0 yields the usual unpolarized spectral function, while the B_1 and B_2 describe the spin structure of the nucleus in terms of the constituent nucleons. Following the notation used in [74], one has

$$\mathcal{S}^\tau_{\sigma'_1\sigma_1}(\tilde{\mathbf{k}}, \epsilon_S, S_{He}) = \ \left[B^\tau_{0,S_{He}}(|\mathbf{k}|, E)\ +\ \boldsymbol{\sigma} \cdot \mathbf{f}^\tau_{S_{He}}(\mathbf{k}, E)\right]_{\sigma'_1\sigma_1}\ , \tag{5.11}$$

[10] $S^\tau_{\sigma'_1\sigma_1}$ is a matrix element of a 2×2 matrix and it is equivalent, but in a different notation, to $\mathcal{O}^{\hat{\mathbf{S}}_A}_{\lambda'\lambda}(\mathbf{p}_N, E)$ defined in Eq.4.9, where $\sigma_1 \equiv \lambda$.

where

$$\mathbf{f}^{\tau}_{S_{He}}(\mathbf{k}, E) \;=\; \mathbf{S}_A \, B^{\tau}_{1,S_{He}}(|\mathbf{k}|, E) \;+\; \hat{k} \, (\hat{k} \cdot \mathbf{S}_A) \, B^{\tau}_{2,S_{He}}(|\mathbf{k}|, E) \; . \tag{5.12}$$

is the (4.34) in which $\boldsymbol{\mathcal{P}}^{\hat{\mathbf{S}}_A} \equiv \mathbf{f}^{\tau}_{S_{He}}$.
Within the above described framework, preliminary results, shown in Tab. 5.2, seem suggest that the LF longitudinal and transverse polarizations, within PWIA, weakly differ and then the extraction procedure in the Bjorken limit works in the LF framework as it does in the non relativistic one.

5.4 Comments and improvements

To summarize what we have understood from the comparisons presented in this Chapter, one can list:

i) the procedure used to extract the neutron SSAs from that of the ^{3}He seems to be still solid even if the FSI effects are included using a Glauber extended eikonal approximation (in this framework relativistic effects have been disregarded),

ii) including the relativistic effects (but disregarding FSI) does change weakly the effective polarization of the nucleons in the ^{3}He, but the procedure till now adopted seems to be reliably consistent even for the 12 GeV data, where the Bjorken limit is expected to be reasonably fulfilled.

However, let us emphasize that the statistical uncertainty in the planned measurements [58] is expected to be of the order of a percent, and therefore, to carefully evaluate the systematic uncertainties due to the nuclear effects, at least two improvements should be needed: i) the extraction procedure should be tested in combination with the Monte Carlo generator used in 5.1, (notice that the MC code has as an input the distorted spectral function, to be evaluated in a rather wide range of its variables, and this requests a sizable amount of computing resources); ii) the Generalized Eikonal Approximation framework, where FSI are presently evaluated, should be integrated in the Light-Front description of the spectral function, namely both relativistic effects and final state interaction have to be merged in the same framework.

Chapter 6

Tracks filtering and fitting algorithms in high luminosity experiments

As it has been underlined in the previous Chapters, in order to extract the neutron SSAs (and subsequently in order to obtain a sound flavor separation of the nucleon TMDs) two ingredients at least are needed at the same time: i) a strong knowledge of the ^{3}He nuclear structure, in order to set up a solid framework to extract the neutron information; ii) the possibility to work at the luminosity frontiers, in order to reduce the statistical uncertainties in a wide kinematical range. To dealing with the second issue not only a strong knowledge of the hardware tracking apparatus is needed but also a fast and efficient tracking algorithms able to associate and filter the particle hits are mandatory. A modular appoach has been developed to get rid of the tracking issues. The approach include a Monte Carlo simulation, a hit association based on Neural Network and a precise track fitting and filtering based on Kalman method; this latter part has been carried on for this thesis. Details on the definition, development and implementation of the neutral network and the integration with the kalman method has described in [92]. In order to maintain a logic chain, firstly the typical events rate expected in the planned JLab Hall A experiments will be described, the main results on track association obtained in [92] will be sketched and then the results concerning tracks filtering and fitting will be presented.

6.1 Expected event rate at JLab12 Hall A experiments

The typical expected event rate in Hall A SBS spectrometer is 20 KHz for the signal events and 400 KHz of background. In the following a GEANT4 [93] simulations of typical signal and background events are shown. In Fig.6.1 it can be seen that the charge rise of simulated signals is correlated with the trigger start, whereas the charge rise of the background it is not. It is important to recall that the GEM readouts consist of two perpendicular x/y strips planes; the timing coincidence also with the charge x/y correlation of the signals yields a first hardware method to discriminate and reduce the background. But, since the passage of a charged particle typically release a charge deposit in three adjacent strips (in both x and y), it is easy to see that, differently

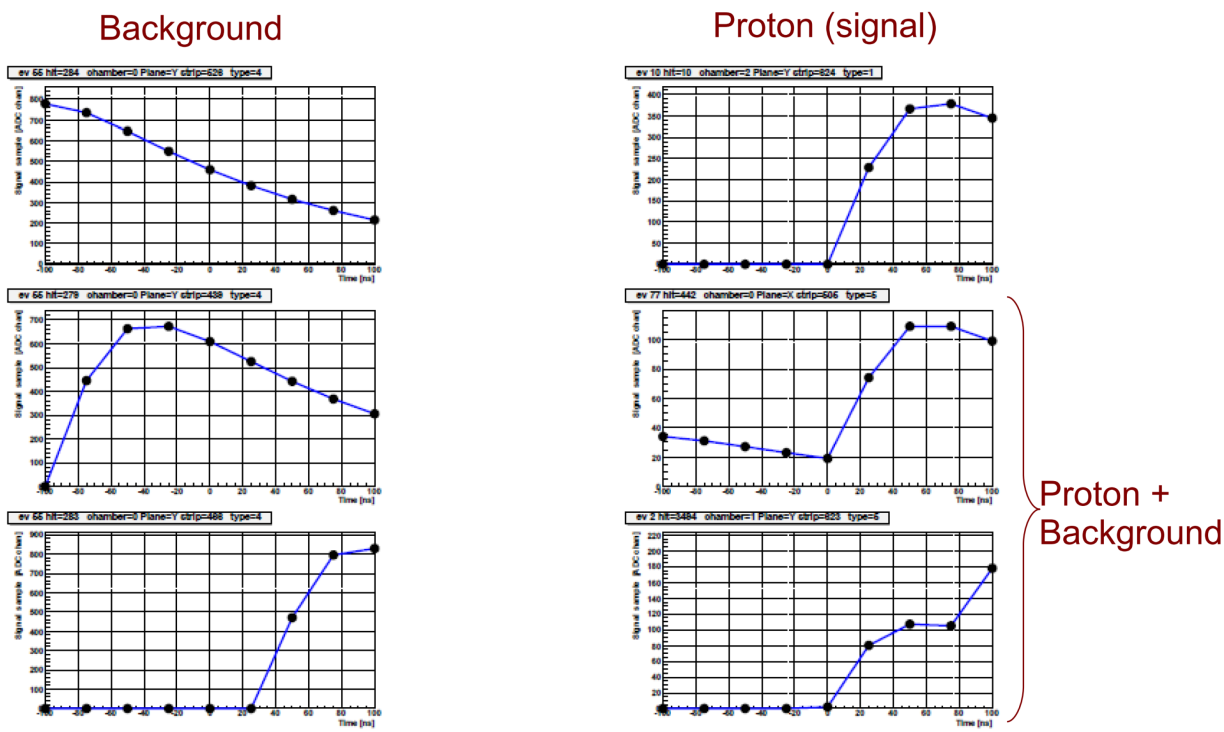

Figure 6.1: The figure shows the typical charge signal shape yields by the electronics when a particle pass through GEM chambers. In the left panel background tracks are shown, in the right panel signal (on the top) and signal plus background tracks are shown.

from a pixel readout plane, in the strip case one has a combinatorial configuration which lead to a high number of fake "ghost" hits growing with the chambers occupancy. Giving the assumed rates and assuming that half of the "ghost" hits can be eliminated using time and charge correlation informations, the typical expected occupancy, in an area of 10 cm^2, is:

i) 1 signal (hadron) track from interaction vertex,

ii) 1 charged background particle,

iii) 1 background photon per plane,

iv) about 100 ghost hits per plane.

Since the GEANT4 simulated data do not contain (for the moment) the ghost hits, this typical rate configuration has been simulated considering six 40×50 cm^2 GEM chamber with a spatial x/y resolution of $100\mu m$ and typically taking a 10 cm^2 box around the center of the first GEM plane[11]. It is important to underline that this data set contains spatial resolution effects only and

[11]Let us emphasize that the ghosts rate must be calculated considering the hits in all the GEM surface and then the 10 cm^2 surface can be selected. Doing this one obtains the above described occupancy.

not multiple scattering effects. The magnetic field in the chambers plane region is assumed to be zero. The results of this simulation have been used to test the associative neural network developed in [92], in the following the main results will be summarized for completeness.

6.2 Association of the hits with neural network

Several methods have been proposed during the time to solve the problem of particle track association, and for a complete and exhaustive review we refer to [94]. The possibility to use Hopfield-like neural networks to solve the track association problem in High Energy Physics has been firstly demonstrated in [95, 96]. In the following the results obtained using the above described hits configuration in combination with a neural network defined within the framework of Mean Field Theory (MFT) developed and implemented in [92] will be quickly outlined.
The essential feature of the neural network in MFT are the following:

i) bi-dimensional S_{ij} neurons correspond to connection between two hits (1 if connection is on, 0 if it is off),

ii) in general a particular energy function subtend the properties of the neurons and has to be minimized in order to obtain the correct associative configuration,

iii) within the MFT approximation the neurons assume continuous value V_{ij} between 0 and 1, and it is possible to have an analytic recursive equation for the network updating.

Since the neurons are bi-dimensional, they are usually connected by synaptic weights T_{ijkl}, which represent correlation between neurons. The typical general energy function form is

$$E(\vec{S}) = -\frac{1}{2}\sum_{ijkl} T_{ijkl} V_{ij} V_{kl}, \tag{6.1}$$

and the neurons recursive updating equation is

$$V_{ij} = \frac{1}{2}\left[1 + \tanh\left(-\frac{\partial E}{\partial V_{ij}}\frac{1}{T}\right)\right]. \tag{6.2}$$

The correct associative solution is assumed when the recursive equation reaches a fixed point solution.
Starting from the outlined theory, a particular energy function has been defined, implemented in and tested in [92] using the above described generated data.

The obtained efficiency (a track is assumed to be correctly associated if at least four consecutive connections are correctly associated) is of 97 % for the case of 100 ghost hits. We refer to [92] for more details on the network definition and implementation.

As already mentioned, the full problem of tracking in particle physics consists in two parts: i) association of the hits; ii) reduce as much as possible the errors (due to detector noise) in the hits position. Therefore, if we assume the association of the hits achieved by the neural network, we have at disposal a number of associated experimental measurement (in subsequent chambers planes); for each of this, doing the charge centroid in both x and y strips coordinate, one obtains the position of the charge particle, but the coordinates are affected by resolution and multiple coulomb scattering effects. In order to reduce those errors one has to approach to so called *Linear inverse problems* (described in the following section): applied in the specific case of tracks filtering in particle physics, this means that one has to define a liner model describing the propagation of a true track (described by the vector $\mathbf{y}$) trough a detector and to use a stochastic model describing the noise of the detector in order to subtract this to the measured coordinate described by the vector $\mathbf{x}$ (i.e. maximizing the posterior probability).

6.3 Linear inverse problems

An inverse problem is a problem in which observed measurements must be converted into informations about the physical quantities one is interested in. If the relation between the measured and the physical quantities is linear, we are talking about linear inverse problem. It is important to point out that, even in the case of linear equations, in the real world any measurement is affected by several source of uncertainties, so the linear relation becomes stochastic to take into account those uncertainties. Therefore, it seems natural to treat these problems within a probabilistic framework, namely the so called Maximum A Posteriori (MAP) formulation (i.e. see [97, 98, 99]), instead of algebraic only (common in most books [100]). With this aim, for the moment, we restrict ourself to linear models in the parameter space and Gaussian distributed stochastic processes.
The measured quantities $\mathbf{y}$ are connected to the physical ones $\mathbf{x}$ by the equation

$$\mathbf{y} = \hat{\mathbf{C}}\mathbf{x} + \mathbf{n} \tag{6.3}$$

where $\mathbf{y} \in \mathbb{R}^N$, $\hat{\mathbf{C}} \in \mathbb{R}^{N\times M}$, $\mathbf{x} \in \mathbb{R}^M$ and $\mathbf{n} \in \mathbb{R}^N$. The stochastic part is due to $\mathbf{n}$, that originates from a Gaussian distribution with covariance matrix $\hat{\mathbf{\Gamma}}$ and mean $\mathbf{0}$, for sake of simplicity.
From this assumptions, it is easy to find the probability distributions of the measurements conditioned to the physical quantities, called *Likelihood function*

$$\begin{aligned} &p(\mathbf{y}|\mathbf{x}) = p(\mathbf{n} = \mathbf{y} - \hat{\mathbf{C}}\mathbf{x}) = \\ &\frac{1}{(2\pi)^{\frac{N}{2}}\sqrt{\det\hat{\mathbf{\Gamma}}}} \exp\left[-\frac{1}{2}(\mathbf{y} - \hat{\mathbf{C}}\mathbf{x})^{\mathrm{T}}\hat{\mathbf{\Gamma}}^{-1}(\mathbf{y} - \hat{\mathbf{C}}\mathbf{x})\right] \end{aligned} \tag{6.4}$$

and we denote the non-constant part of the exponent with the function

$$\mathcal{E}(\mathbf{x};\mathbf{y}) = (\mathbf{y} - \hat{\mathbf{C}}\mathbf{x})^{\mathrm{T}}\hat{\mathbf{\Gamma}}^{-1}(\mathbf{y} - \hat{\mathbf{C}}\mathbf{x}). \tag{6.5}$$

In the special case of identical and scorrelated Gaussian processes, the covariance matrix reduce to a multiple of the unity $\hat{\mathbf{\Gamma}} = \mathrm{R}^2\hat{\mathrm{I}}$, where R^2 is the variance of the processes. Keeping in mind the summary of joint probability properties given in Appendix B, it is easy to recognize that the joint probability of $\mathbf{x}$ and $\mathbf{y}$ is proportional to the likelihood and exactly

$$p(\mathbf{x},\mathbf{y}) = p(\mathbf{y}|\mathbf{x})p(\mathbf{x}). \tag{6.6}$$

Then to reconstruct the whole information we need to know (or to assign) the *a priori* probability distribution of the $\mathbf{x}$. The easiest case is the one in which $p(\mathbf{x})$ is a constant, but for the moment we assume the less easy (but analytically solvable) case of a multivariate Gaussian prior distribution with covariance (symmetric) matrix $\hat{\mathbf{P}}$ and mean $\bar{\mathbf{x}}$

$$p(\mathbf{x}) \propto \exp\left[-\frac{1}{2}\mathcal{S}(\mathbf{x})\right], \tag{6.7}$$

where

$$\mathcal{S}(\mathbf{x}) = (\mathbf{x}-\bar{\mathbf{x}})^{\mathrm{T}}\hat{\mathbf{P}}^{-1}(\mathbf{x}-\bar{\mathbf{x}}). \tag{6.8}$$

At this stage we can write the posterior probability density

$$p(\mathbf{x}|\mathbf{y}) \propto \exp\left\{-\frac{1}{2}\left[\mathcal{E}(\mathbf{x};\mathbf{y})+\mathcal{S}(\mathbf{x})\right]\right\} \tag{6.9}$$

where a normalization factor is disregarded. It will be useful to rewrite the argument of the exponent as an explicit quadratic form with respect to $\mathbf{x}$

$$\begin{aligned}\mathcal{E}(\mathbf{x};\mathbf{y})+\mathcal{S}(\mathbf{x}) &= (\mathbf{y}-\hat{\mathbf{C}}\mathbf{x})^{\mathrm{T}}\hat{\mathbf{\Gamma}}^{-\mathbf{1}}(\mathbf{y}-\hat{\mathbf{C}}\mathbf{x})+(\mathbf{x}-\bar{\mathbf{x}})^{\mathrm{T}}\hat{\mathbf{P}}^{-1}(\mathbf{x}-\bar{\mathbf{x}})\\ &= \mathbf{x}^{\mathrm{T}}(\hat{\mathbf{C}}^{\mathrm{T}}\hat{\mathbf{\Gamma}}^{-1}\hat{\mathbf{C}}+\hat{\mathbf{P}}^{-1})\mathbf{x}-(\mathbf{y}^{\mathrm{T}}\hat{\mathbf{\Gamma}}^{-1}\hat{\mathbf{C}}+\bar{\mathbf{x}}^{\mathrm{T}}\hat{\mathbf{P}}^{-1})\mathbf{x}+\\ &\quad-\mathbf{x}^{\mathrm{T}}(\hat{\mathbf{C}}^{\mathrm{T}}\hat{\mathbf{\Gamma}}^{-1}\mathbf{y}+\hat{\mathbf{P}}^{-1}\bar{\mathbf{x}})+(\mathbf{y}^{\mathrm{T}}\hat{\mathbf{\Gamma}}^{-1}\mathbf{y}+\bar{\mathbf{x}}^{\mathrm{T}}\hat{\mathbf{P}}^{-1}\bar{\mathbf{x}})\end{aligned} \tag{6.10}$$

and it is possible to complete the square by using the identity

$$\begin{aligned}&Q(\mathbf{x}) = \mathbf{x}^{\mathrm{T}}\hat{\mathbf{H}}\mathbf{x}-\mathbf{g}^{\mathrm{T}}\mathbf{x}-\mathbf{x}^{\mathrm{T}}\mathbf{g}+\mathbf{Q_0} =\\ &(\mathbf{x}-\hat{\mathbf{H}}^{-1}\mathbf{g})^{\mathrm{T}}\hat{\mathbf{H}}(\mathbf{x}-\hat{\mathbf{H}}^{-1}\mathbf{g})+(\mathbf{Q_0}-\mathbf{g}^{\mathrm{T}}\hat{\mathbf{H}}^{-1}\mathbf{g})\end{aligned} \tag{6.11}$$

where the matrix $\hat{\mathbf{H}}$ is symmetric and non singular, $\mathbf{g}$ is a vector and $\mathbf{Q_0}$ is a scalar. One obtains

$$\begin{aligned}\mathcal{E}(\mathbf{x};\mathbf{y})+\mathcal{S}(\mathbf{x}) &= (\mathbf{x}-\tilde{\mathbf{x}})^{\mathrm{T}}(\hat{\mathbf{C}}^{\mathrm{T}}\hat{\mathbf{\Gamma}}^{-1}\hat{\mathbf{C}}+\hat{\mathbf{P}}^{-1})(\mathbf{x}-\tilde{\mathbf{x}})+\\ &\quad+\Big(\mathbf{y}^{\mathrm{T}}\hat{\mathbf{\Gamma}}^{-1}\mathbf{y}+\bar{\mathbf{x}}^{\mathrm{T}}\hat{\mathbf{P}}\bar{\mathbf{x}}-\tilde{\mathbf{x}}^{\mathrm{T}}(\hat{\mathbf{C}}^{\mathrm{T}}\hat{\mathbf{\Gamma}}^{-1}\hat{\mathbf{C}}+\hat{\mathbf{P}}^{-1})^{-1}\tilde{\mathbf{x}}\Big)\end{aligned} \tag{6.12}$$

where

$$\tilde{\mathbf{x}} = \left[\hat{\mathbf{C}}^{\mathrm{T}}\hat{\mathbf{\Gamma}}^{-\mathbf{1}}\hat{\mathbf{C}}+\hat{\mathbf{P}}^{-1}\right]^{-1}(\hat{\mathbf{C}}^{\mathrm{T}}\hat{\mathbf{\Gamma}}^{-1}\mathbf{y}+\hat{\mathbf{P}}^{-1}\bar{\mathbf{x}}). \tag{6.13}$$

Considering the general expression of a quadratic form such as (6.11) in terms of components one can find the stationary point:

$$\frac{\partial Q}{\partial x_i} = 2\sum_j h_{ij}x_j - 2g_i = 0 \tag{6.14}$$

which in the specific case corresponds to $\tilde{\mathbf{x}}$, where h_{ij} is the generic element of $\hat{\mathbf{H}}$.
Therefore, if $\hat{\mathbf{C}}^{\mathrm{T}}\hat{\mathbf{\Gamma}}^{-\mathbf{1}}\hat{\mathbf{C}}+\hat{\mathbf{P}}^{-1}$ is an invertible matrix, by solving the system of equations

$$\left[\hat{\mathbf{C}}^{\mathrm{T}}\hat{\mathbf{\Gamma}}^{-\mathbf{1}}\hat{\mathbf{C}}+\hat{\mathbf{P}}^{-1}\right]\tilde{\mathbf{x}} = (\hat{\mathbf{C}}^{\mathrm{T}}\hat{\mathbf{\Gamma}}^{-1}\mathbf{y}+\hat{\mathbf{P}}^{-1}\bar{\mathbf{x}}) \tag{6.15}$$

one obtains the maximum solution $\tilde{\mathbf{x}}$. The covariance of the posterior probability density turns to be

$$\tilde{\mathbf{P}} = (\hat{\mathbf{C}}^{\mathrm{T}}\hat{\mathbf{\Gamma}}^{\mathbf{-1}}\hat{\mathbf{C}} + \hat{\mathbf{P}}^{-1})^{-1} \tag{6.16}$$

and it is easy to realize that one can recover the well known *maximum likelihood method* simply putting $\hat{\mathbf{P}}^{-1} = 0$, or in other words choosing a uniform prior distribution for $\mathcal{S}$.

6.3.1 The recursive problem

In real situations, the data vector $\mathbf{y}$ is updated during the time, therefore can be useful to obtain a recursive form for the solution that allows to avoid the need to recalculate the matrices for every new data. For the moment we assumed that only new data are collected, while the state vector of the physical system $\mathbf{x}$ is constant in time, this situation is known as the solution of *recursive least square* problem. At any time the k datum is related to the physical system through the relation

$$\mathbf{y}_k = \hat{\mathbf{C}}_k\mathbf{x} + \mathbf{n}_k \tag{6.17}$$

By what we learned in above, it is natural to use the recursive form of the Bayes theorem in the following way

i) for the datum $\mathbf{y}_k$ we can calculate the following quantities

$$\tilde{\mathbf{P}} = (\hat{\mathbf{P}}^{-1} + \hat{\mathbf{C}}^{\mathrm{T}}\hat{\mathbf{\Gamma}}^{\mathbf{-1}}\hat{\mathbf{C}})^{-1} \tag{6.18}$$

$$\tilde{\mathbf{x}} = \tilde{\mathbf{P}}(\hat{\mathbf{C}}^{\mathrm{T}}\hat{\mathbf{\Gamma}}^{-1}\mathbf{y} + \hat{\mathbf{P}}^{-1}\bar{\mathbf{x}}) \tag{6.19}$$

ii) we use the posterior probability as a prior for the datum $k+1$, so $\bar{\mathbf{x}}_{k+1} = \tilde{\mathbf{x}}_k$ and $\hat{\mathbf{P}}_{k+1} = \tilde{\mathbf{P}}_k$;

iii) do this for all the subsequent data, using the obtained posterior as new prior.

The advantage of this procedure is obvious, at any new stage we have a better knowledge of the posterior probability density one has to converge to. One difficulty still remains: a sufficient computational power is needed to perform the inversion of matrices.
To avoid in part this problem it is useful to rearrange the (6.18) by using the *Woodbury formula* $(\mathbf{A} - \mathbf{B}\mathbf{D}^{\mathbf{-1}}\mathbf{C})^{\mathbf{-1}} = \mathbf{A}^{\mathbf{-1}} + \mathbf{A}^{\mathbf{-1}}\mathbf{B}(\mathbf{D} - \mathbf{C}\mathbf{A}^{\mathbf{-1}}\mathbf{B})^{\mathbf{-1}}\mathbf{C}\mathbf{A}^{\mathbf{-1}}$:

$$\tilde{\mathbf{P}}_k = \hat{\mathbf{P}}_k - \hat{\mathbf{P}}_k\hat{\mathbf{C}}_k^{\mathrm{T}}\left(\hat{\mathbf{\Gamma}}_k + \hat{\mathbf{C}}_k\hat{\mathbf{P}}_k\hat{\mathbf{C}}_k^{\mathrm{T}}\right)^{-1}\hat{\mathbf{C}}_k\hat{\mathbf{P}}_k \tag{6.20}$$

where now only one matrix has to be inverted.
The updated formula for the $\mathbf{x}$, after taking into account (6.18), then becomes:

$$\begin{aligned}\tilde{\mathbf{x}} &= \tilde{\mathbf{P}}(\hat{\mathbf{P}}^{-1}\bar{\mathbf{x}} + \hat{\mathbf{C}}^{\mathrm{T}}\hat{\mathbf{\Gamma}}^{-1}\mathbf{y})\\ &= \bar{\mathbf{x}}_k + \tilde{\mathbf{P}}_k\hat{\mathbf{C}}_k^{\mathrm{T}}\hat{\mathbf{\Gamma}}_k^{-1}(\mathbf{y}_k - \hat{\mathbf{C}}_k\bar{\mathbf{x}})\\ &= \bar{\mathbf{x}}_k + \hat{\mathbf{K}}_k(\mathbf{y}_k - \hat{\mathbf{C}}_k\bar{\mathbf{x}})\end{aligned} \tag{6.21}$$

where $\hat{\mathbf{K}}_k = \tilde{\mathbf{P}}_k\hat{\mathbf{C}}_k^{\mathrm{T}}\hat{\mathbf{\Gamma}}_k^{-1}$ is called **Gain matrix**.

6.4 Kalman Filter

Up to now we assumed that the physical system $\mathbf{x}$ is non-evolving. But, most of the times one has to deal with data related to systems that evolve following deterministic laws (such as a body falling) or more generally deterministic-stochastic laws (such as the air viscosity during the fall). If one is able to describe the evolution of the state vector with a linear system (as suggested by Kalman in 1960 [101]), the gained information can be used to solve a time dependent linear inverse problem. Let us consider discrete time steps, that is usually the case in numerically solvable problems, the evolution equation of the physical system is described by an inhomogeneous linear transformation of the form

$$\mathbf{x}_{k+1} = \hat{\mathbf{\Phi}}_k \mathbf{x}_k + \mathbf{b}_k + \mathbf{e}_k \tag{6.22}$$

where $\hat{\mathbf{\Phi}}_k$ is the time evolution operator between two following time steps, $\mathbf{b}_k$ is a know vector and $\mathbf{e}_k$ is a vector that takes into account the information about non stochastic physical processes; from now on, we assume it belongs to zero-mean Gaussian processes with covariance matrix $\hat{\mathbf{S}}_k$. At each time step, we measure the data related to the physical system by the usual relation

$$\mathbf{y}_k = \hat{\mathbf{C}}_k \mathbf{x}_k + \mathbf{n}_k \tag{6.23}$$

where $\mathbf{n}_k$ is the noise with covariance matrix $\hat{\mathbf{\Gamma}}_k$. We now go through the first steps to clarify how this model works. Using what derived in the above section, from the relation (6.23) we derive the state vector $\mathbf{x}_1$ knowing the measurement at time $k = 1$; now we can consider the time evolved state

$$\mathbf{x}_2 = \hat{\mathbf{\Phi}}_1 \mathbf{x}_1 + \mathbf{b}_1 + \mathbf{e}_1 \tag{6.24}$$

where all the probability density at time $t = 1$ are Gaussian. Therefore, also the $\mathbf{x}_2$ at time $t = 2$ is Gaussian distributed, with mean

$$E[\mathbf{x}_2] = \hat{\mathbf{\Phi}}_1 \cdot E[\mathbf{x}_1] + \mathbf{b}_1 \tag{6.25}$$

and covariance

$$\begin{aligned} E[(\mathbf{x}_2 - E[\mathbf{x}_2])(\mathbf{x}_2 - E[\mathbf{x}_2])^{\mathrm{T}}] &= E[(\hat{\mathbf{\Phi}}_1(\mathbf{x}_1 - E[\mathbf{x}_1]) + \mathbf{e}_1)(\hat{\mathbf{\Phi}}_1(\mathbf{x}_1 - E[\mathbf{x}_1]) + \mathbf{e}_1)^{\mathrm{T}}] \\ &= \hat{\mathbf{\Phi}}_1 E[(\mathbf{x}_1 - E[\mathbf{x}_1])(\mathbf{x}_1 - E[\mathbf{x}_1])^{\mathrm{T}}]\hat{\mathbf{\Phi}}_1^{\mathrm{T}} + E[\mathbf{e}_1\mathbf{e}_1^{\mathrm{T}}] \end{aligned} \tag{6.26}$$

The evolution equation gives us the *prior* information on $\mathbf{x}_2$ before measuring $\mathbf{y}_2$. Therefore we have

$$\bar{\mathbf{x}}_2 = \hat{\mathbf{\Phi}}_1 \tilde{\mathbf{x}}_1 + \mathbf{b}_1 \tag{6.27}$$

$$\hat{\mathbf{P}}_2 = \hat{\mathbf{\Phi}}_1 \tilde{\mathbf{P}}_1 \hat{\mathbf{\Phi}}_1^{\mathrm{T}} + \hat{\mathbf{S}}_1 \tag{6.28}$$

where $\bar{\mathbf{x}}_2$ is the *Kalman predicted state*. It is easy to understand the recursive generalization of this procedure.

To summarize, before measuring the datum $\mathbf{y}_k$, our state of knowledge of the system is given by $\bar{\mathbf{x}}_k$ and by the covariance matrix $\hat{\mathbf{P}}_k$; and after the datum $\mathbf{y}_k$ is measured, one can update the information calculating:

i) The covariance matrix of the posterior probability of $\mathbf{x}_k$

$$\tilde{\mathbf{P}}_k = \hat{\mathbf{P}}_k - \hat{\mathbf{P}}_k \hat{\mathbf{C}}_k^{\mathrm{T}} (\hat{\mathbf{\Gamma}}_k + \hat{\mathbf{C}}_k \hat{\mathbf{P}}_k \hat{\mathbf{C}}_k^{\mathrm{T}})^{-1} \hat{\mathbf{C}}_k \hat{\mathbf{P}}_k \tag{6.29}$$

ii) The *Kalman gain matrix*

$$\hat{\mathbf{K}}_k = \tilde{\mathbf{P}}_k \hat{\mathbf{C}}_k^{\mathrm{T}} \hat{\mathbf{\Gamma}}_k^{-1} \tag{6.30}$$

iii) The Kalman filtered state (the mean of the posterior probability)

$$\tilde{\mathbf{x}}_k = \bar{\mathbf{x}}_k + \hat{\mathbf{K}}_k (\mathbf{y}_k - \hat{\mathbf{C}}_k \bar{\mathbf{x}}_k) \tag{6.31}$$

iv) The covariance matrix of the prior probability of $\mathbf{x}_{k+1}$

$$\hat{\mathbf{P}}_{k+1} = \hat{\mathbf{\Phi}}_k \tilde{\mathbf{P}}_k \hat{\mathbf{\Phi}}_k^{\mathrm{T}} + \hat{\mathbf{S}}_k \tag{6.32}$$

v) The mean of the prior probability for the state $k+1$

$$\bar{\mathbf{x}}_{k+1} = \hat{\mathbf{\Phi}}_k \tilde{\mathbf{x}}_k + \mathbf{b}_k \tag{6.33}$$

We remark that, as in the case of least square estimation, the first two steps may be reversed as (in this way the computation is faster because of the presence of one inversion only)

i) The *Kalman gain matrix*

$$\hat{\mathbf{K}}_k = \hat{\mathbf{P}}_k \hat{\mathbf{C}}_k^{\mathrm{T}} (\hat{\mathbf{\Gamma}}_k + \hat{\mathbf{C}}_k \hat{\mathbf{P}}_k \hat{\mathbf{C}}_k^{\mathrm{T}})^{-1} \tag{6.34}$$

ii) The covariance matrix of the posterior probability of $\mathbf{x}_k$

$$\tilde{\mathbf{P}}_k = (1 - \hat{\mathbf{K}}_k \hat{\mathbf{C}}_k) \hat{\mathbf{P}}_k \tag{6.35}$$

6.5 The smoothing procedure

Until now, we have characterized the problem of finding and tracking the true dynamics of a linear physical system by using a succession of measurements. But, from the recursive nature of the problem, it is clear that the information on a new step can be used not only to infer the next one, but also to refine the knowledge about a certain point in the past of the trajectory space. This reverse procedure is called *smoothing* [99]. Firstly we define the so called *auxiliary matrix*:

$$\hat{\mathbf{A}} = \hat{\mathbf{P}}_k \hat{\mathbf{\Phi}}_k^{\mathrm{T}} \hat{\mathbf{P}}_{k+1}^{-1} \tag{6.36}$$

In order clarify the meaning of this, by using equation 6.14, we find that essentially it is the back propagation matrix,

$$\hat{\mathbf{A}} = \hat{\mathbf{P}}_k \hat{\mathbf{\Phi}}_k^{\mathrm{T}} [(\hat{\mathbf{\Phi}}_k^{\mathrm{T}})^{-1} \hat{\mathbf{P}}_k^{-1} \hat{\mathbf{\Phi}}_k^{-1}] = \hat{\mathbf{\Phi}}_k^{-1} \tag{6.37}$$

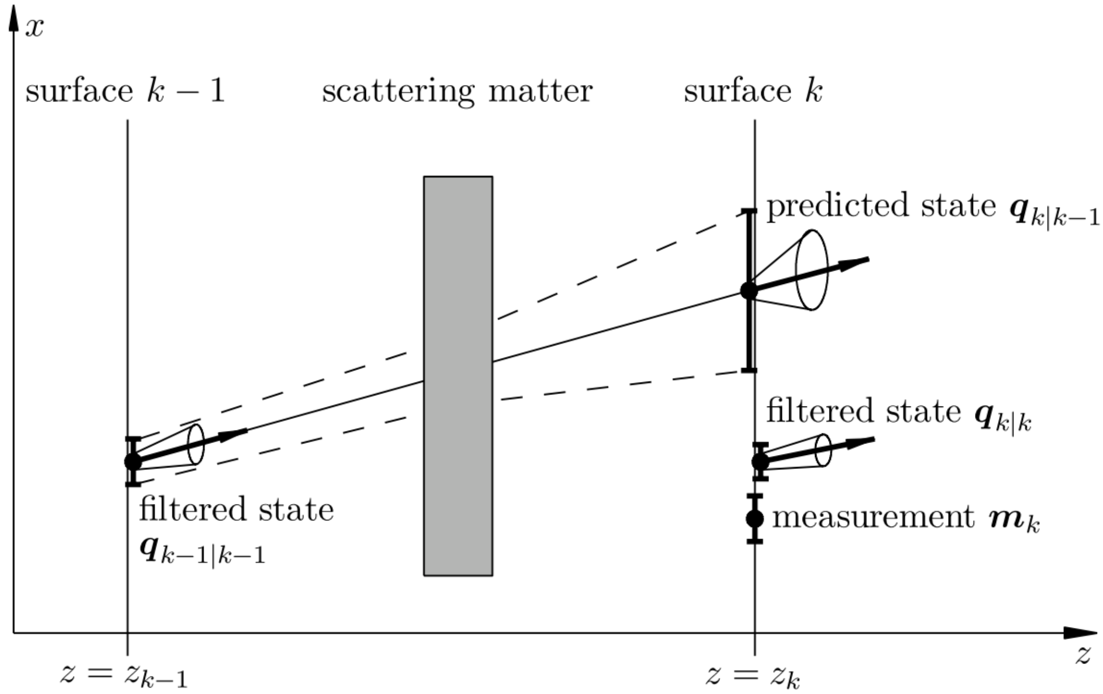

Figure 6.2: Prediction and filter step of the Kalman filter. The propagation proceeds in the z direction, while the x coordinate is measured. $\mathbf{m}_k$ is $\mathbf{y}_k$ and $\mathbf{q}_k$ is $\mathbf{x}_k$ in the text. (After ref. [94]).

if we do not have any active process described by $\mathbf{e}_k$ (for instance the multiple scattering in the case of tracking in HEP).
Therefore, the smoothing equations can be written as:

$$\mathbf{x}_k^S = \tilde{\mathbf{x}}_k + \hat{\mathbf{A}}_k(\mathbf{x}_{k+1}^S - \bar{\mathbf{x}}_{k+1}) \tag{6.38}$$

$$\mathbf{P}_k^S = \tilde{\mathbf{P}}_k - \hat{\mathbf{A}}_k(\hat{\mathbf{P}}_{k+1} - \mathbf{P}_{k+1}^S)\hat{\mathbf{A}}_k^{\mathrm{T}} \tag{6.39}$$

where with the superscript S we indicate the smoothed state vector and the initial conditions will be $\mathbf{x}_{k+1}^S = \tilde{\mathbf{x}}_{k+1}$ and $\mathbf{P}_{k+1}^S = \tilde{\mathbf{P}}_{k+1}$, being $k+1$ the last tracked element.
It is then clear that the choice to proceed in the forward or backward direction is related to the particular problem, and therefore, one method can be used as cross check for the other.

6.6 Tracking in particle physics

In the context of particle physics the Kalman algorithm is widely used to describe and reconstruct the particles propagation inside the tracking detectors. Let us consider a detector made of rectangular parallel planes of detection in which a crossing particle gives rise to a signal that must be used to obtain the physical trajectory of any particle.

For this purpose, we consider the relation (6.5) as the description of the propagation of the particle from one layer to the next, where $\mathbf{x}_k$ is the state vector of a particle at the layer k, $\hat{\mathbf{\Phi}}_k$ is the propagation matrix and $\mathbf{e}_k$ take into account the stochastic description of the multiple scattering (that will be described later). Let us consider for example the following state vector

$$\mathbf{x}_k = \begin{pmatrix} \text{x position} \\ \text{y position} \\ \text{x slope} \\ \text{y slope} \end{pmatrix} \tag{6.40}$$

By defining the state vector in this way we are able to incorporate the correlation between projections in a natural way, but with the drawback of having a larger dimension of the covariance matrix. Considering the steps in unit of time a reasonable form of the evolution matrix is

$$\hat{\mathbf{\Phi}}_k = \begin{pmatrix} 1 & 0 & \Delta z_k & 0 \\ 0 & 1 & 0 & \Delta z_k \\ 0 & 0 & 1 & 0 \\ 0 & 0 & 0 & 1 \end{pmatrix} \tag{6.41}$$

we have to describe the measurements from which the physical state is inferred, then the explicit forms of the measurement vector $\mathbf{y}$ and the measurement matrix has to be decided. We assume

$$\mathbf{y}_k = \begin{pmatrix} \text{x measured coordinate} \\ \text{y measured coordinate} \end{pmatrix} \tag{6.42}$$

and

$$\hat{\mathbf{C}} = \begin{pmatrix} 1 & 0 \\ 0 & 1 \end{pmatrix} \tag{6.43}$$

The vector $\mathbf{n}$ takes into account the measurement errors entering the matrix $\hat{\mathbf{\Gamma}}$ (namely, the spatial resolution), and to initialize the algorithm the following a priori diagonal covariance matrix has been chosen

$$\hat{\mathbf{P}} = \begin{pmatrix} Var[x] & 0 & 0 & 0 \\ 0 & Var[y] & 0 & 0 \\ 0 & 0 & Var[slope\ x] & 0 \\ 0 & 0 & 0 & Var[slope\ y] \end{pmatrix} \tag{6.44}$$

At this point, we have only to apply the recursive algorithm developed in the previous section to obtain the Kalman predicted state from one layer to the other.If we assume for the moment, that the multiple scattering can be approximated by a Gaussian distribution [102], then there are not additional formal complications in the problem (i.e. convolutions of Gaussian distributions are still Gaussian distributions).

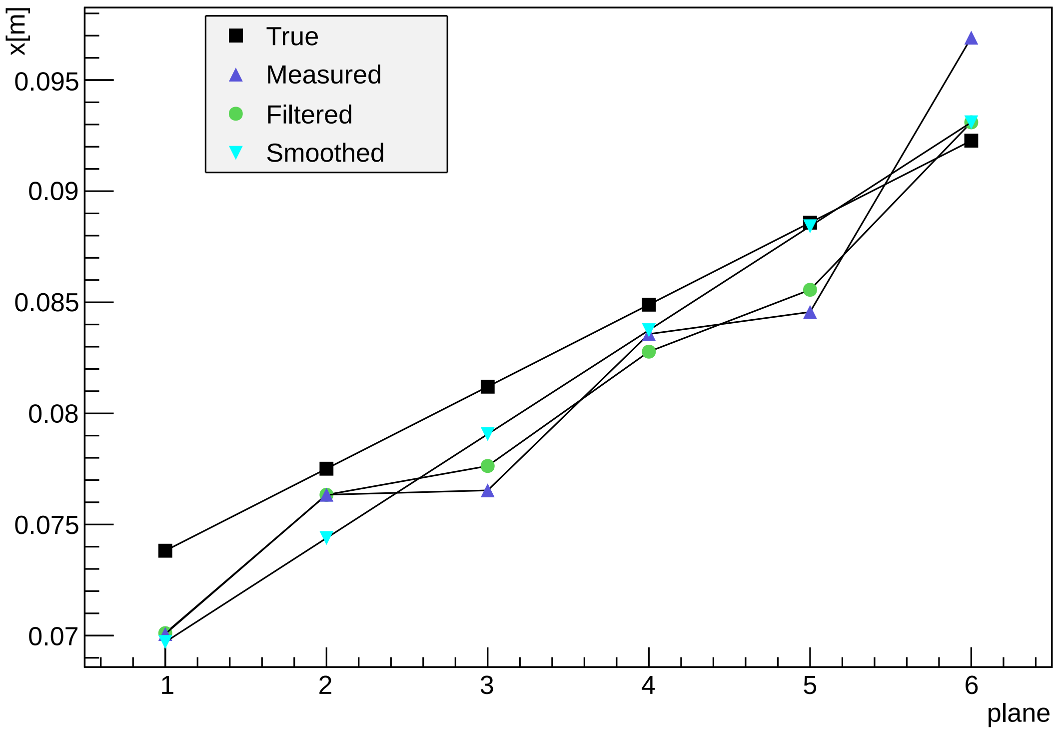

Figure 6.3: A first example of how the filtering and smoothing methods work: in black are the true (without detector spatial resolution effects) hit values; in violet are the measured hits assuming a resolution degradation Gaussian distributed with $\sigma = 0.01$ m; in green are the filtered points; in blue are the smoothed points. Six detector planes configuration has been chosen, with a distance between planes $d = 0.15\ m$.

6.7 Numerical results on filtering and smoothing

In the following the results of the application of filtering and smoothing are presented. All the following results are relative to a six 40×50 cm planes configuration, with a distance between the planes of $d = 0.15\ m$. Fig.6.3 (for the x coordinate) shows Kalman filtering and smoothing acting on hits with spatial resolution in (x, y) coordinate of 0.01 m. Violet points are the measured hits, green points are the filtered hits, blue points are the smoothed hits and black points are the true (which means without resolution effects) hits. It is easy to understand even in a pictorial view the way in which the filter and the smoothing acts.

Fig.6.4 shows the same configuration of the first case, but with a spacial resolution of 100 μm. In this case it is not possible to appreciate even pictorially how the procedure works. Therefore in Fig.6.5 the effects of Kalman filtering and smoothing is shown more quantitatively: the distance form the true hits is plotted for measured (black points), filtered (green points) and smoothed (blue points).

In Figs.6.6 the statistical distribution (in each of the six planes) of the resolution power recover

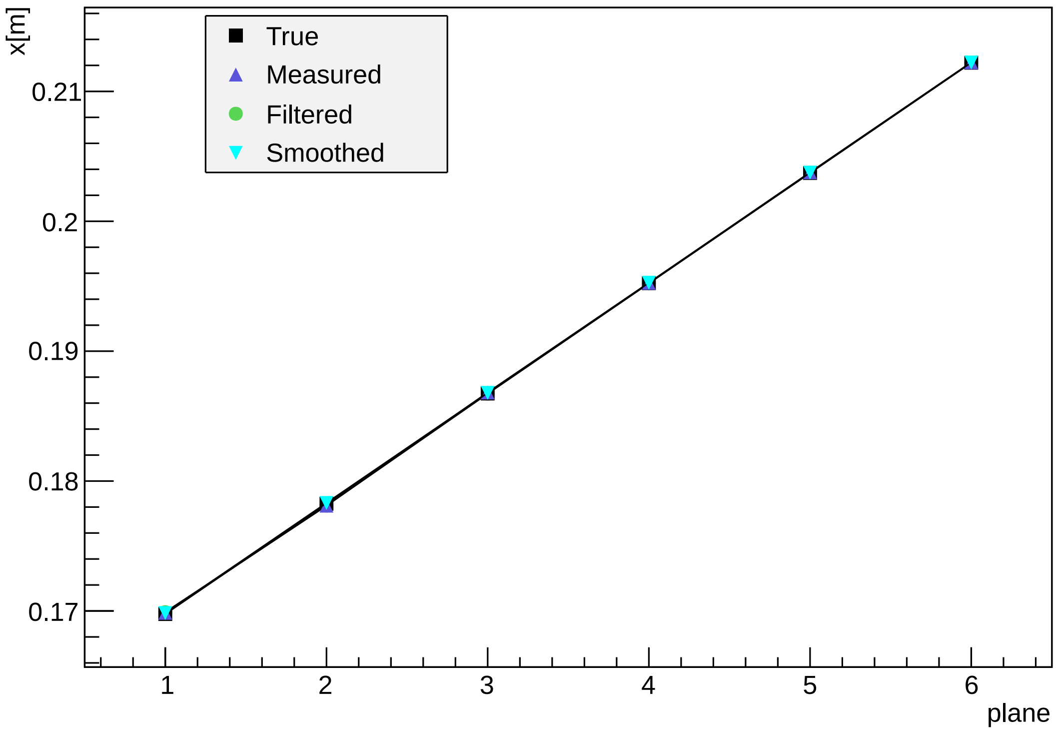

Figure 6.4: A more realistic spacial resolution configuration: in black are the true (without detector spacial resolution effects) hits value; for the measured hits a resolution degradation Gaussian distributed with $\sigma = 100\ \mu m$ is generated. Six detector pales configuration has been chosen.

has been shown for 1000 simulated track. What we learn from this toy rather realistic model configuration is that filtering and smoothing the hits, assuming a spatial resolution of $100\mu m$ and a plane spacing $d = 0.15\ m$ and no other physical effects, one can improve the spatial resolution to $\sim 30\mu m$ in the central planes.

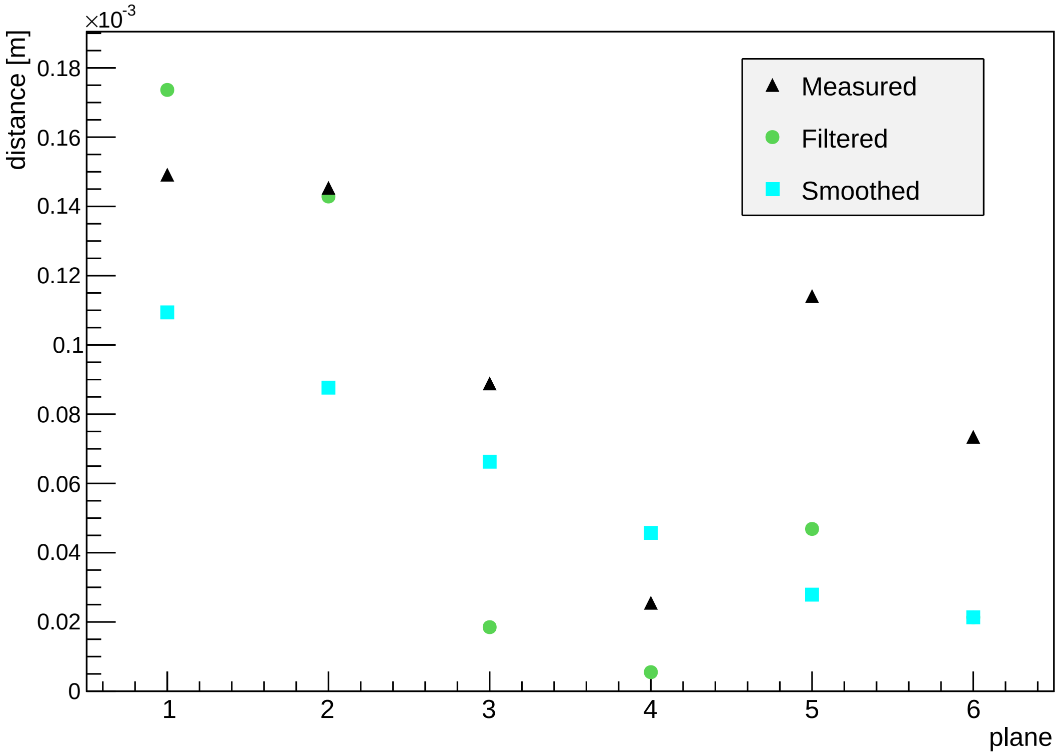

Figure 6.5: The distances from the true hits are shown (for the event in Fig. 6.4): black points show the distance between true and measured hits; green points show the distance between filtered and true hits; blue points show the distance between the smoothed hits and the true one.

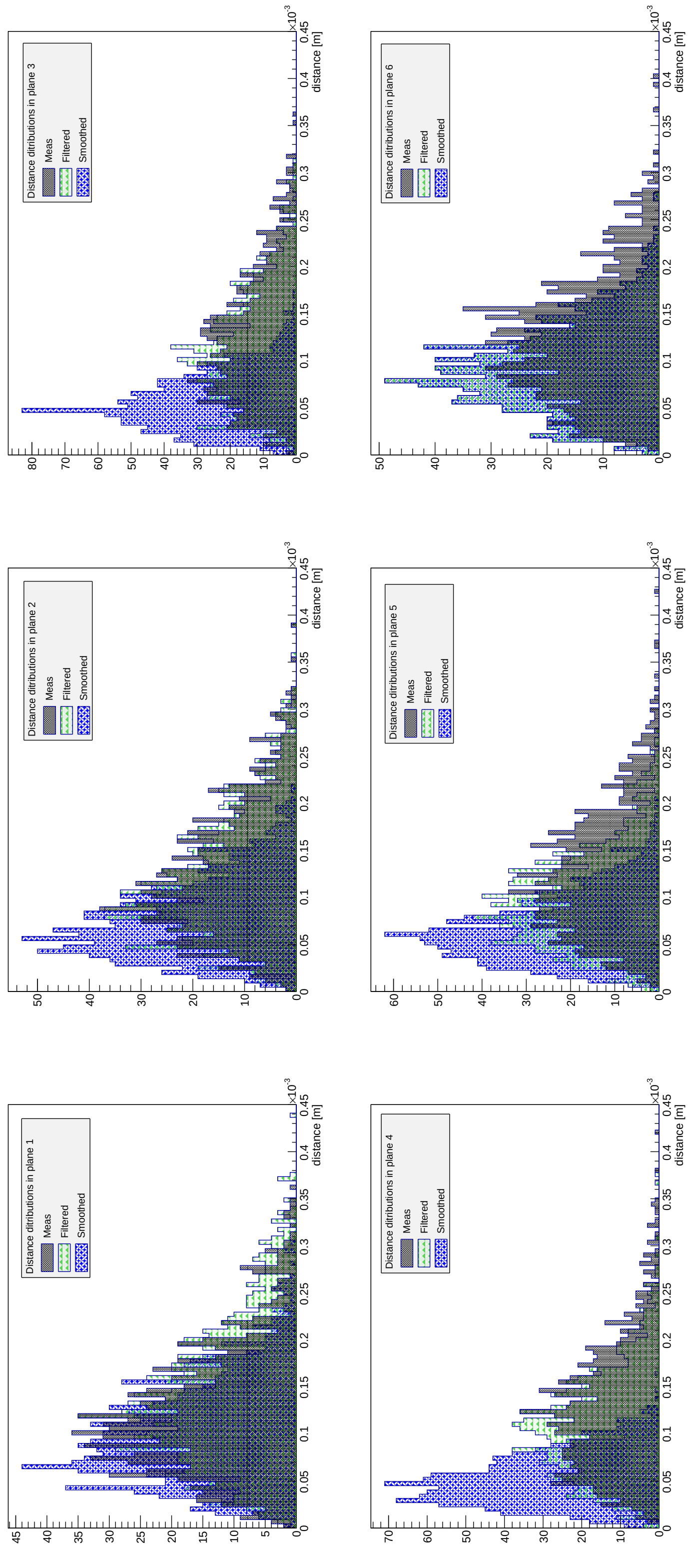

Figure 6.6: Statistical distribution of the distance of the measured, filtered and smoothed hits from the true one, in each of the six planes respectively.

6.8 Events with multiple scattering effects

In order to improve this picture, signal events have been generated with GEANT4 [93] using a preliminary model of the SBS spectrometer and a realistic model of the GEM chambers. In the GEM chambers region there is no magnetic field. The generated data include all the physical processes generating multiple scattering, whereas the simulated spatial resolution of the GEM chambers is of the order of 10 μm. The choice of reducing the nominal spatial resolution is led by the necessity of a systematic study of performance of the filtering procedure in the following two cases: i) the case in which the multiple scattering effects are dominating on the resolution effects; ii) the case in which the two effects are about of the same order. In Fig.6.7 a typical signal generated event is shown.

6.8.1 Multiple Coulomb scattering covariance matrix

In order to study the realistic data, we need to define a physical model of the multiple scattering process and a covariance matrix which will enter in the Kalman filtering algorithm trough the above defined $\hat{\mathbf{S}}$ matrix.
Let us consider the multiple scattering of the charged particle passing through subsequent chamber planes. We consider the multiple scattering source only out of the chamber plane (no multiple scattering effects are considered in the space between planes); the relevant parameters are:

i) σ the spatial resolution of the measurements,

ii) the distance between two chamber planes d,

iii) the number of planes N,

iv) the fraction of the radiation length of the passive material $x_0 = x/X_0$, where x is the thickness of the material and X_0 is the radiation length.

The multiple scattering error is (see [104])

$$\theta_0 = \frac{13.6MeV}{\beta cp}\sqrt{x/X_0}\,[1 + 0.038\ln(x/X_0)] \tag{6.45}$$

where $\theta_0 = \theta^{rms}_{plane} = \theta^{rms}_{space}/\sqrt{2}$ has been defined and θ_0 is the width of a Gaussian approximation for the central 98% of the angular distribution. The non-projected space and the projected plane are given, within the approximation, by

$$\frac{1}{2\pi\theta_0^2}\exp\left(-\frac{\theta^2_{space}}{2\theta_0^2}\right)d\Omega, \tag{6.46}$$

$$\frac{1}{\sqrt{2\pi\theta_0^2}}\exp\left(-\frac{\theta^2_{plane}}{2\theta_0^2}\right)d\theta_{plane}, \tag{6.47}$$

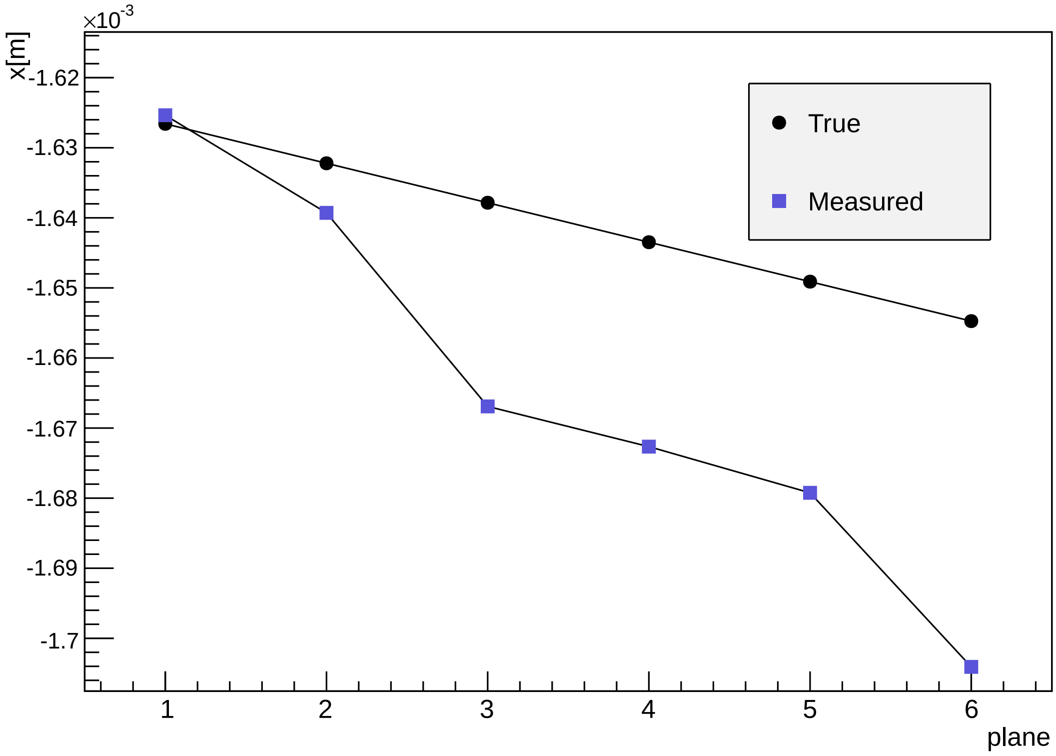

Figure 6.7: Violet points are an example of a generate GEANT4 signal track. In black the true track (without resolution and multiple scattering effects) is plotted.

where θ is the deflection angle. In this approximation $\theta^2_{space} \simeq \theta^2_{1(plane,x)} + \theta^2_{2(plane,y)}$, with the x and y axes are orthogonal to the direction of motion and $d\Omega \simeq d\theta_{1(plane,x)} d\theta_{2(plane,y)}$. Deflections into $\theta_{1(plane,x)}$ and $\theta_{2(plane,y)}$ are independent and identically distributed.
Therefore, the covariance matrix elements, $\langle \theta_i, \theta_j \rangle$ for the scattering angle θ_1 and θ_2 can be written as

$$\langle \theta_i, \theta_j \rangle = \theta_0^2 \delta_{ij}, \tag{6.48}$$

and the covariance matrix elements $\langle P_i, P_j \rangle$ for any two arbitrary functions $P_i(\theta_1, \theta_2)$ and $P_j(\theta_1, \theta_2)$ can be calculated using the propagation of errors

$$\langle P_i, P_j \rangle = \theta_0^2 \left(\frac{\partial P_i}{\partial \theta_1} \frac{\partial P_j}{\partial \theta_1} + \frac{\partial P_i}{\partial \theta_2} \frac{\partial P_j}{\partial \theta_2} \right). \tag{6.49}$$

Let us consider the state vector 6.40

$$\bar{x} = \begin{pmatrix} P_1 \\ P_2 \\ P_3 \\ P_4 \end{pmatrix} = \begin{pmatrix} z \tan \theta_x \\ z \tan \theta_y \\ \tan \theta_x \\ \tan \theta_y \end{pmatrix} \tag{6.50}$$

considering the displacement of the track unit vector $(0,0,1)$ directed along $\hat{z}$ caused by the multiple scattering, which gives the new vector $\left(1/\sqrt{1+\tan^2\theta_1+\tan^2\theta_2}\right)(\tan\theta_1, \tan\theta_2, 1)$ and consequently two new $\tan\theta_x^*$, $\tan\theta_y^*$ entering in the track state vector, it is possible to obtain a simple form for the covariance matrix in the limit of small scattering angles $\theta_1, \theta_2 \to 0$ (in this limit is $\theta_x^* \to \theta_x$, $\theta_y^* \to \theta_y$):

$$\hat{\mathbf{S}}_k = \begin{pmatrix} z^2\theta_0^2 A & z^2\theta_0^2 B & z\theta_0^2 A & z\theta_0^2 B \\ z^2\theta_0^2 B & z^2\theta_0^2 C & z\theta_0^2 B & z\theta_0^2 C \\ z\theta_0^2 A & z\theta_0^2 B & A & B \\ z\theta_0^2 B & z\theta_0^2 C & B & C \end{pmatrix} \tag{6.51}$$

where

$$A = \left[1 + (P_3)^2\right]\left[1 + (P_3)^2 + (P_4)^2\right], \tag{6.52}$$

$$B = P_3 P_4 \left[1 + (P_3)^2 + (P_4)^2\right], \tag{6.53}$$

$$C = \left[1 + (P_4)^2\right]\left[1 + (P_3)^2 + (P_4)^2\right]. \tag{6.54}$$

We refer to [105] for the details on the calculations. What is important to underline is that the error in the position increase with the space crossed by the charged particle.

6.9 Numerical results with GEANT4 realistic data

The GEANT4 data has been used also to study the track filtering in the two regimes where the multiple scattering is of the same order of the detector resolution and where the former is dominating to the latter. The multiple scattering angular variance θ_0^2, considering the GEM chamber thickness and a mean value of the momentum of the typical signal particle, is assumed to be of order 10^{-8} rad^2; a six chambers plane configuration has been chosen, with a distance $d = 0.15\ m$ between planes.
Therefore, for a spatial resolution of order $20\mu m$ the multiple scattering error become quickly dominant beyond the third plane. The following algorithm has been applied to the data in order to recover a straight line much closer as possible to the real track:

i) a least squares fit has been performed on the measured data considering both the resolution and the multiple scattering errors,

ii) the data have been filtered and smoothed adding in the Kalman algorithm the multiple scattering matrix $\hat{\mathbf{S}}$,

iii) the obtained filtered and smoothed points, with the respective errors obtained after the Kalman procedure have been fitted with a least squares method,

iv) for the three obtained straight line the distance from the true straight line has been evaluated in each plane z coordinate.

In Fig.6.8 are the obtained results: the mean distance (with the rms in the error bars) between the true trajectory and the fitted trajectories (measured in black, filtered in green and smoothed in blue) for an events sample are shown.
As expected, in the case in which the multiple scattering effects are dominating, the best fit procedure is the one in which the measured point are used. Furthermore the results suggest that the first three plane are those on which the uncertainties are minimized.

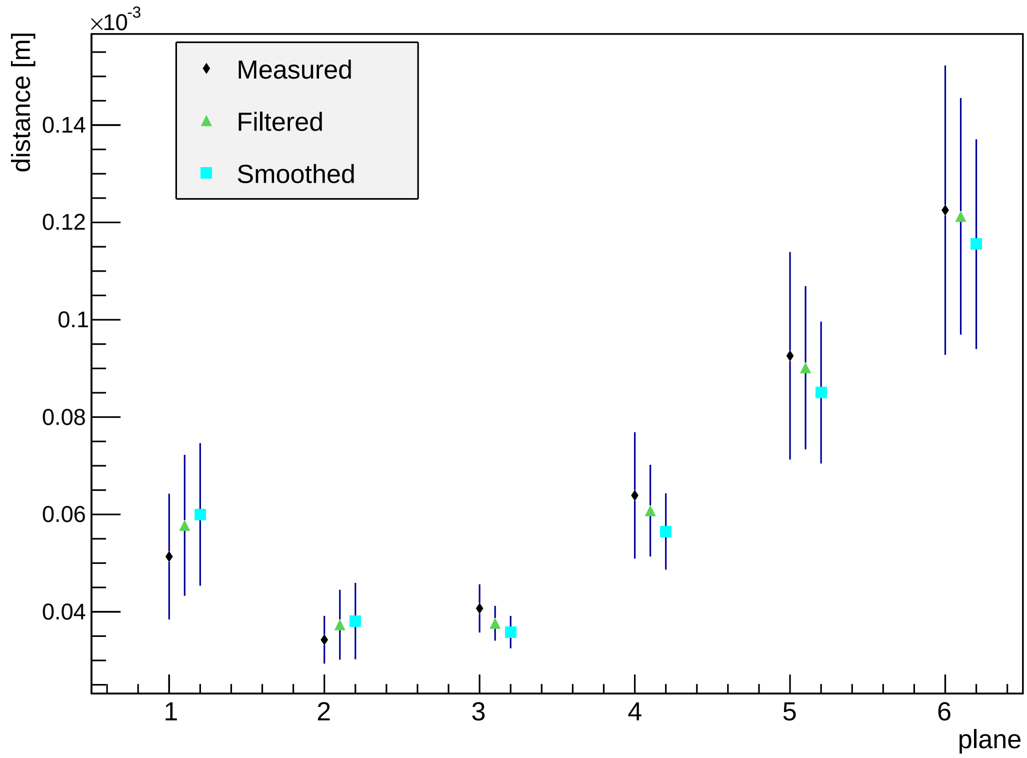

Figure 6.8: Mean distance, evaluated at the plane longitudinal coordinate, between the true trajectory and the fitted trajectories (measured in black, filtered in green and smoothed in blue) for a 1000 tracks sample. The simulated spatial GEM chambers resolution is of $20\mu m$.

We reiterate the above described procedure, but adding a Gaussian smearing to the simulated events in order to achieve the nominal GEM chambers spatial resolution of $70\mu m$.
In Fig. 6.9 is presented the result: the tracks mean distance (with the correspondent rms in the error bars) of the from the true points (in correspondence of the plane z coordinates) obtained fitting the measured, filtered and smoothed points. The results suggest that, in the case in which the detectors spatial resolution effects and the multiple scattering effects are of the same order, the fit of the filtered points is the better choice and the smallest errors are in the central planes region,

with a mean gain in resolution of some μm.

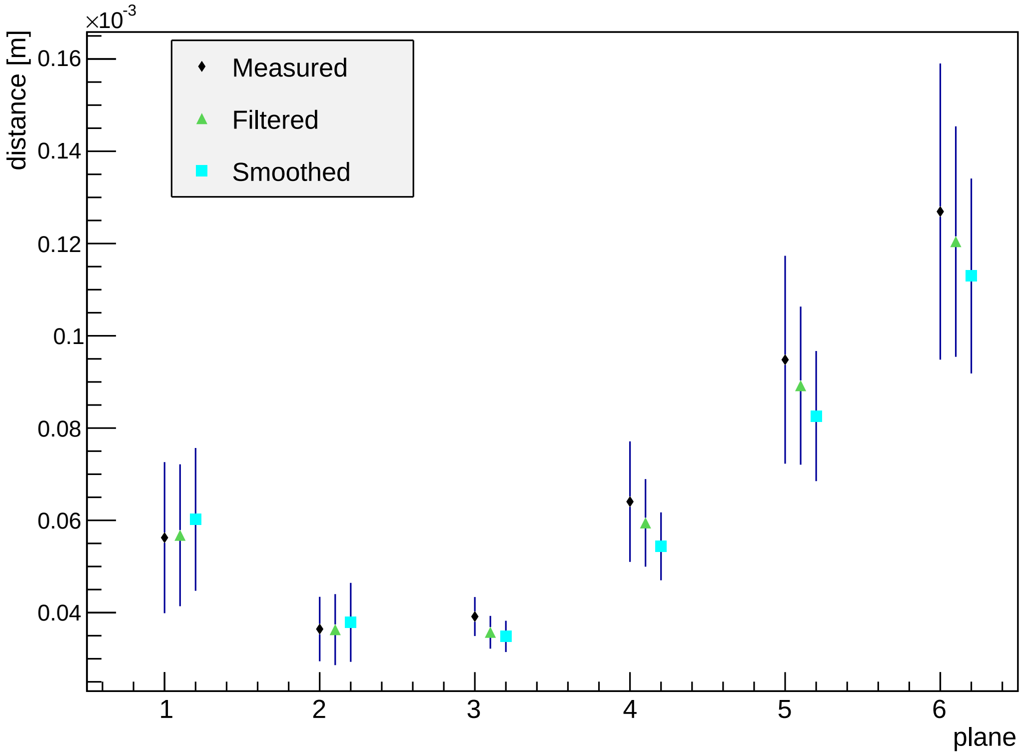

Figure 6.9: Mean distance, evaluated at the plane longitudinal coordinate, between the true trajectory and the fitted trajectories (measured in black, filtered in green and smoothed in blue) for a 1000 tracks sample. The simulated spatial GEM chambers resolution is of $70\mu m$.

6.10 Conclusions and future developments

We have applied the filtering and smoothing procedure to the signal particles hits firstly taking into account spatial resolution effects only, in order to test and understand the properties of the Kalman filtering algorithm. Then the procedure has been applied to realistic GEANT4 generated hits, taking into account also multiple scattering effects. The preliminary results on the realistic data seem suggest to that using filtered data a gain of order $10\mu m$ in spatial resolution with respect the measured data is possible.

The related issues to be approached in the future can be summarized as follows:

i) a systematic study of the initialization parameters of the Kalman filter, in particular varying the entity of the multiple scattering effects,

ii) a systematic study varying the number of used chamber planes for the best fit procedure.

Conclusions

In the path toward a deeper understanding of nucleon spin properties, it is remarkable the necessity of more precise informations on the neutron spin structure. In fact the existing data on proton and deuteron and the data on ^{3}He (neutron) are not sufficient nowadays to obtain a sound flavor decomposition of the nucleon TMDs. In particular the neutron data have limited accuracy, nevertheless they are crucial to achieve a better knowledge of the nucleon partonic spin structure. Then the planned precise direct measurement on the neutron is crucial for at least two reasons: i) to shed light on the apparent inconsistency of the physical picture of nucleon spin dependent partonic structure; ii) to make possible a sound flavor decomposition of the nucleon TMDs.

In this direction two parallel and complementary activities have been carried on, one concerning the development of an extended phenomenological framework describing the ^{3}He within the SIDIS formalism; second concerning the development of filtering and fitting algorithms able to work in high intensity and high precision frontiers.

Final state interaction has been included in the framework used nowadays to extract the neutron Single Spin Asymmetry from the ^{3}He data; through a generalized eikonal approximation (GEA). The study has been done in both the spectator and standard SIDIS. The preliminary results concerning standard SIDIS, suggest that the extraction method appears to be still solid even in taking into account final state interaction [59]. This seems basically due to the kinematical experimental conditions and to the use of asymmetries instead of cross sections. A preliminary study on the relativistic effects on the effective polarizations of protons and neutron in ^{3}He also suggests the reliability of the adopted extraction method [87, 88, 90, 91, 89]. Let us emphasize that, due to the high statistical accuracy expected in the next future experiments, more extended results (in terms of kinematical range for standard SIDIS) are desirable: i) the extraction procedure should be tested in combination with the Monte Carlo generator used in 5.1, (notice that the MC code has as an input the distorted spectral function, to be evaluated in a rather wide range of its variables, and this requests a sizable amount of computing resources); ii) the generalized eikonal approximation framework, where final state interaction are presently evaluated should be integrated in the Light-Front description of the spectral function.

A study of modern fitting and filtering methods for tracking has been done in order to approach the high intensity (and precision) condition in the planned future nucleon structure experiments. The Kalman filtering has been used to improve the spatial resolution of the particles hits in a tracking detector, with an emphasis to the application of a real configuration with GEM chambers. The obtained results seems to be promising. Further developments related to the tracking issue are: i) a more detailed study of the multiple scattering effects, changing both the spatial resolution effects and the numbers of chambers plane used for the track fit; ii) the study of tracks association methods based on Kalman filtering and other local techniques like Hough transform based methods.

Appendix A

Light-cone vectors

A four-vector a^μ with Cartesian contravariant components $a^\mu = (a^0, a^i)$ can be written, in the light-cone frame (see. Fig. A.1), as

$$a^\mu = \left[a^-, a^+, \vec{a}_T\right] = \left[\frac{a^0 - a^3}{\sqrt{2}}, \frac{a^0 + a^3}{\sqrt{2}}, a^1, a^2\right], \tag{A.1}$$

where the $\pm$ components are along the light-cone axes $x^\pm$. The scalar product of two light-cone

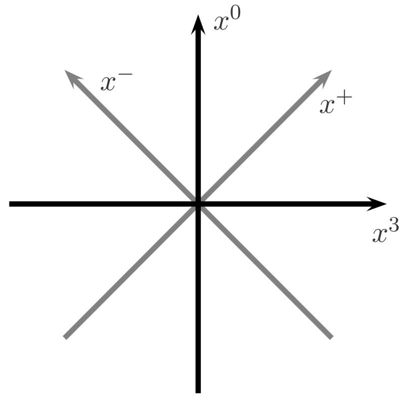

Figure A.1: The light-cone axes.

vectors reads:

$$a \cdot b = a^+ b^- + a^- b^+ - \vec{a}_T \cdot \vec{b}_T. \tag{A.2}$$

In the Bjorken limit ($Q^2 \to \infty, \nu \to \infty, x = const.$) the 4-momentum of the nucleon and of the virtual photon can be written in light-cone coordinates as:

$$P^\mu = \left[\frac{M^2}{2P^+}, P^+, \vec{0}\right], \tag{A.3}$$

$$q^\mu = \left[\frac{Q^2}{2xP^+}, -xP^+, \vec{0}\right]. \tag{A.4}$$

This parametrization is valid in any collinear frame (i.e. any reference frame in which the virtual-photon direction is antiparallel to the x^3 axis). In this parametrization, P^+ is the dominant variable in $1/Q$ expansion. In the IMF the plus component of the nucleon is of the order of Q.

Appendix B

Joint probabilities: Bayes theorem

Let us consider the joint probability of two events, it is well known that the following relation with the conditional probability holds

$$P(E \cap H) = P(E|H) \cdot P(H) \tag{B.1}$$

and, if the probability of H is not the null space $P(H) \neq 0$, the conditional probability of E to H is

$$P(E|H) = \frac{P(E \cap H)}{P(H)}. \tag{B.2}$$

It is also clear, from the commutativity of the logic product, that E and H can be exchange

$$P(E \cap H) = P(H \cap E) = P(E|H) \cdot P(H) = P(H|E) \cdot P(E) \tag{B.3}$$

At this point, assuming a set of events H_i instead of one and using the disintegration probability rule $P(E) = \sum_i P(E|H_i) \cdot P(H_i)$ (valid if assume a complete set of H_i) we can write the so called *Bayes theorem*:

$$P(H_i|E) = \frac{P(E|H_i) \cdot P(H_i)}{P(E)} = \frac{P(E|H_i) \cdot P(H_i)}{\sum_i P(E|H_i) \cdot P(H_i)} \tag{B.4}$$

Acknowledgments

This work was supported by the INFN sezione di Roma, Gruppo collegato Sanità. I desire to thank Dr. Evaristo Cisbani for the fundamental scientific suggestions and economical support.

Bibliography

[1] E. Rutherford, “The scattering of α and β particles by matter and the structure of the atoms”, Phil. Mag. **21**, 669 (1911); H. Geiger and E. Marsden, “On a diffuse reflection of the α particles”, Pro. Roy. Soc.A **82**, 495 (1909).

[2] M. Gell-Mann,”A schematic model of baryons and mesons”, Phys. Lett. **8**, 214 (1964).

[3] G. Zweig, “An SU(3) model for strong interaction symmetry and its breaking”, CERN preprints **TH-401**, **TH-412** (1964).

[4] M. Breidenbach et al. "Observed Behavior of Highly Inelastic Electron-Proton Scattering" Phys. Rev. Lett., **23**:935, (1969); E. D. Bloom et al. "High-Energy Inelastic e-p Scattering at 6° and 10°" Phys. Rev. Lett., **23**:930, (1969).

[5] J.D. Bjørken, “Asymptptic sum rules at infinite momentum”, Phys. Rev. **179**, 1547 (1969).

[6] J.D. Bjørken and E.A. Paschos, “Inelastic electron-proton and γ-proton scattering and the structure of the nucleon”, Phys. Rev. **185**, 1975 (1969).

[7] R. Feynman, “Very high-energy collisions of hadrons”, Phys. Rev. Lett. **23**, 1415 (1969).

[8] D.P. Barber et al., ”Discovery of Three-Jet Events and a Test of Quantum Chromodynamics at PETRA”, Phys. Rev. Lett. **43**, 830 (1979).

[9] C. Adloff et al. (H1 Collaboration), "Deep-inelastic inclusive e p scattering at low x and a determination of α_S", Eur. Phys. J. C**21**, 33 (2001).

[10] S. Chekanov et al. (ZEUS Collaboration), "Measurement of the neutral current cross section and F2 structure function for deep inelastic e+ p scattering at HERA", Eur. Phys. J. C21, 443 (2001).

[11] M.J. Alguard et al. (E80 Collaboration), ”Deep Inelastic Scattering of Polarized Electrons by Polarized Protons”, Phys. Rev. Lett. **37**, 1261 (1976).

[12] G. Baum et al. (E130 Collaboration), ”NewMeasurement of Deep-Inelastic e-p Asymmetries”, Phys. Rev. Lett. **51**, 1135 (1983).

[13] J. Ellis and R.L. Jaffe, ”Sum rule for deep-inelastic electroproduction from polarized protons”, Phys. Rev. D**9** 1444 (1974); ”Erratum: Sum rule for deep-inelastic electroproduction from polarized protons”, Phys. Rev D**10**, 1669 (1974).

[14] EMC, J.Ashman et al., ”A measurement of the spin asymmetry and determination of the structure function g1 in deep inelastic muon-proton scattering”, Phys. Lett. B **206**, 364 (1988).

[15] C. A. Aidala, S. D. Bass, D. Hasch and G. K. Mallot, "The spin structure of the nucleon", Rev. Mod. Phys. **85**, 2013.

[16] M. Walker, "Gluon Polarization Measurements from Correlated Probes", 2011, arXiv:1107.0917. P. Djawotho, "Gluon polarization measurements with inclusive jets at STAR", 2011 arXiv:1106.5769. D. de Fllorian, R. Sassot, M. Stratmann and W. Vogelsang, "Evidence for Polarization of Gluons in the Proton", Phys. Rev. Lett. **113**, 012001 (2014).

[17] B. Adeva et al. (SMC Collaboration), ”Polarized Quark distributions in the nucleon from semi-inclusive spin asymmetries”, Phys. Lett. B **420**, 180 (1998), arXiv:hepex/ 9711008.

[18] M Burkardt et al "Spin-polarized high-energy scattering of charged leptons on nucleons " Rep. Prog. Phys. **73** 016201, (2010)

[19] D.W. Sivers, “Single Spin Production Asymmetries from the Hard Scattering of Pointlike Constituents”, Phys. Rev D **41**, 83 (1990).

[20] J.C. Collins and D.E. Soper, "Parton distribution and decay functions", Nucl. Phys. **B194** (1982) 445.

[21] S. J. Brodsky, D. S. Hwang and I. Schmidt, "Final-state interactions and singlespin asymmetries in semi-inclusive deep inelastic scattering", Phys. Lett. B **530**, 99–107 (2002).

[22] M. Burkardt, "Impact parameter dependent parton distributions and transverse single spin asymmetries", Phys. Rev. D**66**, 114005 (2002).

[23] V. Barone, A. Drago and P.G. Ratcliffe, ”Transverse polarisation of quarks in hadrons”, Phys. Rep. **359**, 1 (2002).

[24] R. L. Jaffe, Spin, twist and hadron structure in deep inelastic processes, Talk given at Ettore Majorana International School of Nucleon Structure: 1st Course: The Spin Structure of the Nucleon", Erice, Italy, 3-10 Aug 1995, hep-ph/9602236.

[25] J.C. Collins, “Leading-twist single-transverse spin asymmetries: Drell-Yan and deepinelastic scattering”, Phys. Lett. B **536**, 43 (2002). arXiv:hep-ph/0204004.

[26] A. Bacchetta, M. Boglione, A. Henneman and P. J. Mulders, "Bounds on transverse momentum dependent distribution and fragmentation functions", Phys. Rev. Lett.**85**, 712 (2000).

[27] P.J. Mulders and R.D. Tangerman, “The complete tree-level result up to order 1/Q for polarized deep-inelastic leptoproduction”, Nucl. Phys. B **461**, 197 (1996).

[28] PAX Collaboration, “Technical Proposal for Antiproton-Proton Scattering Experiments with Polarization” arXiv:hep-ex/0505054 (2005).

[29] D. Sivers "The Adventure and the Prize", 2011, arXiv:1109.2521.

[30] J.C. Collins, “Fragmentation of transversely polarized quarks probed in transverse momentum distributions”, Nucl. Phys. B **396**, 161 (1993).

[31] A. Bacchetta, R. Kundu, A. Metz and P.J. Mulders, ”The Collins fragmentation function: A simple model calculation”, Phys. Lett. B **506**, 155 (2001).

[32] A. Bacchetta, R. Kundu, A.Metz and P.J.Mulders, ”Estimate of the Collins fragmentation function in a chiral invariant approach”, Phys. Rev. D **65**, 094021 (2002).

[33] A. Bacchetta, ”Probing the transverse spin of quarks in deep inelastic scattering”, PhD thesis (2002). arXiv:hep-ph/0212025.

[34] A. Bacchetta, M. Diehl, K. Goeke, A. Metz, P.J. Mulders, M. Schlegel, ”Semiinclusive deep inelastic scattering at small transverse momentum", **JHEP** 0702 (2007) 093, arXiv:hep-ph/0611265.

[35] M. Diehl and S. Sapeta, "On the analysis of lepton scattering on longitudinally or transversely polarized protons", Eur. Phys. J. C **41** (2005) 515–533, [hep-ph/0503023].

[36] A. Signori, et al. "Investigations into the flavor dependence of partonic transverse momentum." Journal of High Energy Physics 2013.11 (2013): 1-25.

[37] A. Signori, A. Bacchetta, M. Radici, and G. Schnell "Investigations into the flavor dependence of partonic transverse momentum", Journal of High Energy Physics, 2013(11), 1-25 (20.13).

[38] A. Bacchetta, M. G. Echevarria, M. Radici, and A. Signori, "Phenomenology from SIDIS and e^+e^- multiplicities" arXiv preprint arXiv:1409.7227 (2014).

[39] L. Pappalardo, "Measurement of Collins and Sivers asymmetries at HERMES", talk given at the 20008 Transversity Workshop, Ferrara, available at http://www.fe.infn.it/transversity2008/

[40] COMPASS Collaboration, "Collins and Sivers Transverse Spin Asymmetries for Pions and Kaons in Deuterons", CERN.PH-EP/2008-002.

[41] H. Wollny, "Transverse spin effects at COMPASS", presented at SPIN 2008", available at http://www.faculty.virginia.edu/spin2008/scientific program.html

[42] M. Contalbrigo, "Transverse Spin Physics at HERMES", presented at SPIN 2008", available at http://www.faculty.virginia.edu/spin2008/scientific program.html

[43] M. Anselmino et al., "Simultaneous extraction of transversity and Collins functions from new SIDIS and e+e- data", Phys. Rev. D **87** (2013) 094019

[44] J. Soffer, "Positivity constraints for spin-dependent parton distributions", Phys. Rev. Lett. **74** (1995) 1292-1294.

[45] M. Anselmino et al., "Single spin asymmetries in $lp \to hX$ processes: A test of factorization", **EPJA** 39, 89 (2009).

[46] M. Anselmino et al., "New insight on the Sivers transverse momentum dependent distribution function", J.Phys.Conf.Ser. **295** (2011) 012062

[47] X. Qian et al. (Jefferson Lab Hall A Collaboration), "Single Spin Asymmetries in Charged Pion Production from Semi-Inclusive Deep Inelastic Scattering on a Transversely Polarized ^{3}He Target at $Q^2 = 1.4 - 2.7GeV^2$", Phys. Rev. Lett. **107**, 072003 (2011).

[48] http://hallaweb.jlab.org/equipment/moller/

[49] http://hallaweb.jlab.org/compton/
http://arxiv.org/abs/1106.4851

[50] G. Cates, N. Liyanage, B. Wojtsekhowski et al., "Measurement of the Neutron Electric Form Factor GEn at High Q2", JLab experiment E02-013.

[51] F. Sauli, "GEM: A new concept for electron amplification in gas detectors", Nucl. Inst. Methods A**386**, 531 (1997).

[52] N. Akopov et al, "The HERMES dual-radiator ring imaging Cherenkov detector", Nucl. Instr. Meth. A **479** 511 (2002).

[53] R. De Leo, "Long-term operational experience with the HERMES RICH detector", talk presented at RICH 2007, Trieste, Italy; available at: http://rich2007.ts.infn.it/

[54] G. Corradi et al. "A novel High Voltage System for a triple GEM detector", NIMA **572** (2007) 96-97

[55] R.B. Wiringa, V.G.J. Stocks, and R. Schiavilla, Phys.Rev. C**51**, 38 (1995).

[56] M.J. French et al., Design and results from the APV25, a deep sub-micron CMOS front-end chip for the CMS tracker, NIM A**466** (2002) 359.

[57] S. Scopetta, "Neutron single spin asymmetries from semi-inclusive deepinelastic scattering off transversely polarized 3He" Phys. Rev. D **75** 054005 (2007).

[58] Cates G. et al., E12-09-018, JLAB approved experiment,

hallaweb.jlab.org/collab/PAC/PAC38/E12-09-018-SIDIS.pdf;

X.Jiang et al

www.jlab.org/exp_prog/generated/apphalla.html;

J. Arrington et al

www.jlab.org/~jinhuang/12GeV/12GeVLongitudinalHe3.pdf.

[59] L.P. Kaptari, A. Del Dotto, E. Pace, S. Scopetta, G. Salmè, "Distorted spin-dependent spectral function of an $A = 3$ nucleus and semi-inclusive deep-inelastic scattering processes", Phys. Rev. C **89** 035206 (2014).

[60] C. Ciofi degli Atti, L. P. Kaptari and S. Scopetta, “Semiinclusive deep inelastic lepton scattering off complex nuclei,” Eur. Phys. J. A **5**, 191 (1999).

[61] C. Ciofi Degli Atti, “Electron Scattering By Nuclei,” Prog. Part. Nucl. Phys. **3** (1978) 163; H. Meier-Hajduk, C. Hajduk, P. U. Sauer and W. Theis, “Quasielastic Electron Scattering From ^{3}He,” Nucl. Phys. A **395** (1983) 332.

[62] C. Ciofi degli Atti, S. Scopetta, E. Pace and G. Salmè, “Nuclear effects in deep inelastic scattering of polarized electrons off polarized ^{3}He and the neutron spin structure functions,” Phys. Rev. C **48**, 968 (1993).

[63] C. Ciofi degli Atti, E. Pace and G. Salmè, “spin-dependent spectral function of He-3 and the asymmetry in the process ^{3}He (polarized) (e (polarized),e-prime) X,” Phys. Rev. C **46**, 1591 (1992).

[64] R. -W. Schulze and P. U. Sauer, “Inelastic electron scattering from the three-nucleon bound states with polarization,” Phys. Rev. C **48**, 38 (1993).

[65] C. Ciofi degli Atti, E. Pace and G. Salmè, “Investigation of the neutron form-factors by inclusive quasielastic scattering of polarized electrons off polarized ^{3}He: A Theoretical overview,” Phys. Rev. C **51**, 1108 (1995)

[66] S. Pollock, H. W. Naus and J.H. Koch Phys. Rev. **C 53**, 2304 (1996).

[67] S. A. Kulagin, W. Melnitchouk, G. Piller and W. Weise, “Spin dependent nuclear structure functions: General approach with application to the deuteron,” Phys. Rev. C **52**, 932 (1995) [hep-ph/9504377].

[68] S. A. Kulagin and R. Petti, “Global study of nuclear structure functions,” Nucl. Phys. A **765**, 126 (2006) [hep-ph/0412425].

[69] S. A. Kulagin and W. Melnitchouk, “Spin structure functions of He-3 at finite Q**2,” Phys. Rev. C **78**, 065203 (2008) [arXiv:0809.3998 [nucl-th]].

[70] J. A. O. Marinho, T. Frederico, E. Pace, G. Salmè, and P. U. Sauer, Phys. Rev. D **77**, 116010 (2008).

[71] P.A.M. Dirac, Rev. Mod. Phys. **21**, 392 (1949).

[72] B. D. Keister and W. N. Polyzou, “Relativistic Hamiltonian dynamics in nuclear and particle physics,” Adv. Nucl. Phys. **20**, 225 (1991).

[73] B. Bakamjian and L.H. Thomas, Phys. Rev. **92**, 1300 (1953).

[74] C. Ciofi degli Atti et al., Physical Review C **46**, R 159 (1992); A. Kievsky et al., Physical Review C **56**, 64 (1997)

[75] U. Oelfke, P. U. Sauer and F. Coester, Nucl. Phys. A **518**, 518 (1990).

[76] X. Zheng, et al. "Precision measurement of the neutron spin asymmetry A 1 n and spin-flavor decomposition in the valence quark region." Phys. Rev. Lett. **92** (2004).

[77] L.P. Kaptari, K. Kazakov, A. Umnikov, B. Kaempfer, Phys. Lett. **B321**, 271 (1994); L.P. Kaptari, A. Umnikov, C. Ciofi degli Atti, S. Scopetta, K. Kazakov, Phys. Rev.**C 51**, 52 (1995).

[78] A. Kievsky, M. Viviani and S. Rosati, “Study of bound and scattering states of three nucleon systems,” Nucl. Phys. A **577**, 511 (1994).

[79] C. Ciofi degli Atti and L. P. Kaptari, “Semi-inclusive Deep Inelastic Scattering off Few-Nucleon Systems: Tagging the EMC Effect and Hadronization Mechanisms with Detection of Slow Recoiling Nuclei,” Phys. Rev. C **83**, 044602 (2011) .

[80] V. Palli, C. Ciofi degli Atti, L. P. Kaptari, C. B. Mezzetti and M. Alvioli, “Slow Proton Production in Semi-Inclusive Deep Inelastic Scattering off Deuteron and Complex Nuclei: Hadronization and Final State Interaction Effects,” Phys. Rev. C **80**, 054610 (2009) .

[81] C. Ciofi degli Atti, L. P. Kaptari and B. Z. Kopeliovich, “Final state interaction effects in semiinclusive DIS off the deuteron,” Eur. Phys. J. A **19**, 145 (2004).

[82] S. Kuhn , C. Keppel, W. Melnitchouk (spokespersons), C. Ciofi degli Atti, L. Kaptari et al. "The structure of the free neutron via spectator tagging",

`www.jlab.org/exp_prog/proposals/03prop.html (PR03-012.pdf);`
`www.jlab.org/exp_prog/proposals/06/PR12-06-113.pdf`

[83] L. L. Frankfurt, M. M. Sargsian and M. I. Strikman, “Feynman graphs and Gribov-Glauber approach to high-energy knockout processes,” Phys. Rev. C **56**, 1124 (1997) [nucl-th/9603018].

[84] C. Ciofi degli Atti and L. P. Kaptari, “On the interpretation of the processes He-3(e,e-prime p) H-2 and He-3(e,e-prime p)(pn) at high missing momenta,” Phys. Rev. Lett. **95**, 052502 (2005) [nucl-th/0502045].

[85] C. Ciofi degli Atti and L. P. Kaptari, “A Non factorized calculation of the process He-3(e,e-prime p) H-2 at medium energies,” Phys. Rev. Lett. **100**, 122301 (2008) [arXiv:0705.3951 [nucl-th]].

[86] J. L. Friar, B. F. Gibson, G. L. Payne, A. M. Bernstein and T. E. Chupp, Phys. Rev. C **42**, 2310 (1990).

[87] A. Del Dotto, L. Kaptari, E. Pace, G. Salmè, S. Scopetta and E. Cisbani, "Flavor decomposition of transverse momentum dependent parton distributions ", EPJ Web of Conferences **73**, 02019 (2014).

[88] A. Del Dotto, E. Pace, G. Salmè, S. Scopetta, "Transversity studies with a polarized 3He target", Il Nuovo Cimento C **35**, 101 (2012).

[89] E. Pace, G. Salmè, S. Scopetta,, A. Del Dotto, M. Rinaldi, "Neutron Transverse-Momentum Distributions and Polarized 3He within Light-Front Hamiltonian Dynamics", Few-Body Syst. **54**, 1079 (2013).

[90] E. Pace, G. Salmè, S. Scopetta, A. Del Dotto, "Quark Transverse Momentum Distributions inside a nucleon : a Light-Front Hamiltonian Dynamics study ", Acta Physica Polonica, B **6**, 103 (2013).

[91] A. Del Dotto, L. Kaptari, E. Pace, G. Salmè, S. Scopetta,"Towards an improved description of SiDIS by a polarized 3He target", Few-Body Syst. **55**, 877-880 (2014).

[92] C. Fanelli,"A novel robust and efficient algorithm for charge particle tracking in high background flux.", Contribution to ACAT 2014, 1-5 September 2014, Prague. (https://indico.cern.ch/event/258092/session/8/contribution/84)
C. Fanelli, E. Cisbani and A. Del Dotto, "A novel robust and efficient algorithm for charge particle tracking in high background flux.", (submitted to IOP Conference Series).

[93] GEANT4 web site: http://www.geant4.org/geant4/

[94] A. Strandlie and R. Frühwirth, "Track and vertex reconstruction: From classical to adaptive methods", Rev.Mod.Phy. **82**, 1419, 2010.

[95] B. Denby, “Neural networks and cellular automata in experimental high energy physics", Computer Physics Communications, **49**, 429-448, 1988.

[96] C. Peterson, “Track finding with neural networks", NIM A, **279**, 537-545, 1989.

[97] Z. Chen, "Bayesian filtering: From Kalman filters to particle filters, and beyond", Statistics, **182**, 1-69, 2003.

[98] R. Van Der Merwe, "Sigma-point Kalman filters for probabilistic inference in dynamic state-space models", Diss. Oregon Health & Science University, 2004

[99] http://elec.physics.otago.ac.nz/w/images/1/19/ELEC404 Inverse Problems.pdf

[100] C. K.Chui and G. Chen. "Kalman filtering: With real time applications", Springer,1999. S.S. Haykin, "Kalman filtering and neural networks", New York: Wiley, 2001.

[101] R.E. Kalman , “A new approach to linear filtering and prediction problems", Journal of Fluids Engineering, **82**, 35-45, 1960.

[102] R. Frühwirth and M. Regler, "On the quantitative modelling of core and tails of multiple scattering by Gaussian mixtures", NIM A, **456**, 369–389, 2001.

[103] V. Bellini et al. , “GEM tracker for high luminosity experiments at the JLab Hall A", Journal of Instrumentation, **7**, C05013, 2012.

[104] Particle physics booklet. in the Americas, Australasia, or the Far East, write to: Particle Data Group, Lawrence Berkeley National Laboratory, 2010.

[105] E. J. Wolin and L. L. Ho. "Covariance matrices for track fitting with the Kalman filter." Nuclear Instruments and Methods in Physics Research Section A: Accelerators, Spectrometers, Detectors and Associated Equipment 329.3 (1993): 493-500.